Wall and bulk modes in confined turbulent rotating convection

Boot, Wouter J.M.

Award date:
2021

EINDHOVEN UNIVERSITY OF TECHNOLOGY

Fluids & Flows

Faculty of Applied Physics

Wall and bulk modes in confined turbulent rotating convection

Authors:
W. J. M. Boot (1015896)

Supervisors:
M. Madonia
A.J. Aguirre Guzmán
R.P.J. Kunnen

June 21, 2021

Abstract

Many geophysical and astrophysical flows are driven by convection and meanwhile affected by convection, which can be described by the fundamental process of Rotating Rayleigh-Bénard convection. This process is investigated by confined cylindrical experiments and direct numerical simulations. The experiments and numerical simulations show a large prominent velocity structure in the vertical and azimuthal direction in the wall region, resulting in a larger heat transport compared to periodic simulations with equal thermal forcing. This research is a continuation of the work of De Wit et al. [2020], who discovered this prominent wall structure, using direct numerical simulations on a confined cylindrical domain. The new results show that the wall mode remains present in highly turbulent flow and that its amplitude increases with increasing the thermal forcing. A maximum precessing speed of the wall mode in azimuthal direction is found for a certain degree of thermal forcing. Analysis of the flow field and the prominent wall structure show a clear relation between the coherence of the wall mode and the vertical heat transport. The flow structure in the bulk is analyzed too, showing similarities with geostrophic modes. The simulation results clearly show a critical degree of thermal forcing where the columnar flow structure changes to the regime of plumes. This transition is marked by the several changes in velocity profiles, that should be investigated further for better understanding.

Contents

1 Introduction

Convection affected by rotation takes place in many flows on the geophysical scale, for example in the atmosphere (Hartmann et al. [2001]) and in the ocean (Marshall and Schott [1999]). In the earth's outer core the same convective process takes place, resulting in the magnetic field of the earth (Roberts and King [2013]). These processes of convection affected by rotation can be simplified by the model of Rotating Rayleigh-Bénard Convection (RRBC). This model describes a system of a fluid, between two plates, which is heated from below and cooled from above within a gravitational field parallel to the temperature field. This set-up rotates around the vertical axis, resulting in a Coriolis force on the fluid.

The problem by studying these astrophysical flows, e.g. inside the core of the earth, is that they occur under extreme circumstances: very strong thermal forcing (high Rayleigh number Ra, defined later) and strong rotation (low Ekman number Ek, defined later). This problem can be approached in two ways: simulations or experiments. The disadvantage of simulations is that the dynamics are resolved down to the grid resolution, whereas in experiments the flow at all scales are "resolved". For direct numerical simulation (DNS) the computational power is the limiting factor to reach the parameter space (high Ra and low Ek) at which RRBC takes place in geophysical and astrophysical flows because the flow needs to be resolved down to the smallest active scale. The advantage of DNS is that the velocity and temperature fields can easily be analyzed, because for every grid point the velocity and temperature are calculated, while for experiments the fields need to be measured using experimental techniques, such as temperature sensors and Particle Image Velocimetry (PIV).

However, one of the largest disadvantages of experiments is that the flow is confined within a set-up (typically an upright cylinder), while for simulations a quasi-infinite domain can be achieved using periodic boundary conditions, which agrees better with large scale geophysical and astrophysical flows. The sidewall of the cylinder has a large impact on the flow field inside and causes an increase in heat transport (larger Nusselt number Nu, defined later) between

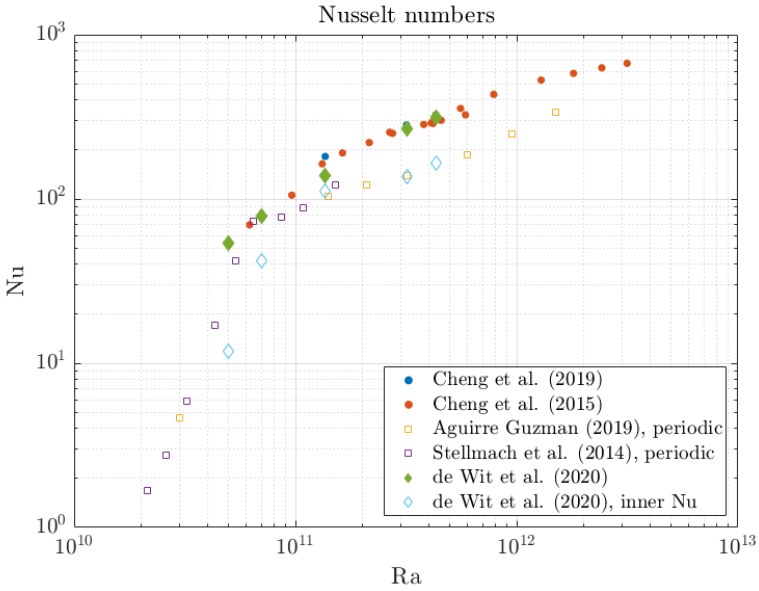

Figure 1.1: Nusselt numbers of previously performed studies: confined experiments (circles), confined simulations (diamonds) and periodic simulations (squares). A quantitative match between the Nusselt number of the bulk (open diamonds) and periodic simulations (open squares) for $Ra \geq 1.4 \times 10^{11}$ is observed. From: De Wit et al. [2020].

the top and bottom plate. This is displayed in fig. 1.1 where the Nusselt number is displayed as a function of the thermal forcing (Rayleigh number) for both confined experiments (closed circles) and quasi-infinite periodic simulations (open squares). The figure shows that for $Ra > 9.0 \times 10^{10}$ the data split into two branches: confined experimental results with a higher Nusselt number and periodic simulation results with a lower Nusselt number. To investigate the gap between the confined experiments and the periodic simulations, new simulations were done by De Wit et al. [2020] using a confined cylindrical set-up (closed diamonds). These results nicely match with the experimental results of Cheng et al. [2015] and Cheng et al. [2018] using a confined cylinder.

In the results of De Wit et al. [2020], close to the sidewall of the cylinder large vertical velocity structures are observed, divided into two halves, one with positive and one with negative vertical velocity (fig. 1.2). This ring of up- and downward velocity coincides with the hot and cold temperature field respectively, resulting in a significant contribution to the vertical heat transport. De Wit et al. [2020] separated this outer ring of heat transport from the bulk part, from which the Nusselt number of the inner flow (bulk part) was calculated (open diamonds of fig. 1.1). For $Ra \geq 9.0 \times 10^{10}$, i.e. after the split into two branches, the Nusselt number of the bulk part coincides with the Nusselt number of periodic simulations.

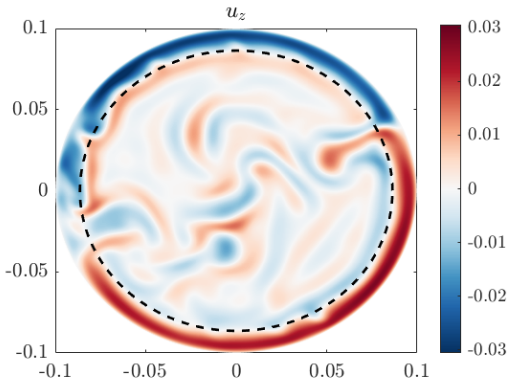

Figure 1.2: Snapshot of the vertical velocity at mid-height for $Ra = 5.0 \times 10^{10}$, showing the vertical velocity structure in the vicinity of the sidewall. The dashed circle indicates the boundary between the wall and bulk region. From: De Wit et al. [2020].

This flow structure close to the sidewall is called the wall mode. This mode is theoretically predicted as onset mode for convection by Herrmann and Busse [1993] and Zhang and Liao [2009]. Although being present near the onset of convection, this mode is very robust and still present far from the onset of convection in the turbulent regime (Zhang and Liao [2009]; Shishkina and Wagner [2006]; De Wit et al. [2020]; Favier and Knobloch [2020]). Fig. 1.1 shows that this mode heavily contributes to the overall heat transport, whereas the heat transport of the bulk part (surface enclosed by the dashed circle of fig. 1.2) quantitatively matches with the heat transport of quasi-infinite simulations. It is therefore interesting to better understand the interaction between the (velocity structures of the) wall and bulk region.

In this study the research of De Wit et al. [2020] is continued by extending the series of confined simulations with five new simulations, where the thermal forcing (Ra) is varied, while the degree of rotation (Ek), fluid properties (Pr, defined later) and cylinder dimensions (Γ, defined later) are kept constant. Two simulations are executed to focus on the parameter space close to where the confined and periodic simulations start to diverge i.e. around $Ra = 1.4 \times 10^{11}$). Three simulations are performed to investigate the flow behavior

for larger Rayleigh numbers. Another two new simulations are performed with stress-free sidewall conditions to investigate the effect of the sidewall on the flow structure.

In chapter 2 the relevant parameters and physical relations will be introduced, and an overview will be given about the research already performed in this scope. In chapter 3 the numerical approach and the used parameters will be discussed. The results will be discussed in chapter 4 and 5. Chapter 4 will focus on the flow observed close to the sidewalls and the stress-free sidewall simulations are discussed here too. Chapter 5 will mainly focus on the bulk flow. The conclusions and suggestions for further research are covered in chapter 6.

2 Theoretical background

2.1 Problem definition

In this report, the gap between the Nusselt numbers of periodic and cylindrical confined simulations, as displayed in fig. 1.1, is further investigated by performing new simulations in the cylindrical confined set-up. This set-up uses a cylindrical coordinate system (r, θ, z) and unit vectors $(\vec{e}_r, \vec{e}_\theta, \vec{e}_z)$ in radial, azimuthal and axial direction respectively as displayed in fig. 2.1. The cylindrical set-up has height H, diameter D and rotates along the central axis with angular velocity $\mathbf{\Omega} = \Omega\vec{e}_z$, parallel to gravity $\mathbf{g}$; the coordinate system is corotating. The top plate has temperature T_c and the bottom plate has temperature T_h, and $T_h > T_c$. The top and bottom boundaries have no-slip boundary conditions, whereas the sidewall has no-slip or stress-free boundary conditions.

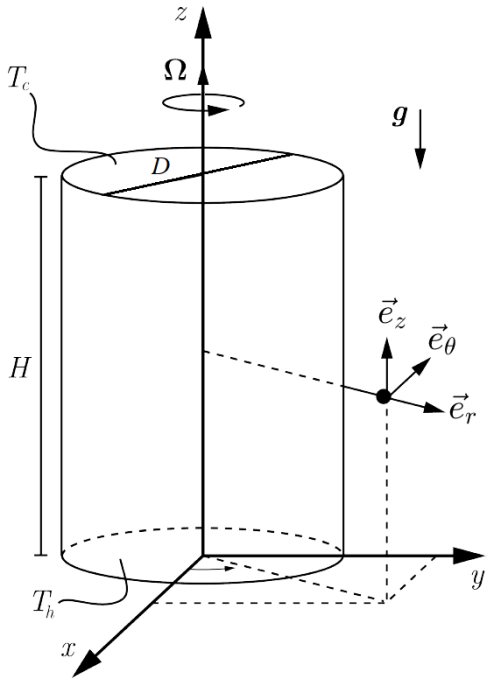

Figure 2.1: Schematic representation of the cylinder, with height H, diameter D, angular velocity $\mathbf{\Omega}$ and temperatures T_h and T_c.

2.2 Dimensionless numbers

The process of Rotating Rayleigh-Bénard Convection (RRBC) can be described with four independent dimensionless parameters, which define the geometry, flow properties, buoyancy strength, and the rotation speed of the cylinder. These are the input parameters of the simulations.

The geometry of the cylinder is described by the aspect ratio Γ, defined as

$$\Gamma \equiv \frac{D}{H}. \tag{2.1}$$

The ratio between the strengths of viscous and thermal diffusion is described by the Prandtl number Pr, defined as

$$Pr = \frac{\nu}{\kappa}, \tag{2.2}$$

with ν the kinematic viscosity and κ the thermal diffusivity.

The degree of thermal forcing is described by the Rayleigh number Ra, which is the ratio between buoyancy and diffusivity forces, defined as

$$Ra \equiv \frac{U^2 H^2}{\nu\kappa} = \frac{g\alpha H^3 \Delta T}{\nu\kappa}, \tag{2.3}$$

in which $U \equiv \sqrt{g\alpha H \Delta T}$ is the free-fall velocity (Cheng et al. [2018]) with $\Delta T \equiv T_h - T_c$, α the thermal expansion coefficient and g the gravitational acceleration.

The degree of rotation is defined by the Rossby number Ro, which is the ratio between inertial and Coriolis forces:

$$Ro \equiv \frac{U}{2\Omega H} = \frac{\sqrt{g\alpha H \Delta T}}{2\Omega H}. \tag{2.4}$$

In the simulations, the Rossby number is required as an input parameter. In the analysis of the results, the Ekman number Ek will be used instead of the Rossby number. This is a parameter that also quantifies the degree of rotation. The Ekman number is defined as

$$Ek \equiv \frac{\nu}{2\Omega H^2} = Ro\sqrt{\frac{Pr}{Ra}}. \tag{2.5}$$

2.3 Governing equations

The equations that fully describe this problem are the general Navier-Stokes equation in Boussinesq approximation, for an incompressible Newtonian fluid. The Boussinesq approximation means that any variation of fluid properties, except those that come from the coupling of density and gravity, will be ignored. This approximation is validated by Cheng et al. [2018]. The following equations will describe the conservation of momentum, energy, and mass.

The conservation of momentum is described by Chandrasekhar [1961]:

$$\underbrace{\rho\frac{D\mathbf{u}}{Dt}}_{[1]} = \underbrace{-\nabla p - \rho g\vec{e}_z}_{[2]} + \underbrace{\rho\nu\nabla^2\mathbf{u}}_{[3]} + \underbrace{g\alpha\rho\left(T - T_{ref}\right)\vec{e}_z}_{[4]} + \underbrace{\mathbf{F}}_{[5]} \tag{2.6}$$

[1] The material derivative with respect to time is defined as $\frac{D}{Dt} = \frac{\partial}{\partial t} + (\mathbf{u}\cdot\nabla)$, with $\mathbf{u}$ the velocity, ρ the density of the fluid and t the time.

[2] The gradient of pressure p contains a hydrostatic contribution, that cancels out with the gravity term $\rho g\vec{e}_z$. Defining the reduced pressure as $\hat{p} = p - \rho g(H - z)$, results in $-\nabla\hat{p} = -\nabla p - \rho g\vec{e}_z$.

[3] This term is the viscous force.

[4] This term is the buoyancy in Boussinesq approximation, with T the local temperature of the fluid and T_{ref} a reference temperature. In this study T_{ref} is the temperature of the cold top plate of the cylinder, i.e. $T_{ref} \equiv T_c$.

[5] This term represents additional forces that are working on the fluid. In this case, there are two forces, namely the centrifugal and Coriolis force. The centrifugal buoyancy due to centrifugal forces is neglected. In experiments, this is allowed to do when the Froude number $Fr \equiv \frac{\Omega^2 D}{2g}$ is smaller than 0.1 (Cheng et al. [2018]), which is the case for the

reference experiments. The Coriolis force is given by $-2\rho\boldsymbol{\Omega}\times\mathbf{u}$ (Lanczos [2020]), which results in $\mathbf{F}=-2\rho\Omega\vec{e}_z\times\mathbf{u}$.

Substituting [2] and [5] in eq. (2.6), and by multiplying both sides of the equation by $H/(\rho U^2)$ results in the dimensionless equation

$$\frac{H}{U^2}\frac{D\mathbf{u}}{Dt}=-\frac{H}{\rho U^2}\nabla\hat{p}+\frac{H\nu}{U^2}\nabla^2\mathbf{u}+\frac{T-T_c}{\Delta T}\vec{e}_z-\frac{2\Omega H}{U^2}\vec{e}_z\times\mathbf{u}. \tag{2.7}$$

Note that the fourth term is rewritten using the free-fall velocity, which is defined in section 2.2. The individual quantities of the equation are made dimensionless too, using

$$\begin{aligned}&\tilde{t}\equiv\tfrac{tU}{H}, \quad &&\tilde{\mathbf{u}}\equiv\tfrac{\mathbf{u}}{U}, \quad &&\tilde{\nabla}\equiv H\nabla,\\ &\tilde{p}\equiv\tfrac{p}{\rho U^2}, \quad &&\tilde{T}\equiv\tfrac{T-T_c}{\Delta T}.\end{aligned} \tag{2.8}$$

in which U is the free-fall velocity. Note that $\tilde{t}\equiv\frac{tU}{H}$ is made dimensionless by dividing it by the convective time unit $\tau_c=H/U$. Substituting these dimensionless quantities into eq. (2.7) results in

$$\frac{D\tilde{\mathbf{u}}}{D\tilde{t}}=-\tilde{\nabla}\tilde{p}+\frac{\nu}{HU}\tilde{\nabla}^2\tilde{\mathbf{u}}+\tilde{T}\vec{e}_z-\frac{2\Omega H}{U}\vec{e}_z\times\tilde{\mathbf{u}}. \tag{2.9}$$

The dimensionless Pr, Ra and Ro, defined in section 2.2, are substituted in this equation, resulting in

$$\frac{D\tilde{\mathbf{u}}}{D\tilde{t}}=-\tilde{\nabla}\tilde{p}+\left(\frac{Pr}{Ra}\right)^{\frac{1}{2}}\tilde{\nabla}^2\tilde{\mathbf{u}}+\tilde{T}\vec{e}_z-\frac{1}{Ro}\vec{e}_z\times\tilde{\mathbf{u}} \tag{2.10}$$

The conservation of energy in this system can be described by (Rajaei [2017])

$$\frac{DT}{Dt}=\kappa\nabla^2T, \tag{2.11}$$

in which the dimensionless quantities of eq. (2.8) can be substituted, resulting in

$$\frac{D\tilde{T}}{D\tilde{t}}=\frac{\kappa}{UH}\tilde{\nabla}^2\tilde{T}. \tag{2.12}$$

Filling in the dimensionless numbers of section 2.2 yields

$$\frac{D\tilde{T}}{D\tilde{t}}=\frac{1}{(RaPr)^{\frac{1}{2}}}\tilde{\nabla}^2\tilde{T}. \tag{2.13}$$

The equation of the conservation of mass $\nabla\cdot\mathbf{u}=0$ is made dimensionless using eq. (2.8), resulting in

$$\tilde{\nabla}\cdot\tilde{\mathbf{u}}=0. \tag{2.14}$$

Summarizing, the set of equations is given by

$$\begin{cases}\frac{D\tilde{\mathbf{u}}}{D\tilde{t}}=-\tilde{\nabla}\tilde{p}+\left(\frac{Pr}{\mathrm{Ra}}\right)^{\frac{1}{2}}\tilde{\nabla}^2\tilde{\mathbf{u}}+\tilde{T}\vec{e}_z-\frac{1}{Ro}\vec{e}_z\times\tilde{\mathbf{u}}\\ \frac{D\tilde{T}}{D\tilde{t}}=\frac{1}{(RaPr)^{\frac{1}{2}}}\tilde{\nabla}^2\tilde{T}\\ \tilde{\nabla}\cdot\tilde{\mathbf{u}}=0\end{cases} \tag{2.15}$$

In eq. (2.8) the velocity is made dimensionless by dividing it by the free-fall velocity U. The dimensionless velocity can also be rewritten as

$$\tilde{u} = \frac{u}{U} = \frac{u}{\sqrt{g\alpha H \Delta T}} = u\sqrt{\frac{1}{Ra}\frac{H^2\nu}{\nu^2\kappa}} = \frac{u}{\nu/H}\sqrt{\frac{Pr}{Ra}}, \tag{2.16}$$

in which $\frac{u}{\nu/H}$ is the dimensionless velocity in viscous units. The viscous dimensionless velocity can thus easily be calculated by $\tilde{u} \cdot \sqrt{Ra/Pr}$. Using this quantity, velocity amplitudes of simulations with different Rayleigh numbers can be compared properly. It will be explicitly mentioned when this quantity is used.

2.4 Nusselt number

One of the output parameters of the simulations is the Nusselt number, which is defined as the ratio between the total heat transfer and heat transfer by conduction:

$$Nu \equiv \frac{\langle q \rangle H}{k\Delta T}, \tag{2.17}$$

in which $\langle q \rangle$ is the average heat flux in the vertical direction and k the thermal conductivity. The average heat flux can be split into a conductive (q_{cond}) and a convective (q_{conv}) part. The conductive contribution can be written as

$$q_{cond} = -k\frac{\partial T}{\partial z} = -k\frac{\Delta T}{H}\frac{\partial \tilde{T}}{\partial \tilde{z}}, \tag{2.18}$$

and the convective part as

$$q_{conv} = \rho c_p u_z T = \frac{k}{\kappa} u_z T = \frac{k}{\kappa} U \Delta T \tilde{u}_z \tilde{T}, \tag{2.19}$$

with c_p the specific heat capacity. This can be combined together to an overall Nusselt number, defined as

$$Nu = \frac{UH}{\kappa}\left\langle \tilde{u}_z \tilde{T} \right\rangle - \left\langle \frac{\partial \tilde{T}}{\partial \tilde{z}} \right\rangle = (PrRa)^{\frac{1}{2}} \left\langle \tilde{u}_z \tilde{T} \right\rangle - \left\langle \frac{\partial \tilde{T}}{\partial \tilde{z}} \right\rangle. \tag{2.20}$$

There are different ways to calculate the Nusselt number because different averaging operations are possible. When the average is calculated over the entire volume, the second part of the definition will be -1, since the temperature $\tilde{T}$ changes from 1 to 0, when $\tilde{z}$ goes from 0 to 1. This gives the volume-averaged Nusselt number as

$$Nu_V = (PrRa)^{\frac{1}{2}} \left\langle \tilde{u}_z \tilde{T} \right\rangle_V + 1. \tag{2.21}$$

The averaging can also be performed over an arbitrary cross-sectional area within the cylinder. At $\tilde{z} = 0$ and $\tilde{z} = 1$ the vertical velocity $\tilde{u}$ is equal to zero because the boundaries are impermeable. So at these heights, the heat transport has only a conductive part and gives a wall averaged Nusselt number defined as

$$Nu_{wall} = -\left\langle \frac{\partial \tilde{T}}{\partial \tilde{z}} \right\rangle_{\tilde{z}=0,1}. \tag{2.22}$$

The Nusselt number can also be calculated using the dissipation energy rate (Shraiman and Siggia [1990]), which is (also in dimensionless units),

$$\epsilon = \nu |\nabla \mathbf{u}|^2, \quad \tilde{\epsilon} = \left(\tfrac{Pr}{Ra}\right)^{\frac{1}{2}} |\tilde{\nabla}\tilde{\mathbf{u}}|^2, \tag{2.23}$$

resulting in

$$Nu_{kin} = (PrRa)^{\frac{1}{2}} \langle \tilde{\epsilon} \rangle + 1. \tag{2.24}$$

The thermal variance $N = \kappa|\nabla T|^2$ can also be used to calculate the Nusselt number. Substituting the dimensionless quantities from eq. (2.8) results in $\tilde{N} = (PrRa)^{-\frac{1}{2}}|\tilde{\nabla}\tilde{T}|^2$, from which the Nusselt number is defined as

$$Nu_{dis} = (PrRa)^{\frac{1}{2}}\langle\tilde{N}\rangle. \tag{2.25}$$

These Nusselt number definitions will all be used later on to calculate a well-averaged Nusselt of the simulations. The right hand side of eq. (2.20) will be used to calculate the local Nusselt number of the flow.

2.5 Flow regimes

In previous work (Julien et al. [2012]; Ecke and Niemela [2014]; De Wit et al. [2020]) it is found that RRBC shows different flow characteristics depending on the interplay of the different forcings (Ra and Ek) and the fluid properties. De Wit et al. [2020] found different flow characteristics within their parameter range: Ra ($5.0 \times 10^{10} - 4.3 \times 10^{11}$), constant Γ (0.1), constant Ek (10^{-7}) and constant Pr (5.2). This parameter range covers different flow regimes, according to the classifications of Julien et al. [2012] and Cheng et al. [2018]. The boundaries of the different flow regimes are defined by the interplay between the thermal (Ra) and rotational (Ek) forces and fluid properties (Pr). When Ek is kept constant, while Ra is increased, the thermal forcing will be become more and more dominant. For small Ra, the flow is structured into convective Taylor columns (CTC), displayed in (fig. 2.2a). Increasing Ra will result in a transition from a columnar profile into plumes (fig. 2.2b)). For the current parameter settings, the transition between the regimes occurs at (Cheng et al. [2020], Kunnen [2021])

$$Ra_{CP} \approx 5.4Ek^{-1.47}. \tag{2.26}$$

The transition from plumes to geostrophic turbulence (GT) (see fig. 2.2c) is not unambiguously known for $Pr > 3$ (Cheng et al. [2018]). Further increasing Ra results in a transition from geostrophic turbulence into the regime of rotationally influence turbulence (RIT) (Cheng et al. [2020]). This transition takes place (for any Pr), according to Julien et al. [2012], at

$$Ra_{GTU,1} \approx Ek^{-8/5}Pr^{3/5}, \tag{2.27}$$

or for $Pr \approx 6$, according to Ecke and Niemela [2014], at

$$Ra_{GTU,2} \approx 1.3Ek^{-1.65}. \tag{2.28}$$

Since the highest Ra simulation of De Wit et al. [2020] is close to this transition, the geostrophic turbulent regime is also covered in that project. In this project, the Rayleigh number is further increased, while keeping the other parameters constant, whereby the RIT regime (fig. 2.2d) is covered too. The transition from the RIT regime into the non-rotating regime for large Pr occurs when the convective Rossby number is equal to 1 (Gilman [1977]), for which Ro_c is defined as (Cheng et al. [2018])

$$Ro_c \equiv \left(\frac{RaEk^2}{Pr}\right)^{1/2}. \tag{2.29}$$

So, the Rayleigh number of this transition is defined as

$$Ra_{UNR} \approx PrEk^{-2}. \tag{2.30}$$

This transition is not achieved in the new simulations either.

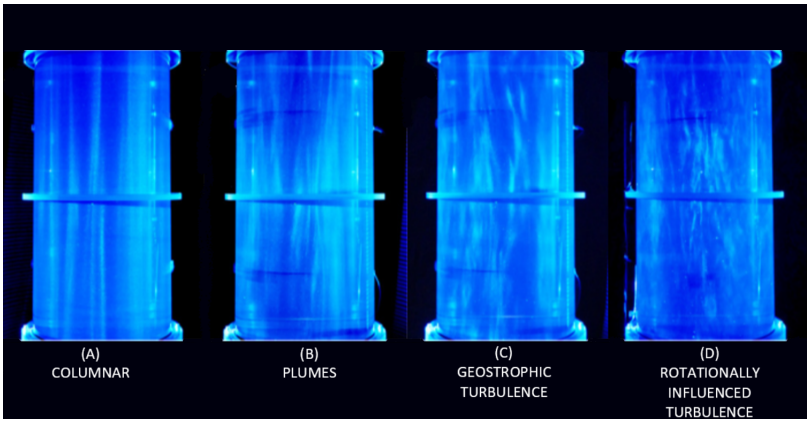

Figure 2.2: Flow regimes, that are covered in this work. Figures are obtained for $\Gamma = 0.2$, $Ek = 5 \times 10^{-8}$, $Pr \approx 5.2$ and Ra =(a) 9.6×10^{10} (columnar), (b) 8.6×10^{11} (plumes), (c) 1.2×10^{12} (geostrophic turbulence) and (d) 3.3×10^{12} (rotationally influenced turbulence). Adapted from: Cheng et al. [2020].

2.6 Boundary layers

Boundary layers are present to connect the bulk flow with the boundaries. At the top and bottom plate of the cylinder, Ekman boundary layers will form. The thickness of this boundary layer scales with (Nieuwstadt et al. [2016])

$$\tilde{\delta}_E \sim Ek^{1/2}. \tag{2.31}$$

There will be a radially in- or outward flux in this boundary layer, based on the net vorticity of the bulk flow. The negative vorticity of the bulk results in a 'pumping' of fluid from the bulk region into the Ekman boundary layer (fig. 2.3a), resulting (due to mass conservation) in a radially outward velocity field. The other way around is called Ekman suction, where fluid is sucked from the boundary layer into the bulk (fig. 2.3b), resulting in a radially inward flow in the boundary layer and a positive vorticity of the bulk.

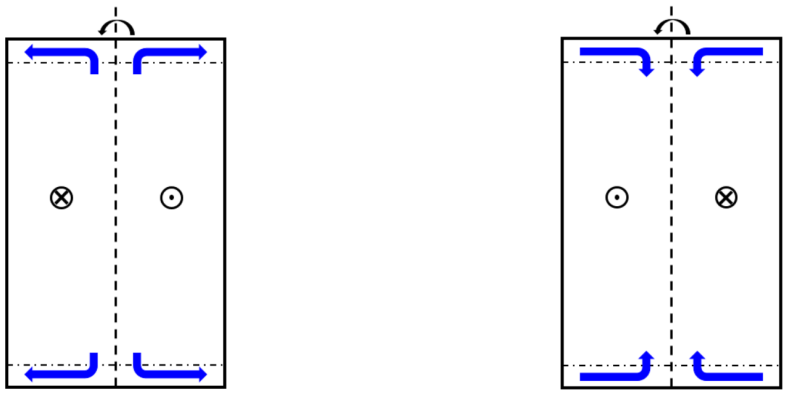

(a) Ekman pumping **(b)** Ekman suction

Figure 2.3: Schematic representation of Ekman pumping and suction, due to the sign of vorticity in the bulk.

The cylindrical set-up is a closed system, so the radially in- or outward fluxes in the top and bottom Ekman boundary layers need to be compensated near the sidewalls. Close to the sidewall, Stewartson boundary layers are present, that connect the no-slip sidewall with the bulk flow. The Stewartson layer has a theoretical thickness of (Stewartson [1957])

$$\tilde{\delta}_{S,1/4} = (2Ek)^{1/4}, \tag{2.32}$$

and connects the boundary layer flow with the bulk flow. Within this layer, there is an even smaller layer (Stewartson [1957])

$$\tilde{\delta}_{S,1/3} = (2Ek)^{1/3}, \tag{2.33}$$

that connects the sidewall flow with the no-slip sidewall boundaries.

Another definition to connect the bulk flow with the walls is used by Julien et al. [2012], who defined the location of the maximum viscous dissipation rate as the thickness of the kinetic boundary layer. Stevens et al. [2010] used the location of the maximum root mean square of the temperature (T_{RMS}) and velocity ($u_{r,\theta,z}RMS$) as the thickness of the thermal and kinetic boundary layer respectively. Note that the RMS is not the real RMS, but defined (in this case for the temperature) as

$$T_{rms} = \sqrt{\langle T^2 \rangle - \langle T \rangle^2}. \tag{2.34}$$

This definition is used throughout this study and is referred to as the RMS.

There exists a region close to the sidewall with sections with large vertical (and azimuthal) velocity values, both positive and negative (fig. 1.2). The thickness of this layer can be determined in several ways. De Wit et al. [2020] defined the thickness of this layer as the location where the root mean square of the vertical velocity field has its local minimum, which means that at that radial distance the vertical velocities are minimal. Zhang et al. [2020] defined the thickness of this layer as the location where the azimuthally averaged azimuthal velocity is equal to zero. These two definitions will be used in this study to decouple the wall region from the bulk region.

The structure of positive and negative velocities near the sidewall drifts in the azimuthal direction, with a velocity which is more than two orders of magnitudes slower than the rotation rate of the cylinder (De Wit et al. [2020]). Favier and Knobloch [2020] argued that these observed structures are wall modes, albeit far from their linear onset, i.e. the region where they are supposed to exist. Wall modes were first computed, within linear theory, by Goldstein et al. [1993]. The modes are very stable and persist in turbulent bulk flows and even changes in the shape of the cylinder do not destroy the wall mode (Favier and Knobloch [2020]). The precession rate depends on the Rayleigh number, Ekman number and dimensions of the cylinder (Ecke et al. [1992]; De Wit et al. [2020]; Zhang et al. [2021]). The wall mode can precess in both prograde and retrograde direction (Horn and Schmid [2017]).

The onset of wall modes depends on the Rayleigh and Ekman number. By increasing the thermal forcing (increasing Ra), while keeping the rotation (Ek) constant, a parameter space is reached where a bulk mode arises. These bulk modes are convective structures that dominate the core of the cylinder and its velocity components have periodic behavior in the radial and azimuthal direction. In general, the wall modes precess with a higher precession rate than the bulk modes (c.f. Favier and Knobloch [2020]).

2.7 Kolmogorov and Batchelor scales

A suitable grid resolution is required to resolve the above-described equations (eq. (2.15)). A suitable resolution has not too many length scales of the smallest flow features in one grid cell. For velocity features the smallest length scale is the Kolmogorov length scale η, for thermal features the Batchelor length scale η_T. Both length scales are based on the dissipation rate of kinetic energy ϵ (eq. (2.23)), which results for the Kolmogorov and Batchelor length scales

into (Monin et al. [1975])

$$\eta = \left(\frac{\nu^3}{\epsilon}\right)^{\frac{1}{4}}, \quad \tilde{\eta} = \left(\frac{Pr}{Ra}\right)^{\frac{3}{8}} \tilde{\epsilon}^{-\frac{1}{4}}, \tag{2.35}$$

$$\eta_T = \eta \left(\frac{\kappa}{\nu}\right)^{\frac{1}{2}}, \quad \tilde{\eta}_T = \tilde{\eta} Pr^{-\frac{1}{2}}. \tag{2.36}$$

In this report, the dimensionless units, as displayed in eq. (2.8), will be used by default. It will explicitly be mentioned when other units are used. So time is convective time and velocity is velocity divided by the free-fall velocity etc. For simplicity, and ease of reading, tildes will be omitted.

3 Methods

3.1 Code description

To simulate RRBC in a cylinder the numerical method that is described by Verzicco and Orlandi [1996] is used to solve eq. (2.15) using a finite-difference method that is second-order accurate in space and time. A cylindrical coordinate system is used to solve the equations, which causes problems in the numerical scheme at $r = 0$ due to the singularities of the Navier-Stokes equations. This is solved by not solving the equations for the velocities fields, but by solving the flow for q_θ, q_r and q_z which are defined as

$$\begin{cases} q_\theta \equiv u_\theta = \mathbf{u} \cdot \vec{e}_\theta, \\ q_r \equiv r u_r = r\mathbf{u} \cdot \vec{e}_r, \\ q_z \equiv u_z = \mathbf{u}\vec{e}_z. \end{cases} \tag{3.1}$$

This solves the singularity struggle in the origin with $q_r = 0$ at $r = 0$.

As schematically displayed in fig. 3.1, the pressure p and temperature Φ are calculated in the center of the grid cells, whereas the azimuthal, radial and vertical velocities are calculated at the center of the faces of the cells, perpendicular to the velocity directions.

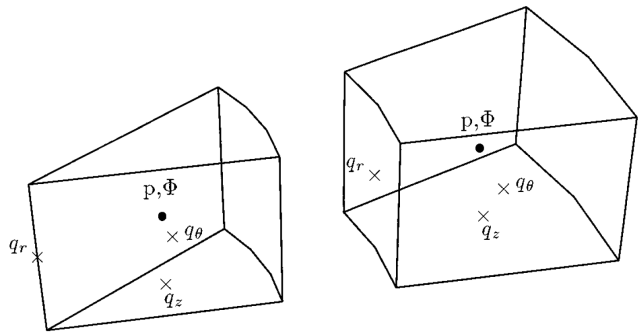

Figure 3.1: Schematic representation of the grid cells, showing the locations where the velocities, pressure and temperature are calculated.

Simulations with both stress-free and no-slip sidewall boundaries are performed, whereas the top and bottom boundaries have no-slip conditions in all the cases. The non-permeability condition holds for all the boundaries. The sidewall of the cylinder is isolated and the top and bottom plates are set to a constant temperature. So for the no-slip simulations:

$$\begin{cases} \mathbf{u} = \mathbf{0}, & T = 1, & \text{at } z = 0, \\ \mathbf{u} = \mathbf{0}, & T = 0, & \text{at } z = 1, \\ \mathbf{u} = \mathbf{0}, & \frac{\partial T}{\partial r} = 0, & \text{at } r = \Gamma/2. \end{cases} \tag{3.2}$$

And for stress-free sidewall simulations:

$$\begin{cases} \mathbf{u} = \mathbf{0}, & T = 1, & \text{at } z = 0, \\ \mathbf{u} = \mathbf{0}, & T = 0, & \text{at } z = 1, \\ u_r = \frac{\partial u_\theta}{\partial r} = \frac{\partial u_z}{\partial r} = 0, & \frac{\partial T}{\partial r} = 0, & \text{at } r = \Gamma/2. \end{cases} \tag{3.3}$$

3.2 Input parameters

Five new simulations with no-slip sidewall boundary conditions and two new simulations with stress-free sidewall boundaries are performed in this study. To compare the new results with previous simulations obtained by De Wit et al. [2020], the same Prandtl number ($Pr = 5.2$), Ekman number ($Ek = 10^{-7}$) and aspect ratio ($\Gamma = 0.2$) are used. The input parameters are

tabulated in section 3.2. De Wit et al. [2020] found different results for Ra being smaller or larger than 1.4×10^{11}. To investigate this change of behavior, two simulations are performed, from which the Rayleigh numbers are logarithmically in the middle of the gap between the data points around $Ra = 1.4 \times 10^{11}$, namely at $Ra = 9.9 \times 10^{11}$ and $Ra = 2.1 \times 10^{11}$. The other three no-slip simulations, with larger Ra, are chosen to further investigate the gap between the Nusselt numbers in periodic simulations and simulations in a cylindrical domain. The Ra of these simulations coincide with the Rayleigh numbers used by Aguirre Guzmán [2021] in periodic simulations for a good comparison.

One Rayleigh number of the stress-free sidewall simulations is below $Ra = 1.4 \times 10^{11}$, the other above $Ra = 1.4 \times 10^{11}$ to investigate the sidewall influence on both observed flow behaviors. The chosen Rayleigh numbers coincide with the Rayleigh numbers of no-slip sidewall simulations performed by De Wit et al. [2020].

Ra	Pr	Ek	Ro	Sidewall
9.9×10^{10}	5.2	10^{-7}	1.4×10^{-2}	no-slip
2.1×10^{11}	5.2	10^{-7}	2.0×10^{-2}	no-slip
6.0×10^{11}	5.2	10^{-7}	3.4×10^{-2}	no-slip
9.5×10^{11}	5.2	10^{-7}	4.3×10^{-2}	no-slip
1.5×10^{12}	5.2	10^{-7}	5.4×10^{-2}	no-slip
5.0×10^{10}	5.2	10^{-7}	9.8×10^{-3}	stress-free
3.2×10^{10}	5.2	10^{-7}	2.5×10^{-2}	stress-free

Table 3.1: Input parameters of the simulations.

For a general analysis of the flow structures and the Ra dependence, the simulation data obtained by De Wit et al. [2020] is used too. The simulations of De Wit et al. [2020] are performed at $Ra = 5.0 \times 10^{10}, 7.0 \times 10^{10}, 1.4 \times 10^{11}, 3.2 \times 10^{11}$ and 4.3×10^{11}.

3.3 Grid resolution

For the simulations with $Ra = 9.9 \times 10^{10}$ and 2.1×10^{11} and both stress-free simulations a grid with $769 \times 351 \times 1025$ grid points in the azimuthal, radial, and axial direction is used. This grid is uniform in the azimuthal direction and non-uniform in the radial and axial direction. A higher grid resolution close to the sidewall and close to the top and bottom is applied, to properly simulate the Ekman layers and the sidewall boundary layer.

The grid resolution of the bulk is verified by calculating the Batchelor length η_T because this is the smallest length scale in the bulk for $Pr > 1$ (eqs. (2.35) to (2.36)). The maximum number of Batchelor lengths within one grid cell is calculated by dividing the Batchelor length scale by the maximum distance between grid points in one of the directions, i.e. $\eta_T / \max(\Delta\theta, \Delta r, \Delta z)$. This gives the largest number of Batchelor lengths per grid cell in the azimuthal, radial, or axial direction. According to Verzicco and Camussi [2003], the maximum number of length scales should remain below 4. The size of the length scales decreases with increasing Ra, while keeping the other parameters constant. So the simulations with the largest Ra are discussed, because when the grid is sufficient with the largest Ra, it will also be sufficient for lower Ra. The number of Batchelor lengths of the stress-free simulation with $Ra = 3.2 \times 10^{11}$ is displayed in fig. 3.2a. The figure shows that for these simulations the number of Batchelor lengths is below 4 in the bulk, which means that the bulk resolution is sufficient.

The simulation with the largest Rayleigh number ($Ra = 4.3 \times 10^{11}$) of De Wit et al. [2020] showed a too coarse grid in the bulk region. The amount of Batchelor lengths within a grid cell was above 4 (but still below 5). So, for the three simulations with $Ra = 6.0 \times 10^{11}$-

1.5×10^{12} a higher grid density is used: $1025 \times 469 \times 1365$ grid points in the azimuthal, radial, and axial direction. The simulations with $Ra = 6.0 \times 10^{11}$ and 9.5×10^{11} show a high enough grid density, i.e. less than 4 Batchelor lengths per cell in all directions. The simulation with $Ra = 1.5 \times 10^{12}$ showed numbers of length scales above 4, but below 5.5, as displayed in fig. 3.2b. Whereas De Wit et al. [2020] found proper results while exceeding the number of 4 Batchelor length scales in the bulk, we expect proper results for simulations with $Ra = 1.5 \times 10^{12}$ too. It is known that a too coarse grid resolution results in a too high Nusselt number (Verzicco and Camussi [2003]). The Nusselt number of $Ra = 1.5 \times 10^{12}$ is compared with experimental results (will be displayed in chapter 4), showing no overestimation of the Nusselt number, from which is concluded that the grid resolution is sufficient.

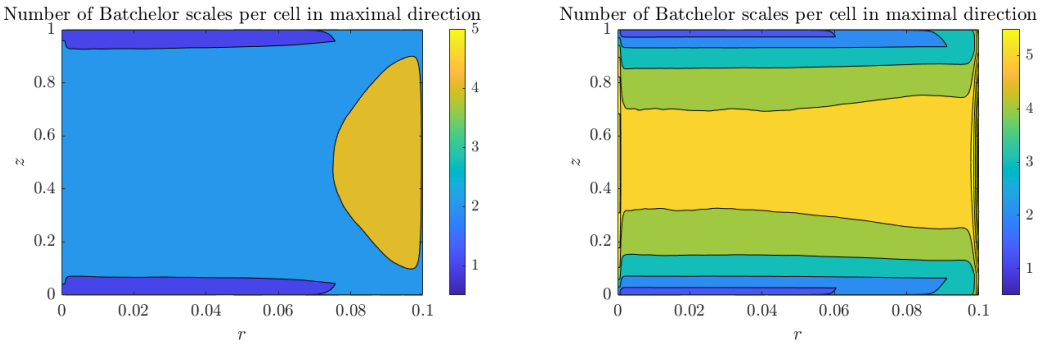

(a) $Ra = 3.2 \times 10^{11}$, stress-free

(b) $Ra = 1.5 \times 10^{12}$, no-slip

Figure 3.2: Maximum number of Batchelor length scales in one of the directions (r,θ,z)per grid cell for stress-free (a) and no-slip (b) sidewall conditions.

According to Verzicco and Camussi [2003], there should be at least six cells in the boundary layers (Ekman and sidewall) to simulate them properly. The simulations are all performed at the same Ekman number, so the Ekman boundary layer thickness is expected to be the same in all simulations. The Ekman boundary layer thickness is determined by the peak of the root mean square of the velocity parallel to the boundaries. The simulations with the lowest grid resolution ($769 \times 351 \times 1025$) all showed a boundary layer that was covered by 16 cells. The finer grid ($1025 \times 469 \times 1365$) showed the boundary layer covered by 23 cells. This number of grid cells in the Ekman boundary layers is more than sufficient.
At the sidewall of the simulations with the lowest resolution, 27 grid cells were found in the sidewall boundary layer based on the Stewartson boundary layer thickness for no-slip simulations (eq. (2.32)). For the higher resolution, 41 grid cells were found in the sidewall boundary layer, which is also more than sufficient.

4 Results and Discussion: Wall mode

The results of this study are split into two chapters: part concerning the wall region (approx. $0.08 < r < 0.1$) and a part concerning the bulk region (approx. $0 < r < 0.08$). Flow phenomena concerning the wall region are discussed in this chapter. Flow phenomena that dominate in the bulk will be discussed in chapter 5. This chapter is split into two main sections. In section 4.1 the results of the simulations with no-slip sidewall conditions are discussed, in section 4.2 the results with stress-free sidewalls are discussed.

The structure of section 4.1 is as follows: first, the presence of the wall mode will be proved and the precession rate will be determined, from which rotation averaged flow structures are generated. The strength, coherence, and thickness of the wall mode are calculated and the Ra dependence is investigated. Next, the thickness of the wall region is used to decouple the wall region from the bulk region, after which the heat transport (Nusselt number) of both regions (bulk and wall) is calculated. The degree of coherence of the wall mode and the transport in the top and bottom Ekman boundary layers are used to explain the Ra dependence of the heat transport. Finally, rotation averaged flow structures are used to mathematically approach the problem using a 3D fitting method, to investigate the Ra dependence of the different parameters.

This same structure is used in section 4.2.

4.1 No-slip sidewall

Close to the sidewall of a cylindrical set-up in RRBC conditions a large stable velocity field arises with well-pronounced positive and negative vertical velocity regions. This is exemplarily displayed in figs. 4.1a to 4.1c where snapshots of the vertical velocity at mid-height ($z = 0.50$) for three different Ra cases are shown. In figs. 4.1d to 4.1f the vertical velocity profiles along the dashed lines of figs. 4.1a to 4.1c are shown. For low Ra, e.g. $Ra = 5.0 \times 10^{10}$, a step-like flow structure of vertical velocity is observed, whereas a well-pronounced sinusoidal profile with deviations is observed for large Ra, e.g. $Ra = 1.5 \times 10^{12}$. In between these numbers ($Ra = 1.4 \times 10^{11}$) the vertical flow structure has a weak sinusoidal shape, with strong irregularities. Note that these graphs are unaveraged snapshots, although being exemplarily for the vertical flow observed around these Ra values.

4.1.1 Precessing wall mode

The observed structure in the vicinity of the sidewall precesses in the azimuthal direction as a function of time. Following De Wit et al. [2020] the vertical flow structure is fitted in time using the sinusoidal fit

$$u_z(\theta) = A_{amp} \cdot \cos(\theta - \phi_0) + B_{os}, \tag{4.1}$$

where A_{amp} is the amplitude, ϕ_0 the azimuthal orientation (from which the precession velocity can be calculated) and B_{os} the offset (almost zero). The sinusoidal fitting is performed at the radial distance where the azimuthally and temporally averaged root mean square of the vertical velocity (u_zRMS) is maximal. This maximum in RMS means that at this radial distance the data points are most widely spread, which means that at this radial distance the difference in up- and downward velocity is maximal. This is different from De Wit et al. [2020], who used a radial distance halfway the boundary layer to fit the vertical velocity profile. Using the method of De Wit et al. [2020] is correct when only the precession (velocity) is evaluated. The flow profile could have a different shape in the radial direction for different Ra, resulting in maximum velocities at different radial distances. Using the radial distance where u_zRMS is maximal to fit the sinusoidal profile, makes it also possible to compare the

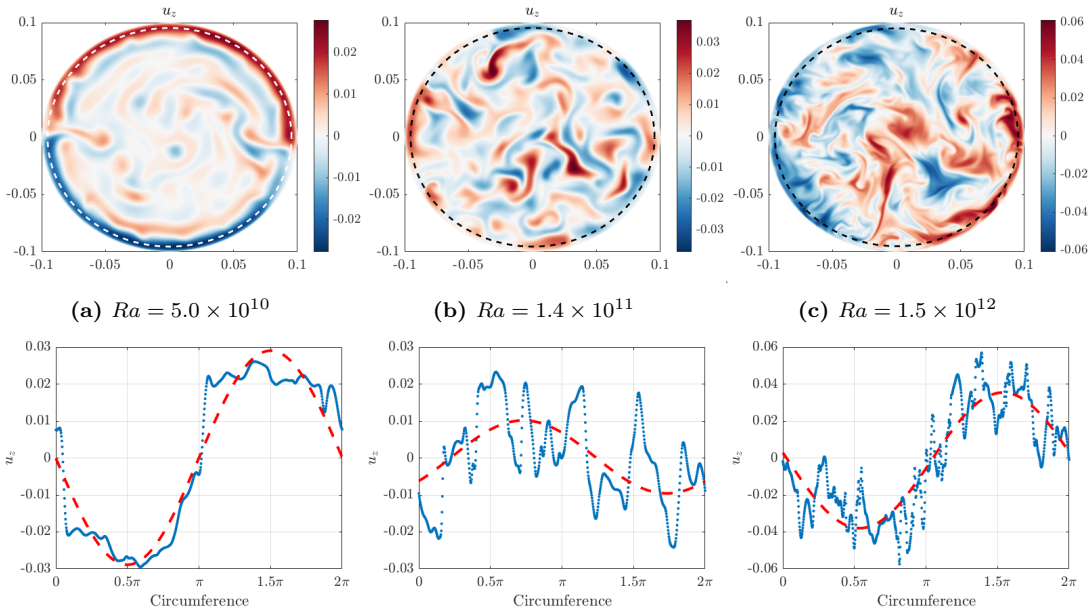

(a) $Ra = 5.0 \times 10^{10}$ **(b)** $Ra = 1.4 \times 10^{11}$ **(c)** $Ra = 1.5 \times 10^{12}$

(d) u_z in azimuthal direction for $Ra = 5.0 \times 10^{10}$. **(e)** u_z in azimuthal direction for $Ra = 1.4 \times 10^{11}$. **(f)** u_z in azimuthal direction for $Ra = 1.5 \times 10^{12}$.

Figure 4.1: Fig. (a)-(c): Vertical velocity profiles at mid-height ($z = 0.50$) for different Ra. Fig. (d)-(f): vertical velocity profile along dashed circles of fig. (a)-(c), showing a $n = 1$ mode in azimuthal direction. The data is fitted (red dashed line) using a sinusoidal equation (eq. (4.1)).

amplitudes of the vertical velocity profile of the different Ra cases in the wall region.

The angular position ϕ_0 of the flow profile as a function of time for all Ra is displayed in fig. 4.2a and shows that in all cases the wall structure rotates in the negative azimuthal direction. The figure shows that in the range of $Ra = 5.0 \times 10^{10} - 6.0 \times 10^{11}$ the phase shift of the vertical flow profile in time (i.e. precession frequency) increases with increasing Ra. A close-up of the precession frequency of the three highest Ra ($Ra = 6.0 \times 10^{11} - 1.5 \times 10^{12}$) is displayed in fig. 4.2b. The figure shows that these three cases have flow structures that rotate with almost the same velocity in the azimuthal direction.

The averaged precession speed of the profile in the azimuthal direction is calculated by fitting the phase shifts of fig. 4.2a and is displayed in fig. 4.3 as a function of the Rayleigh number. The figure shows a Ra dependence of the precession speed until a maximum speed is reached at $Ra = 6.0 \times 10^{11}$. For the range $Ra = 5.0 \times 10^{10} - 6.0 \times 10^{11}$ a Ra dependence is found as $|\omega_{sc}| = (2.4 \times 10^{-9}) \cdot Ra^{0.64 \pm 0.12}$. A constant precession speed of $|\omega_{sc}| = 0.079$ is found for the largest three Ra cases. This maximum precession speed is expected, because at a certain speed the force to precess and the sidewall friction are in equilibrium, resulting in a maximum speed. The size of sidewall friction is based on the aspect ratio Γ, which is thus the parameter that determines the maximum precession speed. Varying this parameter should result in different maximum precession speeds.

When the snapshots of fig. 4.1 are averaged in time, the positive and negative velocity sections close to the sidewall boundary will average out, because the structure precesses in the azimuthal direction in time. Using the phase shifts (fig. 4.2a), the snapshots can be rotated back to a fixed orientation, after which a rotation averaged flow profile can be made. This is done as a representative example for $Ra = 4.3 \times 10^{11}$ at mid-height in fig. 4.4 for the vertical, radial and azimuthal velocity field. Here, the in-plane $r - \theta$ velocity field is displayed with

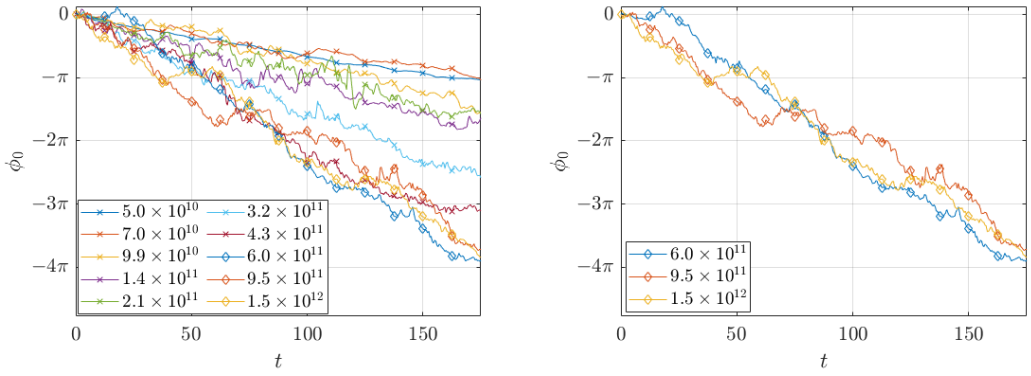

(a) Azimuthal orientation of the wall mode as a function of time.

(b) Close-up of the 3 highest Ra cases, showing a phase shift of the wall structure that is independent of the Rayleigh number.

Figure 4.2: Angular position of the vertical wall structure in time for varying Rayleigh numbers, showing a Ra dependent precession velocity for $Ra \leq 6.0 \times 10^{11}$ and independent for $Ra \geq 6.0 \times 10^{11}$.

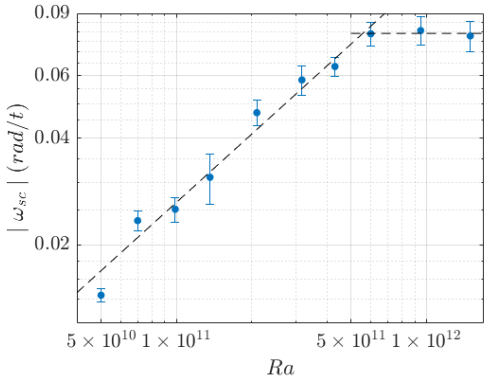

Figure 4.3: The absolute angular velocity $\mid \omega_{wc} \mid$ for different Rayleigh numbers. The uncertainties are calculated by fitting the data of fig. 4.2a. A power-law is fitted, resulting in $\mid \omega_{wc} \mid = (2.4 \times 10^{-9}) \cdot Ra^{0.64 \pm 0.12}$ for $Ra \leq 6.0 \times 10^{11}$.

the vector field. The figures show an $n = 1$ mode in azimuthal direction for the vertical velocity profile in the wall region, whereas an $n = 2$ mode is observed in the bulk region for u_r and u_θ. Rotation averaged profiles of u_z, u_r and u_θ for all Ra at $z = 0.25, 0.50$ and 0.75 are displayed in appendix D.1.

The overall vertical velocity scale increases with increasing Ra. This is displayed in fig. 4.5a, where the root mean square of the vertical velocity ($u_z RMS$) averaged in the azimuthal direction and in time at mid-height is displayed as a function of the radius r. The figure shows an increase of $u_z RMS$ in the bulk region (approx. $0 < r < 0.08$) with increasing Rayleigh number. This is caused by stronger thermal forcing, which causes larger velocity scales and so larger RMS values, because of the wider spread of the data. For each Ra, the $u_z RMS$ graph clearly shows a peak in RMS-value in the wall region. This peak is caused by the well-pronounced up- and downward going velocity sections, i.e. the wall mode. The peaks of the $u_z RMS$ of the $Ra = 7.0 \times 10^{10} - 1.4 \times 10^{11}$ simulations are lower than the peak of the $Ra = 5.0 \times 10^{10}$ case. This lower $u_z RMS$ is probably the result of a less-pronounced wall mode, resulting in a smaller spread of data points and so a lower RMS value.

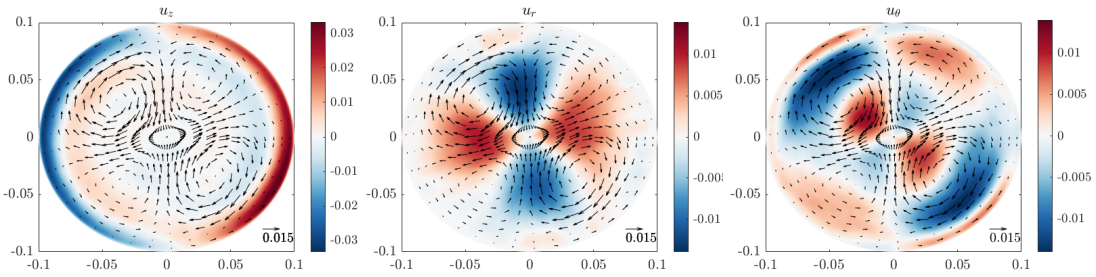

(a) Vertical velocity field. **(b)** Radial velocity field. **(c)** Azimuthal velocity field.

Figure 4.4: Precession averaged velocity fields at mid-height with $Ra = 4.3 \times 10^{11}$. The in-plane $r - \theta$ velocity field in indicated with the vector field. The $n = 1$ (vertical) and $n = 2$ (radial and azimuthal) structures are clearly visible.

The velocity scales increase with increasing Ra, see bulk part (approx. $0 < r < 0.08$) of fig. 4.5a, so a quantitative comparison between strengths of wall modes with different Ra can only be made when the relative strength of the wall modes are compared. This relative strength is calculated by dividing the time-averaged amplitude of the cosine fit (eq. (4.1)) by the averaged u_zRMS value of a part of the bulk ($0 < r < 0.05$). This fixed radius is used, instead of the boundary between bulk and wall, to cancel out influences from the wall into the bulk, e.g. the second peak in u_zRMS, which is present for $Ra = 5.0 \times 10^{10}$. The relative strength of the wall mode is displayed in fig. 4.5b, where a dip in the strength is observed around $Ra = 1.4 \times 10^{11}$, which is in accordance with fig. 4.5a where a lower u_zRMS-*peak* value is observed for this Ra. For cases with $Ra < 1.4 \times 10^{11}$, a strong decrease of wall mode strength is observed, whereas for $Ra > 1.4 \times 10^{11}$ the wall mode has a constant strength, relative to the velocity scales.

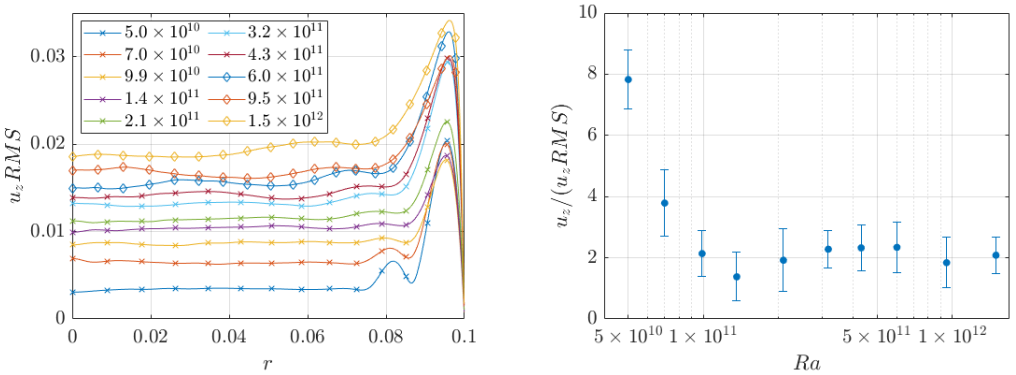

(a) u_zRMS as a function of the radius r at mid-height, showing an increase in RMS for increasing Ra, and a strong increase in RMS close to the sidewall boundary.

(b) Strength of the wall structure, relative to the overall vertical velocity scales as a function of Rayleigh. Error bars indicating one standard deviation.

Figure 4.5

The degree of correlation of the cosine fit and the vertical flow structure in the sidewall boundary region is reviewed by calculating the coefficient of determination R^2 for the fits of these velocity profiles (figs. 4.1d to 4.1f). R^2 is the normalized sum of squares between the fit and the data and takes values between 0 (no correlation) and 1 (full correlation). So, a well-pronounced sinusoidal flow profile with small deviations will result in a relatively high R^2 (fig. 4.1d and 4.1f), while a flow profile with large deviations will have a low R^2 (fig. 4.1e).

This calculation is done for all time instances at the radial distance where u_zRMS is maximal. The time-averaged R^2 values are displayed in fig. 4.6 and show a strong decrease in R^2 with increasing Rayleigh number for $Ra \leq 1.4 \times 10^{11}$. For larger Ra, an approximated constant value of $R^2 = 0.63 \pm 0.04$ is found. The largest uncertainties are logically found for the lowest R^2 values $Ra = 1.4 \times 10^{11} - 2.1 \times 10^{11}$ because when the wall mode is the least stable, the largest fluctuations will occur.

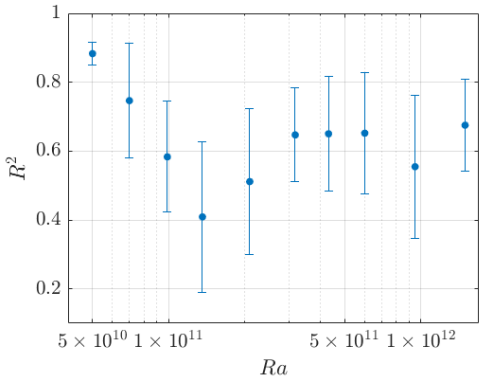

Figure 4.6: R^2 as a function of the Rayleigh number, clearly indicating the less-pronounced wall mode around $Ra = 1.4 \times 10^{11}$, with one time the standard deviation as error bars.

Note that for high Ra ($Ra \geq 3.2 \times 10^{11}$) a cosine is a more convenient function to fit the wall structure because the vertical profile has a sinusoidal shape with irregularities (see fig. 4.1f). For the low Ra cases ($Ra \leq 9.9 \times 10^{10}$), the vertical flow profile has a more square-wave-like function (fig. 4.1d), which underestimates the coherence of the wall mode, because the wall mode is very coherent, but has not its sinusoidal shape. This is not a problem, since the largest R^2 values are still found for the lowest Rayleigh numbers.
Summarizing, the relative strength of the wall mode and the coherence decrease for $Ra \leq 1.4 \times 10^{11}$ for increasing Ra, resulting in the relative low u_zRMS values for these Ra in fig. 4.5a. For larger Ra, the u_zRMS increases with increasing Ra.

4.1.2 Sidewall Boundary Layer Thickness

A clear definition of the sidewall boundary layer width is important because with a coherent, meaningful definition the wall and bulk parts could probably be decoupled, and both can be analyzed separately. The thickness of the sidewall boundary layer can be described by several definitions, as described in section 2.6. In fig. 4.7a the thickness of the boundary layers is displayed as a function of Ra for different definitions. The kinetic boundary layer definitions based on the RMS in vertical (u_zRMS) and azimuthal ($u_\theta RMS$) velocity (used by Stevens et al. [2010]) show an (almost) constant boundary layer thickness that coincides with each other. Moving radially further outward, the RMS decreases (i.e. the velocities decrease) due to the no-slip sidewall. This means that these definitions indicate the thickness of the kinetic boundary layer that connects the boundary flow with the no-slip sidewalls, with almost the same thickness as the theoretical $Ek^{1/3}$-layer (Stewartson [1957]).

Further, the figure shows the ever-increasing boundary layer width using the u_zRMS-*dip* definition (De Wit et al. [2020]) with a fit: $\delta = ((7 \pm 2) \times 10^{-5}) \cdot Ra^{0.21 \pm 0.02}$. This is also visible in fig. 4.5a where the distance between the wall and the dip in RMS value increases with increasing Ra. This fit is based on the Rayleigh number only, whereas this is the only parameter that is varied in this study, so dependences on the Ekman number, Prandtl number, and aspect ratio can not be excluded. Note that for some cases at mid-height the dip in

u_zRMS is hardly visible, e.g. $Ra = 2.1 \times 10^{11}$ and $Ra = 4.3 \times 10^{11}$ in fig. 4.5a.

Analysis of the overall vertical structure of the simulations show that there are some heights where no u_zRMS-*dip* is observed, e.g. $Ra = 1.5 \times 10^{12}$ at heights $z = 0.25$ and $z = 0.75$ and for the stress-free sidewall boundary simulation with $Ra = 3.2 \times 10^{11}$ no u_zRMS-*dip* is observed at any height. In these cases, there is just a decrease in slope. A more general definition that can also be applied for these cases is:

$$\min\left(\left|\frac{\partial u_zRMS}{\partial r}\right|\right), \tag{4.2}$$

which will locate both u_zRMS-*dip* and the decrease in slope, and so define the thickness of the boundary layer, correctly.

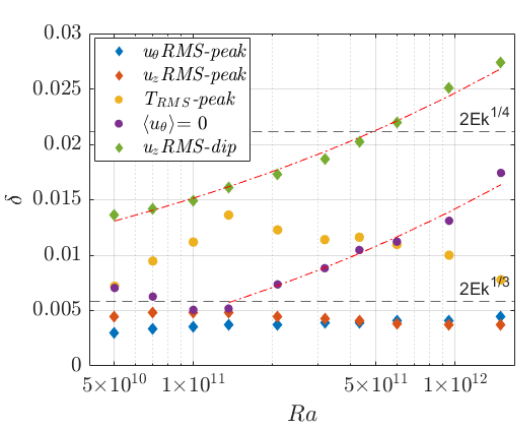

(a) Boundary layer thickness for several definitions as functions of Ra.

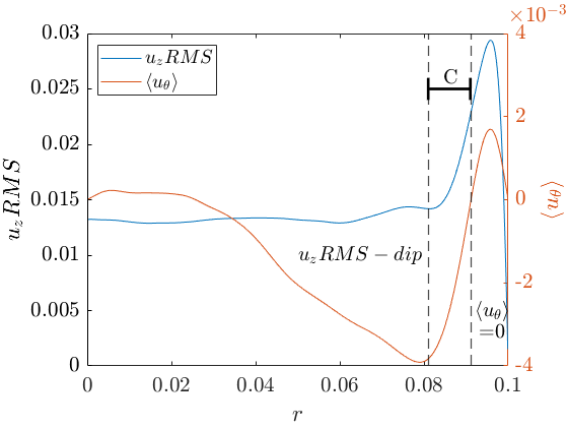

(b) u_zRMS and $\langle u_\theta \rangle$. Vertical dashed lines indicate the boundary layer thickness based on u_zRMS-*dip* and $\langle u_\theta \rangle = 0$ and show the constant distance C that is observed for $Ra \geq 1.4 \times 10^{11}$.

Figure 4.7

Fig. 4.7a shows that the boundary layer thicknesses that rely on the definitions based on T_{RMS}-*peak* (Stevens et al. [2010]) and $\langle u_\theta \rangle = 0$ (Zhang et al. [2020]) both show a certain kink around $Ra = 1.4 \times 10^{11}$. This obvious change of behavior could be the transition between two different regimes of wall modes. Fitting the boundary layer widths for $Ra \geq 1.4 \times 10^{11}$ using the $\langle u_\theta \rangle = 0$ definition, show a fit which is (almost) parallel to the fit based on the u_zRMS-*dip* definition, with equation $\delta = ((5 \pm 1) \times 10^{-5}) Ra^{0.22 \pm 0.02} - C$, where C is the averaged difference between u_zRMS-*dip* and $\langle u_\theta \rangle = 0$. This means that there is a constant ($C \approx 0.01$) distance between the zero-crossing of the azimuthal flow profile and the zero-crossing of the vertical flow profile which is independent of the Rayleigh number for $Ra \geq 1.4 \times 10^{11}$. This is, as an example, visualized at mid-height for $Ra = 3.2 \times 10^{11}$ in fig. 4.7b, where the constant distance C is the distance between the two vertical dashed lines which indicate the location of the boundaries based on the u_zRMS-*dip* and $\langle u_\theta \rangle = 0$ definition. That this distance between both definitions (i.e. C) is Ra independent, whereas the total thickness of the boundary layer increases with increasing Ra, means that this section (between the two dashed lines) moves radially inward with increasing Ra and that the growth of thickness of the boundary layer takes place in the region between $\langle u_\theta \rangle = 0$ and the sidewall.

4.1.3 Ekman boundary layers at top and bottom plates

Whereas the sidewall boundary layer thickness changes as a function of the Rayleigh number, the top and bottom boundary layer thicknesses are conserved because the Ekman number is

not changed ($Ek = 10^{-7}$). This shows that the boundary layers at the top and bottom plates remain laminar Ekman-type boundary layers. In fig. 4.8a the azimuthally and temporally averaged vector field of the radial and vertical velocity for $Ra = 4.3 \times 10^{11}$ is displayed for the region close to the bottom of the cylinder. The figure shows a strong radially outward velocity field close to the bottom plate (Ekman boundary layer) and a dominant vertical velocity field in the sidewall region. In fig. 4.8b the radial velocity, averaged in the azimuthal direction, in time and over the radial distance of the bulk, so in this case over $0 < r < 0.08$, is displayed as a function of the height z. In other words, the figure shows the average radial velocity as a function of the height z and indicates the Ekman boundary layers at the top and bottom of the cylinder. The zero crossings of the velocity profile are used as thicknesses of the Ekman boundary layer in fig. 4.8a.

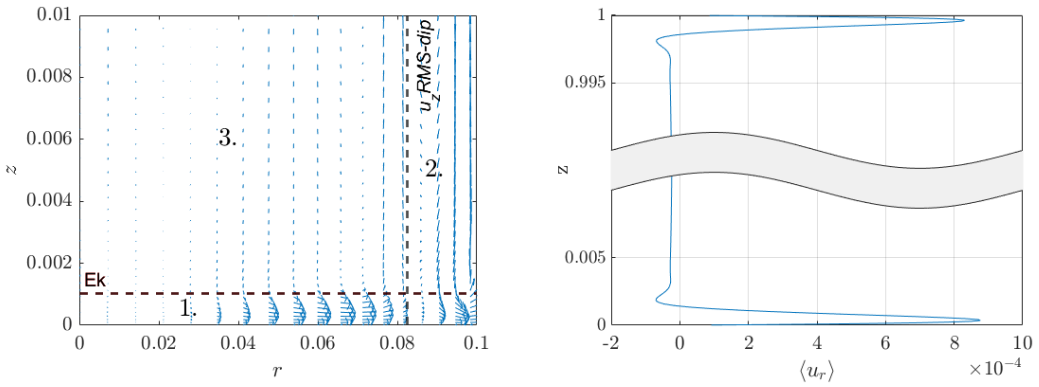

(a) u_r-u_z vector field close to the bottom plate, displaying the Ekman (1) and sidewall (2) boundary layers and the bulk region (3).

(b) Averaged radial velocity as function of height, showing the presence and thickness of the Ekman boundary layers.

Figure 4.8: Ekman boundary layers for $Ra = 4.3 \times 10^{11}$.

The averaged radial velocity of the Ekman boundary layer, i.e. averaged in time, over the thickness of the boundary layer and in the radial direction, is displayed in fig. 4.9 for the top and bottom Ekman boundary layer. The figure shows an increasing radial velocity as a function of Rayleigh, with its zero-crossing around $Ra = 9.9 \times 10^{10} - 1.4 \times 10^{11}$. This means that for the low Ra cases the mean radial velocity in the Ekman boundary layer is negative, resulting in an Ekman suction from the Ekman region into the bulk region. For high Ra cases, the situation is the opposite, with a net Ekman pumping flow from the bulk region into the bottom and top boundary layers. This supports the earlier found results of the relative strength of the wall mode (fig. 4.5b) and the thickness of the thermal boundary layer (fig. 4.7a) that there are two different kinds of wall modes, with the transition around $Ra = 1.4 \times 10^{11}$.

4.1.4 Nusselt number

In section 2.4, five different methods are described to calculate the average Nusselt number. The Nusselt number is calculated using all five methods and weighted averaged while taking the uncertainty into account (Taylor [1997]) (appendix C.1). All individual Nusselt numbers and their uncertainties are displayed in appendix C.2. The averaged results are displayed in fig. 4.10, marked with the red diamonds. The figure shows that the Nusselt number of the new simulations are in accordance with the previously found results of De Wit et al. [2020] (green diamonds), and following the data points that are found experimentally by Cheng et al. [2015] (red dots).

Following De Wit et al. [2020], the $u_z RMS\text{-}dip$ sidewall boundary layer definition, described

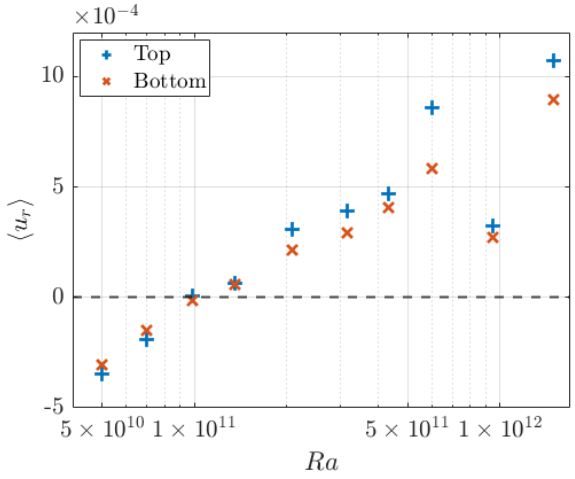

Figure 4.9: Averaged radial velocities in the Ekman boundary layers as a function of the Rayleigh number.

in section 4.1.2, is used to separate the flow into a wall and a bulk region. The local Nusselt number of the bulk region, i.e. the surface that is enclosed by the radius using the $u_z RMS\text{-}dip$ definition, is calculated at mid-height ($z = 0.50$), using eq. (2.20). The results are displayed with the red open diamonds in fig. 4.10. The new simulations are in line with the inner Nusselt numbers found by De Wit et al. [2020] (open blue diamonds), showing a large gap between the overall Nusselt number and the Nusselt number of the bulk. For simulations with $Ra \geq 1.4 \times 10^{11}$, the split into two branches of Nusselt numbers is visible, where the Nusselt numbers of the bulk part have a Nusselt number that is comparable with the numbers of the periodic simulations of Aguirre Guzmán [2021] (light orange open squares).

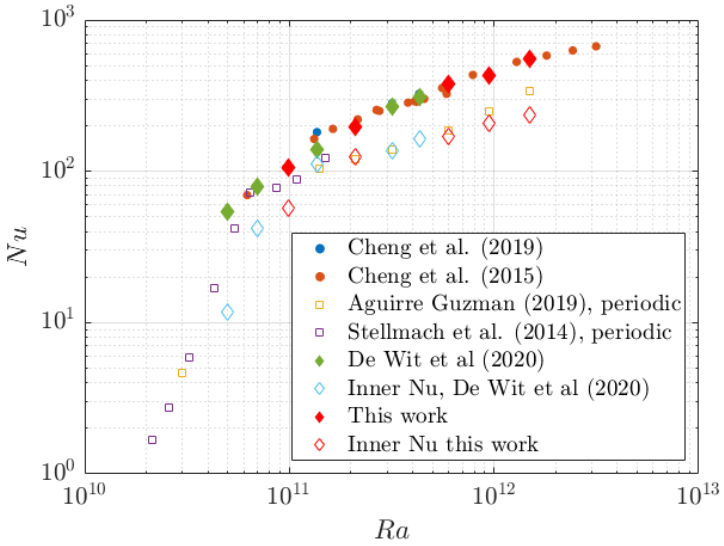

Figure 4.10: Nusselt number as a function of Rayleigh. The boundary layer definition $u_z RMS\text{-}dip$ is used to extract the 'inner Nu' from the total Nusselt number.

The Nusselt number dependence on the Rayleigh number of the bulk and wall region, together with the overall Nusselt number are displayed in fig. 4.11 for two different boundary layer definitions: $u_z RMS\text{-}dip$ and $\langle u_\theta \rangle = 0$. Looking at the overall Nusselt number (Nu

total), an continuously increasing relation is found. This is caused by a larger temperature difference, i.e larger thermal forcing, which causes larger vertical velocities, resulting in a larger Nusselt number. For $Ra \leq 1.4 \times 10^{11}$, the increase in overall heat transport is caused by an increase of heat transport of the bulk region, whereas the heat transport in the boundary region remains constant. For $Ra \geq 1.4 \times 10^{11}$ both wall and bulk Nusselt numbers increase. An attentive reader would observe that for most Ra, both the local Nusselt number of the bulk and the local Nusselt number of the wall region are higher for the $\langle u_\theta \rangle = 0$ boundary layer definition, compared to the local Nu belonging to the $u_z RMS\text{-}dip$ definition, whereas the total Nusselt number is the same. This is due to the different boundary layer definitions the local Nu is averaged over different areas, resulting in these paradoxical results.

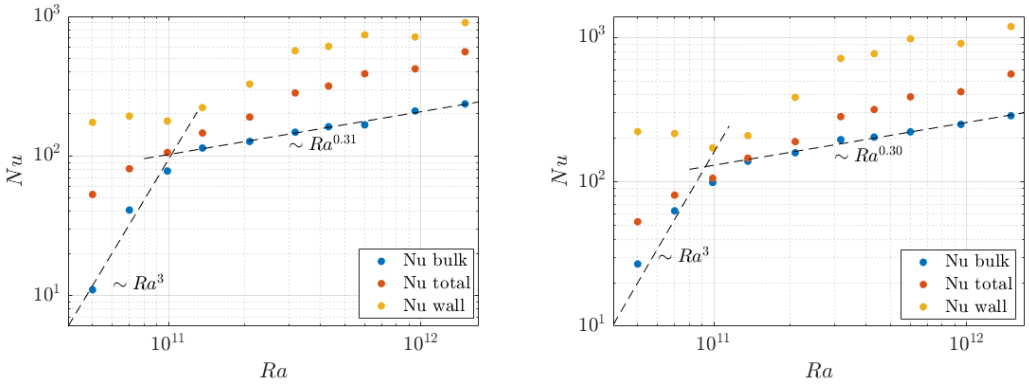

(a) Nusselt number of bulk, wall and total, with $u_z RMS\text{-}dip$ as boundary layer definition.

(b) Nusselt number of bulk, wall and total, with $\langle u_\theta \rangle$ as boundary layer definition.

Figure 4.11: Bulk, wall and total Nusselt Number as functions of Rayleigh using $u_z RMS\text{-}dip$ and $\langle u_\theta \rangle$ as boundary layer definitions.

In fig. 4.11 for $Ra \leq 9.9 \times 10^{10}$ a line with Ra^3 is plotted for the Nusselt number of the bulk. This is in accordance with the power-law found by Stellmach et al. [2014]. The strong increase of the Nusselt number of the bulk (open diamonds in fig. 4.10) for $Ra \leq 1.4 \times 10^{11}$ can be explained by the Ekman suction from the top and bottom boundary regions into the bulk, which is observed for the lowest Ra cases (see fig. 4.9). The Nusselt numbers of the bulk with $Ra \geq 1.4 \times 10^{11}$ are fitted with $Nu \sim Ra^\alpha$ for both boundary layer definitions, resulting in $\alpha = 0.31 \pm 0.04$ and $\alpha = 0.30 \pm 0.04$ for $u_z RMS\text{-}dip$ and $\langle u_\theta \rangle$ respectively. These values agree reasonably well with the $\alpha = 0.322$ power-law which was found by Cheng et al. [2015] for not rotation-dominated flows. So, for $Ra \geq 1.4 \times 10^{11}$ the thermal forcing (Ra) dominates over the rotational force (Ek) resulting in a Ra dependence of the heat transfer that scales with $\alpha = 0.322$, whereas for $Ra \leq 1.4 \times 10^{11}$,which is for this Ek in the regimes of CTC's (section 2.5), the Nusselt number reasonably matches with the Ra^3 line (Stellmach et al. [2014]). So, for the Nusselt number of the bulk the same transition from power law scaling takes place as observed for the cylinder as a whole (Cheng et al. [2015]).

As displayed in fig. 4.6, the lowest correlation of the cosine fit through the vertical velocity profile in the boundary region is observed for $Ra = 1.4 \times 10^{11}$. This agrees with the relatively low Nusselt number in the boundary region in this case (fig. 4.11). In fig. 4.12 the Nusselt number as a function of time and the fitting coherence of the cosine through the vertical velocity profile (R^2) are displayed for $Ra = 1.4 \times 10^{11}$ and $Ra = 2.1 \times 10^{11}$, i.e. the two cases with the lowest R^2. The figure clearly shows that fluctuations of the overall Nusselt number are mainly caused by fluctuations of the vertical coherence, and thus the heat transport in the boundary region, whereas the Nusselt number of the bulk is more or less constant in time (fig. 4.12a and 4.12b).

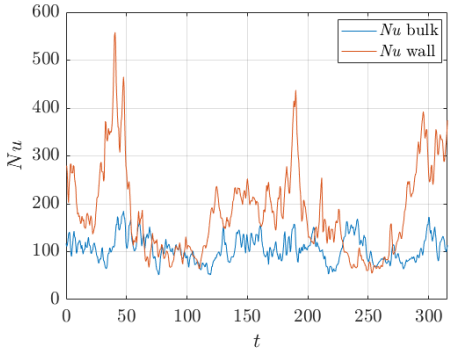

(a) Nusselt number in time for $Ra = 1.4 \times 10^{11}$.

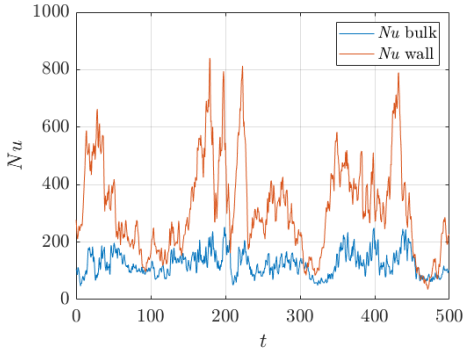

(b) Nusselt number in time for $Ra = 2.1 \times 10^{11}$.

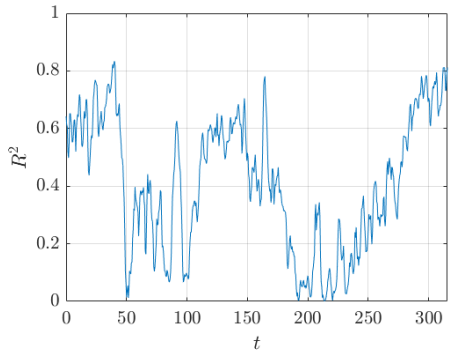

(c) R^2 in time for $Ra = 1.4 \times 10^{11}$.

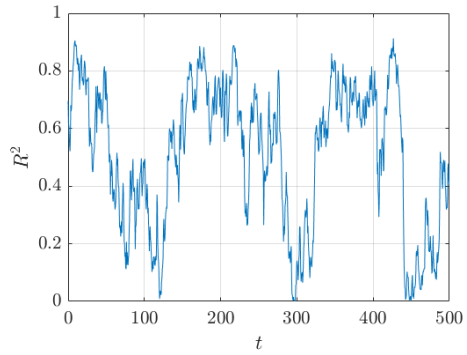

(d) R^2 in time for $Ra = 2.1 \times 10^{11}$.

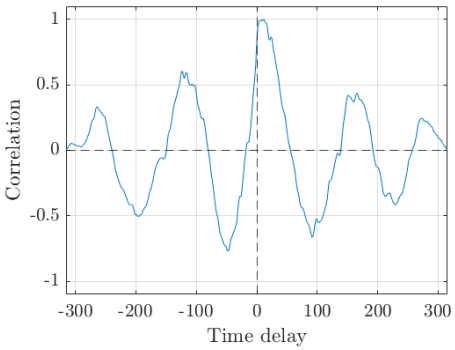

(e) Cross-correlation for $Ra = 1.4 \times 10^{11}$.

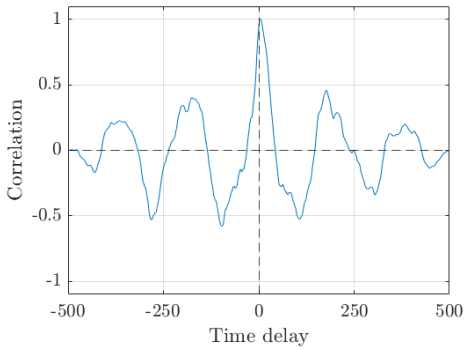

(f) Cross-correlation for $Ra = 2.1 \times 10^{11}$.

Figure 4.12: Nusselt number and R^2 as functions of time, together with their cross-correlation for $Ra = 1.4 \times 10^{11}$ and $Ra = 2.1 \times 10^{11}$.

There is a clear correlation between the heat transport in the boundary region and the degree of coherence of the cosine fit through the vertical velocity field, i.e. peaks and troughs of the Nusselt number in the wall region correspond with peaks and troughs of R^2. Cross-correlation calculations of the Nusselt number in the boundary region and the R^2 (fig. 4.12e and 4.12f) show for $Ra = 1.4 \times 10^{11}$ a Nusselt number signal that is a time gap $\tau = 11.5$ later, relative to the R^2 value. For $Ra = 2.1 \times 10^{11}$ the Nusselt number is a time gap $\tau = 5$ later. The cross-correlation is performed for the other simulations too, showing in all cases a later Nusselt number signal, with an average of $\tau = 5 \pm 3$. The delay of the Nu signal means that a well-established wall mode results in high Nusselt numbers.

The strongly fluctuating R^2 value, with sometimes almost zero correlation, indicates that

around these Rayleigh numbers ($Ra = 1.4 \times 10^{11} - 2.1 \times 10^{11}$) the wall mode structure vanishes at certain times. This behavior of appearing and disappearing is not found for the other Rayleigh numbers, indicating that around these Ra the wall mode is very unstable and probably a transition between two different wall mode regimes takes place.

4.1.5 Wall mode fitting

Inspired by the theoretical studies of wall modes by Herrmann and Busse [1993] and Zhang and Liao [2009] the wall mode pattern is approached in a more theoretical way to get an insight into how the shape (amplitude, thickness) of the wall mode changes as a function of Ra. The vertical velocity field of the wall mode is mathematically approximated by a sine wave in azimuthal direction combined with a radially inward damped sine. This is mathematically represented as

$$u_z(r,\theta) = A_z \cdot \sin((r-0.1)\cdot B_z)\cdot \sin(\theta + C_z)\cdot \exp(-(0.1-r)\cdot D_z), \tag{4.3}$$

with A_z the amplitude scale factor, B_z a scaling for the radial wavenumber, C_z the azimuthal shift of the vertical profile relative to its origin and D_z the radial (inward) damping factor. Note that $\sin(\theta + C_z)$ is used instead of $\sin(F\cdot\theta + C_z)$ because in all Ra cases a wave profile with $n = 1$ in the azimuthal direction is observed for the vertical velocity field. Using the $(r - 0.1)$ notation forces the velocity to be zero at the sidewall (no-slip). As an example, the simulated and approximated vertical velocity fields of $Ra = 4.3 \times 10^{11}$ are displayed in fig. 4.13. The figures show a great coherence concerning boundary layer width and amplitude. Whereas fitting parameter C_z is just a phase constant, attention is paid to the amplitude (A_z), radial wavenumber (B_z), and damping (D_z) parameters.

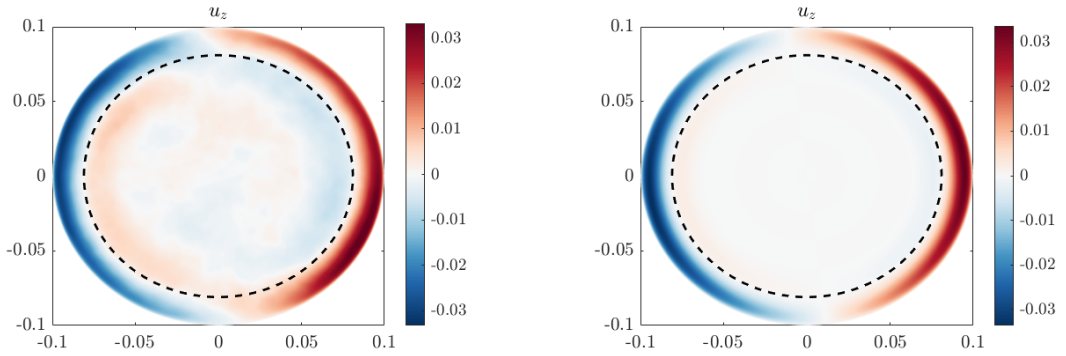

(a) Simulation **(b)** Mathematical approximation

Figure 4.13: Simulated and approximated vertical velocity profiles for $Ra = 4.3 \times 10^{11}$ at $z = 0.50$, with the $u_z RMS\text{-}dip$ boundary displayed with the dashed circle.

To compare the fitting parameters of the different fits correctly, the velocities are made dimensionless in viscous units according to eq. (2.16), changing the velocity dimensionless $u_z/U_{free-fall}$ into $u_z/(\nu/H)$.

Eq. (4.3) is applied for the no-slip simulations at mid-height using a 3D-least square fitting algorithm. The fitting parameters as functions of the Rayleigh number are displayed in fig. 4.14 and their corresponding equations in table 4.1. The radial wavenumber (B_z), which is a parameter for the first zero-crossing of the vertical velocity profile (i.e. the boundary layer thickness), shows a monotonous behavior, in accordance with the definition of $u_z RMS\text{-}dip$ of fig. 4.7a. Note that the equation of the radial wavenumber (B_z) is the inverse of the boundary layer thickness equation of $u_z RMS\text{-}dip$. The boundary layer thickness is

the wavelength of the vertical structure in the radial direction, which is the inverse of the wavenumber (B_z) in the radial direction. The amplitude (A_z) and damping (D_z) parameters both show a discontinuous relation, with the breaking point around the fourth data point ($Ra = 1.4 \times 10^{11}$). For the low Ra cases, a constant amplitude (A_z) is observed. This could be the explanation for the (almost) constant Nusselt number in the boundary region (fig. 4.11) for low Rayleigh numbers. For $Ra \geq 1.4 \times 10^{11}$ an increase of wall mode amplitude is observed, which can be explained by the increasing velocity scales for increasing Rayleigh number and the change of sign of radial velocity in the Ekman layer (see fig. 4.9), resulting in a net transport from the Ekman boundary layer into the sidewall boundary layer. The damping factor (D_z) causes an exponential damping for smaller radial values, i.e. lower amplitudes when moving radially inwards. Further, the damping factor (D_z) has an impact on the shape of the sinusoidal flow profile in the boundary region, i.e. larger damping factor causes a more asymmetric sinusoidal lobe in the wall region. Without damping, the sinusoidal wave (as a function of r) will be perfectly symmetric. Adding a damping factor results in a steep profile close to the sidewall boundary. For the lowest Rayleigh cases, a constant damping is observed: the amplitude difference between the first vertical flow lobe and the second (radially inward) lobe is constant and the shape of the lobes is constant too for different Rayleigh numbers. For larger Ra, an increase in damping factor is observed, i.e. the second lobe becomes weaker and the shape of the first lobes becomes more asymmetric. This behavior is observed in fig. 4.5a too, where the $u_z RMS$ profile becomes more asymmetric, for increasing Rayleigh number.

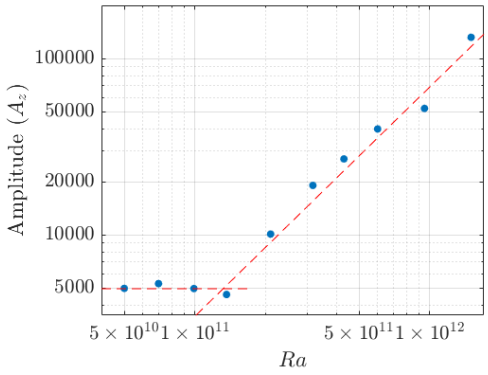

(a) Wall mode amplitude (A_z) as function of Ra.

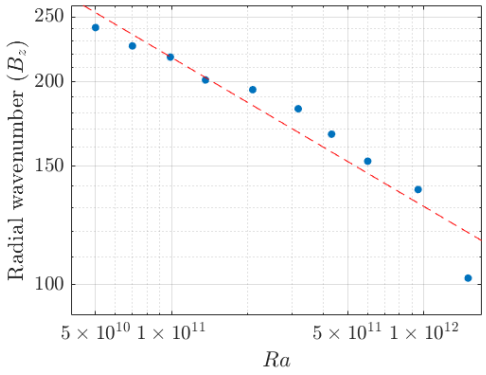

(b) Radial wavenumber (B_z) as function of Ra.

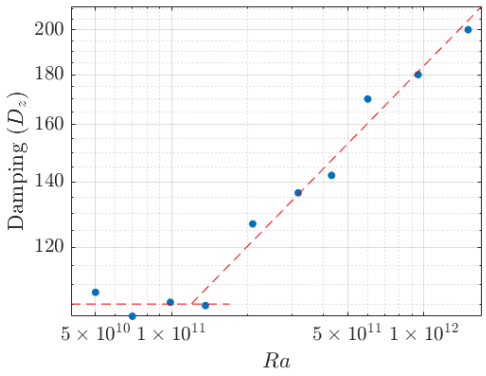

(c) Damping (D_z) as a function of Ra.

Figure 4.14: Viscous dimensionless fitting parameters as function of the Rayleigh number.

The same fitting procedure using eq. (4.3) is also applied at $z = 0.25$ and $z = 0.75$ to get an insight into the vertical dependence of the vertical flow field. The results (fig. App. A.1) show the same shapes of graphs as displayed in fig. 4.14. Differences are that the vertical

	Low Ra	High Ra
Amplitude (A_z)	4952	$(1.7 \times 10^{-11}) \cdot Ra^{1.30}$
Radial wavenumber (B_z)	$(5.9 \times 10^4) \cdot Ra^{-0.22}$	$(5.9 \times 10^4) \cdot Ra^{-0.22}$
Damping (D_z)	107	$(0.13) \cdot Ra^{0.26}$

Table 4.1: Equations belonging to the fitting parameters of the viscous dimensionless velocity fields.

flow field in the boundary at $z = 0.25$ and $z = 0.75$ have a lower amplitude (A_z), larger radial wave number (B_z) (so smaller sidewall boundary layer), and a larger damping factor (D_z) compared to the observations at $z = 0.50$. The fitting parameters at $z = 0.25$ and $z = 0.75$ are comparable, indicating that the vertical flow is mirror-symmetric in $z = 0.50$, with its maximum at mid-height and its minimum at the bottom and top plate. Doing the same analysis at $z = 0.10$ confirms the estimated profile with the lowest amplitudes close to the bottom (and top) plate.

4.2 Stress-free sidewall

Two simulations are performed with stress-free sidewall boundaries: $Ra = 5.0 \times 10^{10}$ and $Ra = 3.2 \times 10^{11}$. Note that in these cases the top and bottom boundaries are not stress-free. The RMS of the vertical velocity of both cases is displayed in fig. 4.15a. For comparison the u_zRMS of the no-slip cases is displayed in fig. 4.15b. Here it is visible that the stress-free simulations have their maximum u_zRMS values at the sidewall boundary, with a larger amplitude. The RMS of the bulk (approx. $0 < r < 0.08$) of the lowest Ra case is almost identical in both cases (no-slip and stress-free), whereas for the largest Ra, the RMS of the stress-free bulk is much lower. This difference suggests that the flow field for $Ra = 3.2 \times 10^{11}$ is significantly different compared to the stress-free case.

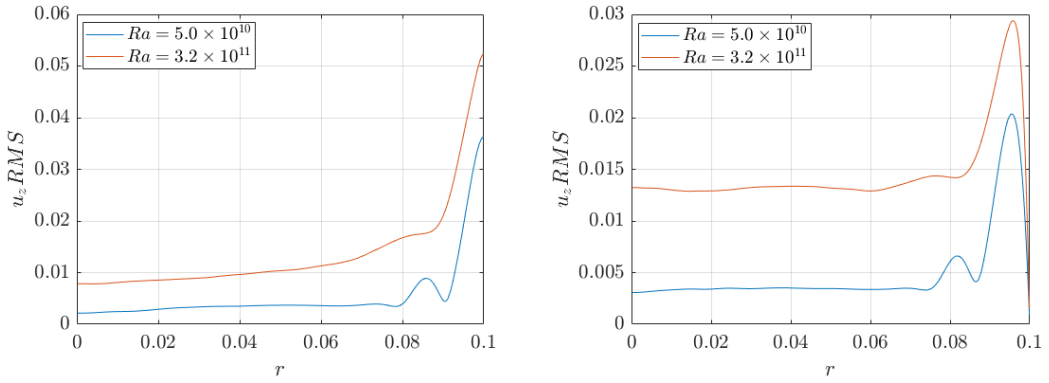

(a) u_zRMS as a function of r for the stress-free sidewall boundary.

(b) u_zRMS as a function of r for the no slip sidewall boundary.

Figure 4.15

The vertical velocity fields in the boundary region of the stress-free simulations precess in the azimuthal direction too. The precession path of both simulations, compared with the no-slip simulations, are displayed in fig. 4.16. The angular drift of the stress-free simulation with $Ra = 3.2 \times 10^{11}$, which remarkably precesses in the positive/cyclonic direction, is multipied with -1 for comparison. The sinusoidal functions, to measure the phase shift (and amplitude), are fitted at the sidewall boundary, because u_zRMS is maximal here (see fig. 4.15a). The figures show that for the lowest Ra case the precession speed is much slower for the stress-free simulation, whereas for $Ra = 3.2 \times 10^{11}$ the precession speed is almost equal, but in the opposite direction . A prograde rotating wall mode is earlier observed in

simulations of Horn and Schmid [2017], showing that this observed phenomenon is not unique.

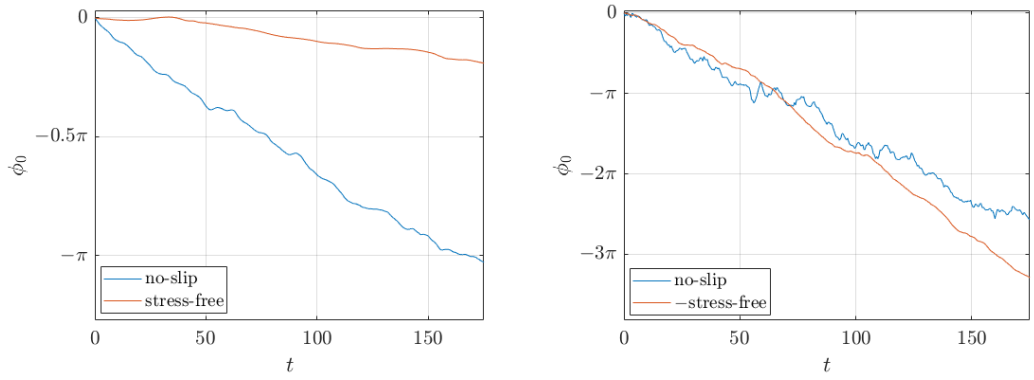

(a) $Ra = 5.0 \times 10^{10}$ **(b)** $Ra = 3.2 \times 10^{11}$

Figure 4.16: Azimuthal orientation of the wall mode as functions of time. The stress-free drift of $Ra = 3.2 \times 10^{11}$ has its sign flipped for plotting convenience. The slower rotation for $Ra = 5.0 \times 10^{10}$ and equal rotation but in the opposite direction for $Ra = 3.2 \times 10^{11}$ are visible.

For $Ra = 3.2 \times 10^{11}$, the lines of the azimuthal phase shift in time (fig. 4.16) are much smoother, i.e. have fewer irregularities, for the stress-free sidewall case compared to the no-slip case, suggesting that this stress-free mode is more coherent and precesses with a constant velocity. This behavior is also found for the coherence (R^2) of the wall mode. A fitting coherence of $R^2 = 0.84 \pm 0.10$ is found for the stress-free case, which is much higher than for the no-slip case ($R^2 = 0.65 \pm 0.13$). This means that the spread of data points relative to the size of the sinusoidal profile is less for the stress-free case. The coherence of the no-slip simulation with $Ra = 5.0 \times 10^{10}$ is already high ($R^2 = 0.88 \pm 0.04$), so no significant difference is observed here (stress free: $R^2 = 0.89 \pm 0.03$). So, the wall mode of the stress-free simulations is more stable and precesses with a more constant precession rate.

The precession speed of the wall mode is used to generate a rotation average of the flow profiles at mid-height. The flow profiles of the rotation corrected averages are compared with the no-slip simulations at mid-height. The stress-free simulations of $Ra = 5.0 \times 10^{10}$ show minor differences in flow structure at mid-height (appendix D.1 and D.2); the boundary region of the vertical flow profile is narrower, with a higher amplitude, whereas the azimuthal and radial flow profiles almost match. The flow fields at mid-height for both the no-slip and stress-free case for $Ra = 3.2 \times 10^{11}$ are displayed in fig. 4.17. The vertical flow profile is displayed in fig. 4.17a and fig. 4.17d, showing a narrower boundary layer with a higher amplitude. The radial velocity field also shows more or less the same profile, but with a lower amplitude. The azimuthal velocity profile no longer has its 4 lobe structure with prograde and retrograde sections, but it is separated in a prograde rotating wall region and a retrograde rotating bulk region.

The boundary layer widths of the stress-free simulations are calculated using both $u_z RMS$-*dip* (eq. (4.2)) and the $\langle u_\theta \rangle = 0$ definitions. Their widths, together with the widths of the no-slip cases, are tabulated in table 4.2. For the $u_z RMS$-*dip* definition in both cases, a boundary layer is observed which is 0.004 narrower in the stress-free case. This distance is equal to the distance between the $u_z RMS$-*peak*'s and the sidewall in fig. 4.15b, This distance is almost the thickness of the $Ek^{1/3}$-boundary layer that connects the sidewall flow to the sidewall and is logically missing for stress-free sidewall conditions. Using the $\langle u_\theta \rangle = 0$ definition, a narrower boundary layer is observed for the lowest Ra case, which can be explained by the stress-free sidewall. The $Ra = 3.2 \times 10^{11}$ case shows a much wider boundary based on the

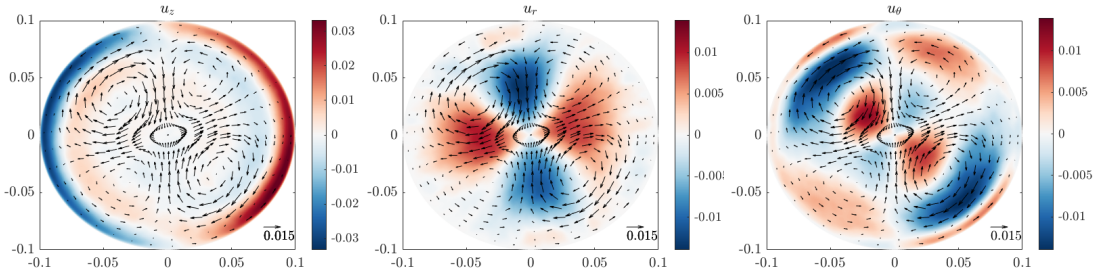

(a) No-slip vertical velocity. **(b)** No-slip radial velocity. **(c)** No-slip azimuthal velocity.

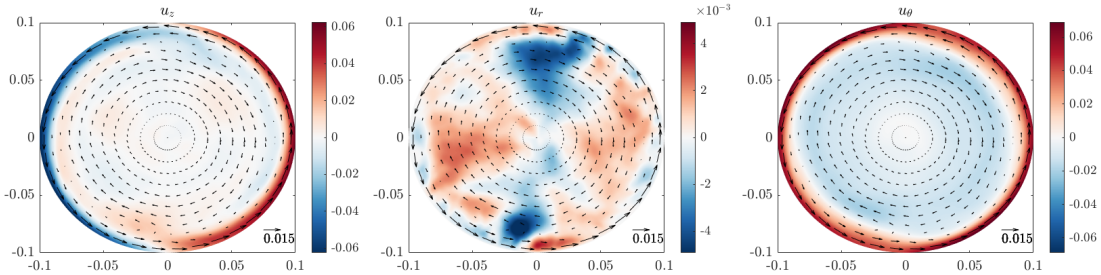

(d) Stress-free vertical velocity. **(e)** Stress-free radial velocity. **(f)** Stress-free azimuthal velocity.

Figure 4.17: Rotation averaged velocity profiles at mid-height for $Ra = 3.2 \times 10^{11}$ for no-slip fig.(a)-(c) and stress-free fig.(d)-(f) sidewall boundaries.

$\langle u_\theta \rangle = 0$ definition in the stress-free case. This boundary width coincides with the boundary layer width based on the $u_z RMS\text{-}dip$ definition of the stress-free case. This means that the vertical and azimuthal velocity are zero at the same radial distance, which results, combined with the lower radial velocities in the stress-free case (fig. 4.17e), in a strong decoupling of the wall region from the bulk region. Note that the shape of the vertical flow structure stays the same for stress-free and no-slip sidewall conditions, whereas the azimuthal flow structure drastically changes. This means that a general definition of the thickness of the wall mode can better be based on the vertical velocity.

Ra	5.0×10^{10} (ns)	5.0×10^{10} (sf)	3.2×10^{11} (ns)	$3.2 \cdot 10^{11}$ (sf)
$u_z RMS\text{-}dip$	0.014	0.010	0.019	0.015
$\langle v_\theta \rangle = 0$	0.007	0.005	0.009	0.015

Table 4.2: Boundary layer thicknesses of simulations with stress-free (sf) and no-slip (ns) sidewall boundaries.

Since the Ekman number for the stress-free and no-slip sidewall boundaries is the same, the thickness of the top and bottom Ekman boundary layers is conserved too. The average radial velocity in the Ekman boundary layer is calculated for the stress-free cases too and is tabulated in table 4.3, where the averaged velocity of both the top and bottom boundary layer is displayed. For the lowest Ra, a small difference is observed, which agrees with previous observations that the flow profile is almost identical for the stress-free and no-slip boundary conditions. For $Ra = 3.2 \times 10^{11}$ a larger radial velocity in the Ekman boundary is observed, which has comparable amplitude to the no-slip simulation with $Ra = 1.5 \times 10^{12}$.

The total Nusselt number is calculated using the 5 methods described in section 2.4 and averaged. The local Nusselt number at mid-height for both the boundary and bulk region are calculated using (eq. (2.20)). The Nusselt numbers and the numbers of the previously found no-slip cases are displayed in table 4.4. The results show for $Ra = 5.0 \times 10^{10}$ larger Nusselt

Ra	5.0×10^{10} (ns)	5.0×10^{10} (sf)	3.2×10^{11} (ns)	3.2×10^{11} (sf)
$\langle u_r \rangle$	-3.2×10^{-4}	-2.5×10^{-4}	3.4×10^{-4}	1.25×10^{-3}

Table 4.3: Averaged radial velocity in the Ekman boundary layer for stress-free (sf) and no-slip (ns) sidewall boundaries.

numbers (local and total) which can be explained by the overall higher vertical velocity due to the stress-free boundaries at equal Rayleigh number, whereas the overall flow profile stays the same. The total Nusselt number analysis is displayed in appendix C.3.

For $Ra = 3.2 \times 10^{11}$ the flow profile for the stress-free simulation (fig. 4.17) is different, with a lower radial velocity, resulting in a larger decoupling between the bulk and the boundary region. This stronger decoupling results in a lower Nusselt number of the bulk and an even higher Nusselt number of the boundary region. The large gap between the Nu_{bulk} for stress-free simulations and Nu_{bulk} of no-slip simulations suggest that the latter is still fed by heat transport from the boundaries.

Ra	5.0×10^{10} (ns)	5.0×10^{10} (sf)	3.2×10^{11} (ns)	3.2×10^{11} (sf)
Nu_{bulk}	11.5	15.0	154.2	72.3
Nu_{wall}	174.5	249.4	544.8	994.3
Nu_{total}	53.2	58.8	280.0	325.1

Table 4.4: Nusselt number of simulations with stress-free (sf) and no-slip (ns) sidewall boundaries.

The rotation averaging is applied at $z = 0.25$ and $z = 0.75$ too. The results are displayed in appendix D.2. The vertical velocity field has its maximum amplitude at mid-height and lower maximum velocities at $z = 0.25$ and $z = 0.75$, which is the same behavior as observed for the no-slip boundary simulations. The radial velocity field has its lowest amplitudes at mid-height and higher velocities at $z = 0.25$ and $z = 0.75$. The vertical and radial velocity fields further show no height-dependent behavior. The azimuthal velocity field is displayed in fig. 4.18 (first column). At mid-height, the azimuthal velocity field is almost symmetric, with a prograde rotating ring and a retrograde rotating core. The rotating averages at $z = 0.25$ and $z = 0.75$ are almost the same but mirrored. Both cross-sections have a narrow half-ring with a high azimuthal velocity and a wide half-ring with relatively low azimuthal velocity. This phenomenon could be approximated by a superposition of a narrow prograde rotating ring (second column of fig. 4.18) combined with a second double-ring structure with prograde and retrograde sections (third column of fig. 4.18) with half the amplitude compared to the second column. This pattern should be mirrored at mid-height, where its amplitude is equal to zero at $z = 0.50$. Combining these two fields is displayed in the fourth column of fig. 4.18. These figures show large degrees of coherence with the simulation results displayed in the first column, suggesting that the wall mode which is present in the simulations is a superposition of the 2 minor effects described in columns 2 and 3.

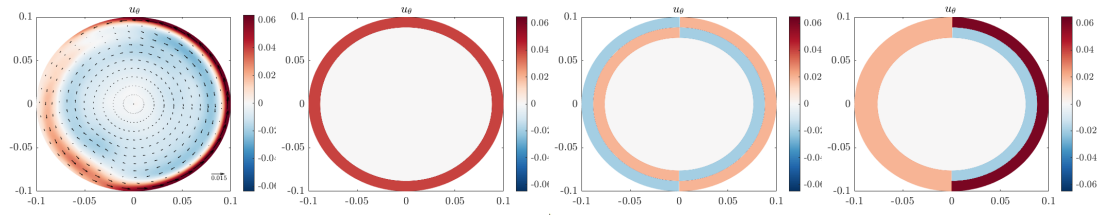

(a) $z = 0.25$ simulation **(b)** constant field. **(c)** pro/retrograde field. **(d)** superposition.

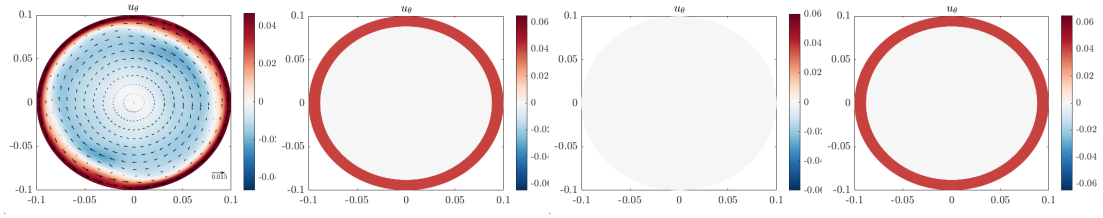

(e) $z = 0.50$ simulation **(f)** constant field **(g)** pro/retrograde field **(h)** superposition

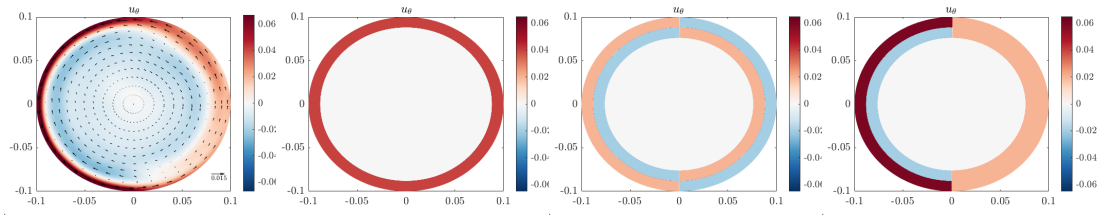

(i) $z = 0.75$ simulation **(j)** constant field **(k)** pro/retrograde field **(l)** superposition

Figure 4.18: Mean azimuthal flow profile at $z = 0.25, 0.50$ and 0.75 (column 1) for $Ra = 3.2 \times 10^{11}$ with stress-free sidewall conditions. The simulation azimuthal field can be explained by a superposition of a constant height-independent rotating ring (column 2) and prograde-retrograde structure which changes sign at $z = 0.50$. This results in column 4, which shows large degrees of similarities with column 1.

.

5 Results and Discussion: Bulk mode

In this chapter, the flow pattern in the bulk will be analyzed. First, a distinction between two different flow structures will be made: structures observed for low and high Rayleigh numbers. The overall flow structure will be analyzed using the RMS at different heights. The simulations with low Rayleigh numbers will be analyzed qualitatively, where the general flow structure will be explained. The simulations with high Rayleigh numbers will be analyzed more quantitatively because the periodic structure makes it possible to approach the structures mathematically. The observed bulk mode of the azimuthal velocity will be subtracted from the observed profiles, resulting in an isolated azimuthal wall mode. This wall mode will be compared with the vertical wall mode that is discussed in chapter 4. Finally, these observed and modeled structures will be compared with bulk mode structures from theory. The results of the stress-free simulations will not be discussed in detail, whereas the bulk flow of $Ra = 3.2 \times 10^{11}$ is already discussed in section 4.2 and the bulk flow of $Ra = 5.0 \times 10^{10}$ is identical to the simulation with no-slip sidewalls (see appendix D.1 and appendix D.2).

The velocity profile in the bulk (approx. $0 < r < 0.08$) is dominated by the radial and azimuthal velocities, which are characterized by their flow profile with azimuthal wavenumber $n = 2$ (fig. 4.4). In the previous chapter, a clear distinction is found between the two parts of flow structures (i.e. bulk region and wall region). Simulations with $Ra \leq 1.4 \times 10^{11}$ are characterized with a vertical wall mode structure with an (almost) constant amplitude and a strong increase of the Nusselt number of the bulk, whereas for $Ra \geq 1.4 \times 10^{11}$ the wall mode amplitude increases as a function of Rayleigh.

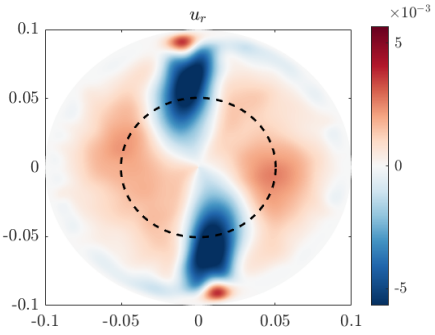

(a) $Ra = 5.0 \times 10^{10}$.

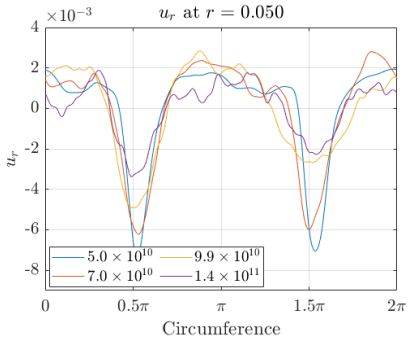

(b) u_r profile at $r = 0.050$ for $Ra < 2.1 \times 10^{11}$.

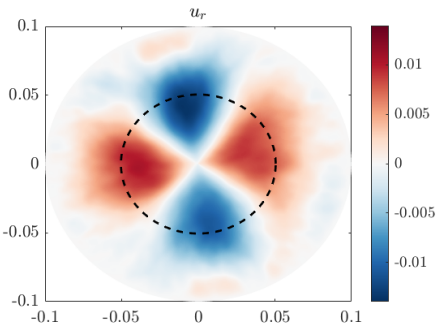

(c) $Ra = 4.3 \times 10^{11}$.

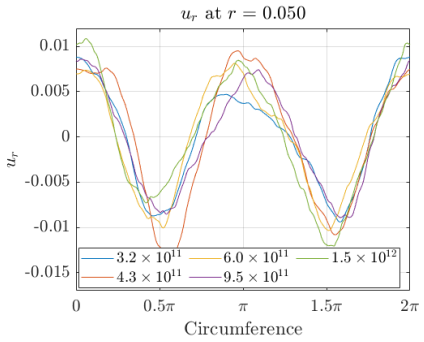

(d) u_r profile at $r = 0.050$ for $Ra > 2.1 \times 10^{11}$.

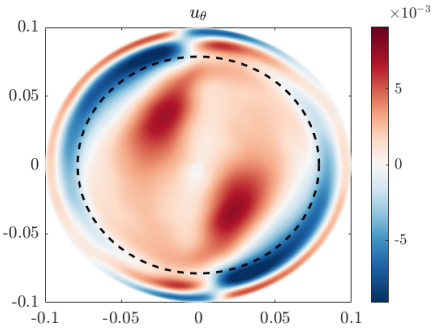

(e) $Ra = 5.0 \times 10^{10}$.

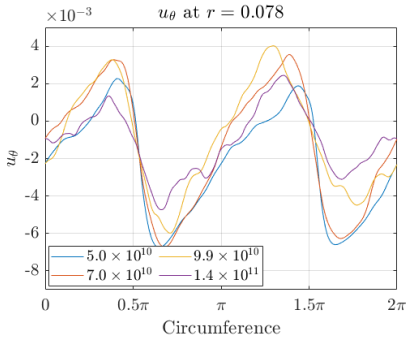

(f) u_θ profile at $r = 0.078$ for $Ra < 2.1 \times 10^{11}$.

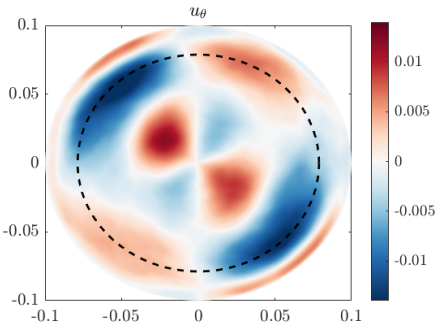

(g) $Ra = 4.3 \times 10^{11}$.

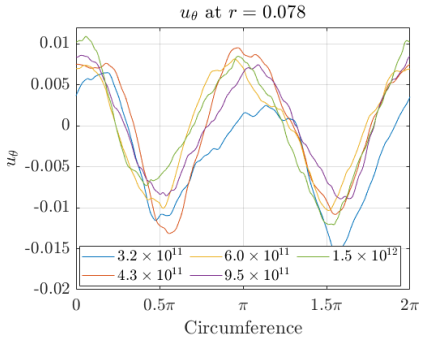

(h) u_θ profile at $r = 0.078$ for $Ra > 2.1 \times 10^{11}$.

Figure 5.1: Separation of the rotation averaged radial and azimuthal velocity fields at mid-height ($z = 0.50$) in a low $Ra < 2.1 \times 10^{11}$ and high $Ra > 2.1 \times 10^{11}$ Ra regime, based on their flow characteristics. Exemplaric displayed for $Ra = 5.0 \times 10^{10}$ (low Ra) in fig.(a),(e) and 4.3×10^{11} (high Ra) in fig. (c),(g). The velocity profiles along the dashes circles of the figures is displayed in fig.(b),(d),(f) and (h).

This change of flow behavior is also found for the radial and azimuthal velocity profiles, as displayed in fig. 5.1. These figures display averages of the radial and azimuthal velocity, where the wall mode precession is used to rotation average the flow profile. Theoretically, the wall modes precess with a larger velocity than the bulk mode (Favier and Knobloch [2020]), so our approach is theoretically not appropriate. We tried to improve the rotation averaging of the bulk by using a large range of precession rates. This resulted in more smoothed graphs with lower maximum amplitudes, which suggests that in these simulations the wall and bulk mode precess with the same rate. The results of the rotation averaged flow profiles at $z = 0.25$, 0.50, and 0.75 are displayed in appendix D.1.

For low Rayleigh ($Ra < 2.1 \times 10^{11}$), there are two strong inward jets found (e.g. fig. 5.1a), combined with a large background region of radially outward flow. For high Rayleigh ($Ra > 2.1 \times 10^{11}$) the flow profile is more like a symmetric profile with in- and outward velocity sections (e.g. fig. 5.1c). In fig. 5.1b and fig. 5.1d the velocity in the radial direction at $r = 0.050$ (dashed circle) is displayed for the different flow sections. fig. 5.1b clearly shows the local inward jets combined with a larger region with weak radially outward flow, whereas fig. 5.1d shows a more sinusoidal shaped profile for the high Rayleigh cases and a four lobe structure.

The same distinction is observed for the velocity profiles in the azimuthal direction, where the profiles can be separated for Rayleigh being larger or smaller than 2.1×10^{11}. For the lowest Rayleigh cases (fig. 5.1e and 5.1f) a saw-tooth profile of the azimuthal flow profile is observed at $r = 0.078$, whereas for high Rayleigh cases a sinusoidal profile is observed (fig. 5.1g and

5.1h). Using exact this distance ($r = 0.078$) the dashes circle is located in all simulations in the second lobe when moving radially inward.

In the following chapters the results of the 'Low Rayleigh'-cases ($Ra < 2.1 \times 10^{11}$) and 'High Rayleigh'-cases ($Ra > 2.1 \times 10^{11}$) with be analyzed separately.

In fig. 5.2 the azimuthally and temporally averaged data of the RMS of the azimuthal velocity field are displayed. The azimuthal flow structure is symmetric in $z = 0.50$, resulting in identical RMS graphs at $z = 0.25$ and $z = 0.75$, only the latter is displayed here. For completeness, the RMS graph at $z = 0.25$ is displayed in appendix B. The figures show increasing velocity scales with increasing Ra, the same as observed for the vertical velocity field. Further, at $z = 0.75$ (and thus also at $z = 0.25$) a large $u_\theta RMS\text{-}peak$ is observed close to the sidewall, which indicates the presence of region with well pronounced positive and negative velocities, i.e. prograde and retrograde rotating velocity structures. The sidewall located peak in RMS-value is not observed at mid-height ($z = 0.50$), indicating an anti-symmetric profile. The RMS-values of the bulk (approx. $0 < r < 0.08$) show a wavy behavior, indicating that there is a kind of sinusoidal profile present in the bulk.

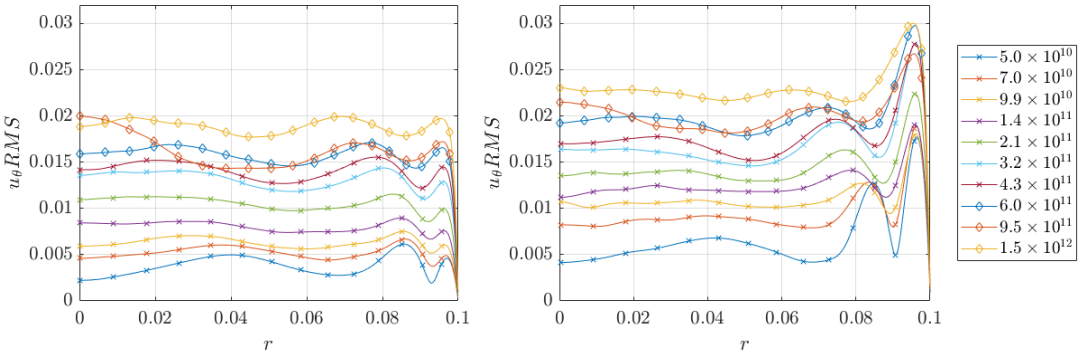

(a) $z = 0.50$ **(b)** $z = 0.75$

Figure 5.2: Root mean squares of the azimuthal velocity for different Rayleigh numbers at 0.50 and 0.75. The figures show a peak in RMS-value close to the boundary at 0.75, which is not observed for $z = 0.50$.

In fig. 5.3 the mean azimuthal velocity, which is averaged in time and in the azimuthal direction is displayed as a function of the radius for the different simulations at $z = 0.50$. The figure shows that close to the sidewall the azimuthal velocity is positive on average. Moving radially inwards, sections with negative and positive azimuthal velocity are observed for $Ra \leq 3.2 \times 10^{11}$, whereas for larger Rayleigh numbers the velocity of the bulk remains negative. Zooming in on the average velocity of the bulk (approx. $r < 0.08$) an overall prograde circulation is observed for $Ra \leq 7.0 \times 10^{10}$, a net circulation of (plus-minus) zero is observed for $Ra = 9.9 \times 10^{11}$ and $Ra = 1.4 \times 10^{11}$ and a retrograde circulation for $Ra \geq 2.1 \times 10^{11}$. The change of sign in averaged azimuthal velocity coincides with the change in sign of the averaged radial velocity in the top and bottom Ekman boundary layer (fig. 4.8). This is in line with the theory, where Ekman pumping is related to negative vorticity, i.e. negative azimuthal velocity, and Ekman suction to positive vorticity, i.e. positive azimuthal velocity.

The radial velocity profile is symmetric in $z = 0.50$ too. The root mean square of the radial velocity at 0.50 and 0.75 is displayed in fig. 5.4 ($z = 0.25$ in appendix B). The figures logically show low RMS values close to the sidewall boundary and in the core, i.e. low radial velocities are measured close to the sidewall boundary and in the core. Further, the increasing RMS

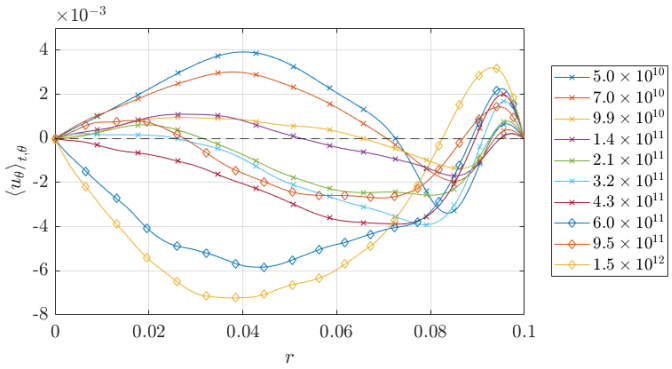

Figure 5.3: Mean azimuthal velocity (averaged in azimuthal direction and time) at $z = 0.50$ as a function of the radius for $Ra = 5.0 \times 10^{10} - 1.5 \times 10^{12}$.

as a function of Rayleigh is clearly observed.

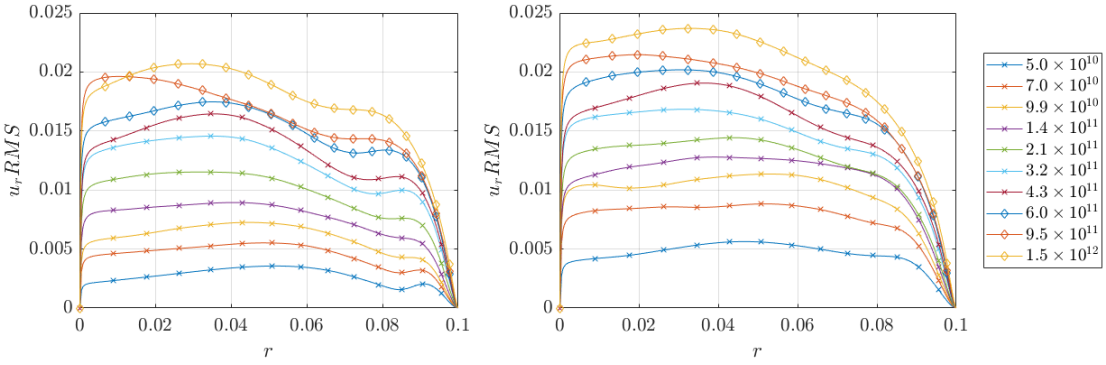

(a) $z = 0.50$ **(b)** $z = 0.75$

Figure 5.4: RMS of the radial velocity for different Rayleigh numbers at $z = 0.50$ and 0.75.

5.1 Low Rayleigh

In fig. 5.5 the radial and azimuthal velocity profiles for $Ra = 5.0 \times 10^{10}$ are displayed for $z = 0.25$, 0.50 and 0.75 as an example of a 'Low Rayleigh' flow profile. The other profiles ($Ra = 7.0 \times 10^{10} - 2.1 \times 10^{11}$) are displayed in appendix D.1. The 'Low Rayleigh' simulations are characterized by the well-pronounced radial inward jets, which are present over the whole height. The azimuthal profile is a combination of a constant bulk structure combined with a strong wall structure that changes sign at mid-height, through which the wall mode is (theoretically) not visible at $z = 0.50$. The radially inward-going jets coincide with locations with strong positive azimuthal velocities. This can be explained by the conservation of angular momentum, where radially inward moving matter gains a positive azimuthal velocity.

As mentioned before, the azimuthal profile is a superposition of a constant rotation-symmetric bulk structure and a strong non-rotation-symmetric wall structure. This asymmetric behavior results in an amplification of azimuthal velocities near the bottom of fig. 5.5d and near the top of fig. 5.5f, where two strong rings are visible (regions marked with blue dashed boxes). A close-up of the dashed boxes at $z = 0.25$ is displayed in fig. 5.6. In the outermost ring, the azimuthal velocities are pointing outwards, resulting in a radial suction of mass. This mass is supplied by the second outer ring, where two sections of azimuthal velocity collide with

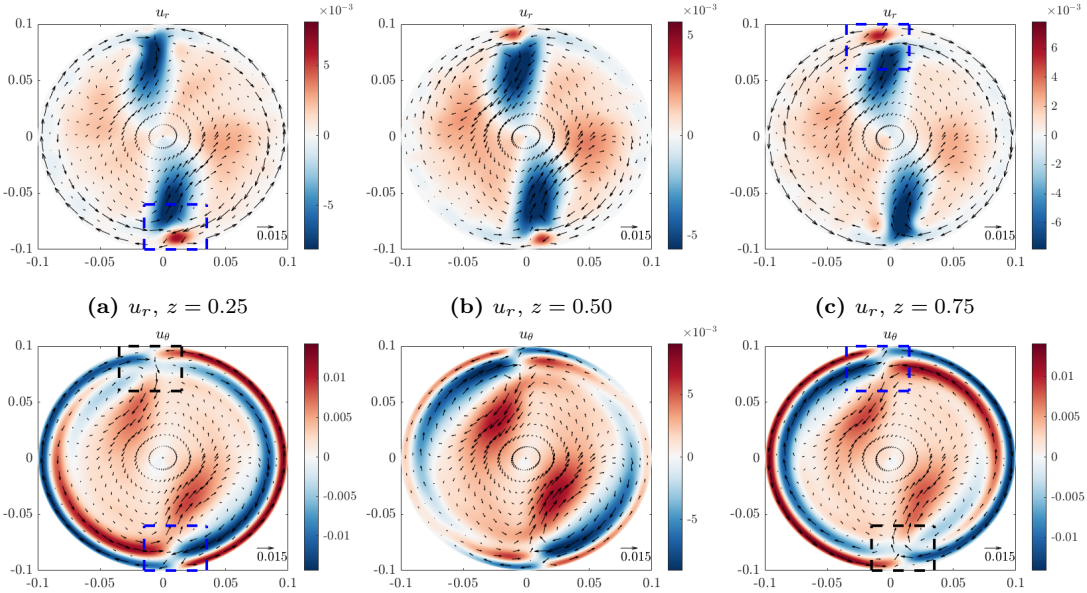

(a) u_r, $z = 0.25$ **(b)** u_r, $z = 0.50$ **(c)** u_r, $z = 0.75$

(d) u_θ, $z = 0.25$ **(e)** u_θ, $z = 0.50$ **(f)** u_θ, $z = 0.75$

Figure 5.5: Radial and azimuthal velocity profiles for $Ra = 5.0 \times 10^{10}$ at $z = 0.25$, 0.50 and 0.75.

each other, resulting in velocities in the perpendicular direction, moving radially inwards and outwards. This local flow behavior causes the remarkable 'red dots' at the end of the jets in the radial flow profiles. The prograde and retrograde rotating wall mode sections at $z = 0.25$ and 0.75 collide with each other in the regions marked with the black dashed box, resulting in a strong inward jet. Here, the (only present) outermost ring collides, so no radially outward velocity (red dot) is possible.

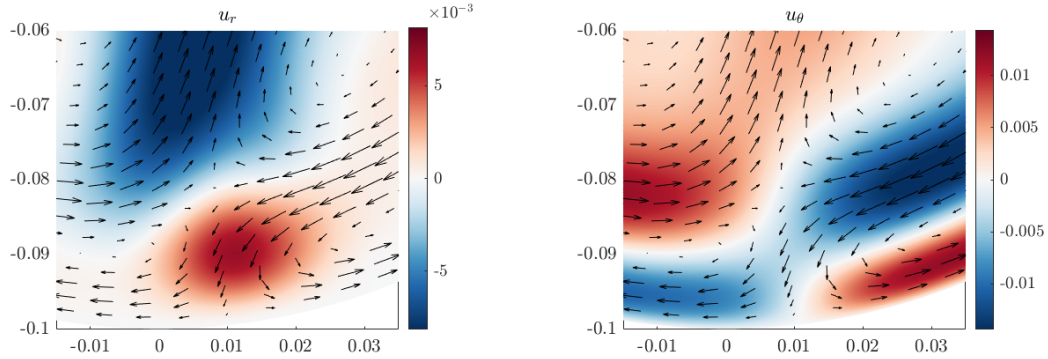

(a) Close-up of radial velocity field (blue dashed box in fig. 5.5a).

(b) Close-up of azimuthal velocity field (blue dashed box in fig. 5.5d).

Figure 5.6: Close-up of dashed boxes in fig. 5.5a and fig. 5.5d for $Ra = 5.0 \times 10^{10}$ at $z = 0.25$.

Comparing the different Rayleigh cases with each other (appendix D.1), it is visible that the radially inward jet is getting wider for increasing Ra, finally resulting in the sinusoidal profile as observed for the 'High Rayleigh' cases. For the azimuthal profile, a tendency is observed where the double-ringed wall structure combined with the bulk with two prograde orientated jets transform to a single-ringed wall structure combined with a double lobe structure in the bulk.

5.2 High Rayleigh

5.2.1 Rotation averaged profiles

In fig. 5.7 the rotation averaged azimuthal velocity fields at $z = 0.25$, 0.50 and 0.75 are displayed for $Ra = 4.3 \times 10^{11}$. At mid-height, the figure shows a well-pronounced profile with 4 lobes in the azimuthal direction ($n = 2$) and 2 or 3 lobes in the radial direction. At $z = 0.25$ and 0.75, a field with high velocities is observed with $n = 1$ in the wall region, which is the cause of the peaks in RMS-value of fig. 5.2. The dashed rings in the figures indicate the zero-crossings of the azimuthal flow profile and are the locations of the $u_\theta RMS\text{-}dip$ from fig. 5.2. Using $u_\theta RMS\text{-}dip$, the location of the zero-crossing in the radial direction can be found in the same way as using $u_z RMS\text{-}dip$ to determine the thickness of the sidewall boundaries.

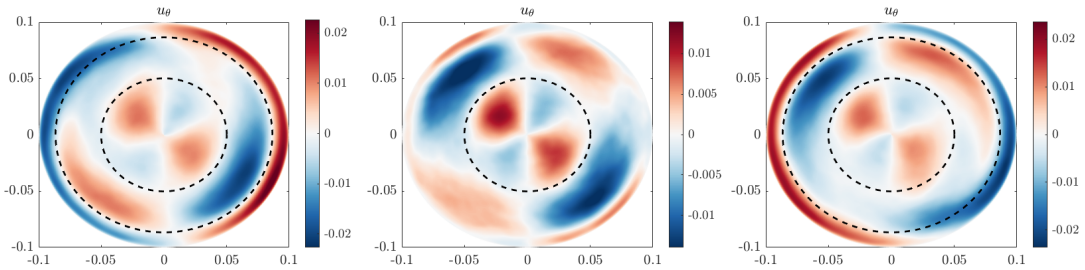

(a) $z = 0.25$ **(b)** $z = 0.50$ **(c)** $z = 0.75$

Figure 5.7: Rotation averaged azimuthal velocity profiles at $z = 0.25$, 0.50 and 0.75 for $Ra = 4.3 \times 10^{11}$. Dashed circles indicating the the zero crossings of the flow profile in radial direction, based on $u_\theta RMS\text{-}dip$.

The profile observed in fig. 5.7b looks like a profile with only a bulk mode with $n = 2$, whereas the profiles at $z = 0.25$ and 0.75 are more like a combination of a wall mode with $n = 1$ and a bulk mode with $n = 2$. The inner circle of these profiles could be described as the bulk mode ($n = 2$), whereas the outer ring ($n = 1$) is the wall mode. The ring in between is well-pronounced at one side, and badly pronounced at the opposite side. This is caused by constructive and destructive interference of the periodic behavior of the bulk and wall mode.

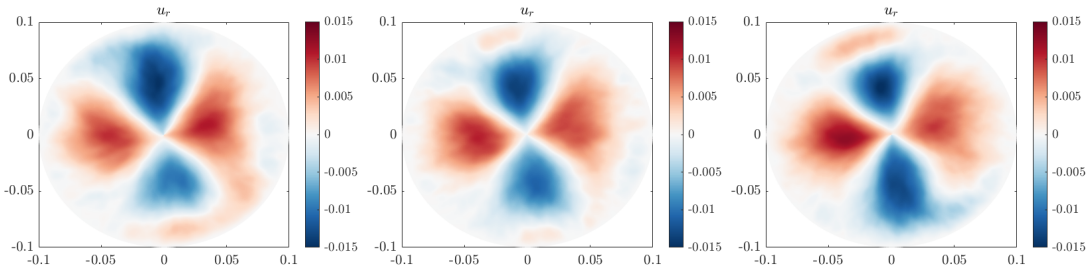

(a) $z = 0.25$ **(b)** $z = 0.50$ **(c)** $z = 0.75$

Figure 5.8: Rotation averaged radial velocity profiles at $z = 0.25$, 0.50 and 0.75 for $Ra = 4.3 \times 10^{11}$.

The orientation averaged radial velocity fields at $z = 0.25$, 0.50 and 0.75 for $Ra = 4.3 \times 10^{11}$ are displayed in fig. 5.8. The figures show a 4 lobe structure in the azimuthal direction and slightly higher velocities at $z = 0.25$ and 0.75 compared to mid-height. The lobe structure is rotated 45 degrees compared to the azimuthal flow structure (fig. 5.7b), which combined causes the 4 circulation cells displayed with the $r - \theta$ vector field in the figures. At $z = 0.25$ and 0.75, one of the radial inward jets is weaker and shorter compared to the other inward jet. This is caused by the 'red dots', as described in section 5.1. At $z = 0.50$ there is no strong

sidewall circulation in the azimuthal direction present, resulting in an (almost) symmetric velocity profile.

5.2.2 Bulk mode fitting

The azimuthal velocity profile of the bulk at mid-height is approached with the function

$$u_\theta(r,\theta) = A_{1\theta} \cdot \sin(r \cdot B_{1\theta}) \cdot \sin(2 \cdot \theta + C_{1\theta}) \tag{5.1}$$

with $A_{1\theta}$ the amplitude, $B_{1\theta}$ the radial wavenumber, and $C_{1\theta}$ the azimuthal shift. Note the factor 2 in front of θ because of the azimuthal wavenumber of 2. The radial dependence $(\sin(r \cdot B_{1\theta}))$ is chosen to force the velocity to be zero in the origin. Note that no radial decay factor is added to this fit because the RMS-values of the azimuthal velocity (fig. 5.2) as functions of the radius do not suggest such behavior. The modeled azimuthal flow profile at mid-height is displayed in fig. 5.9a, showing great degrees of coherence with fig. 5.7b.

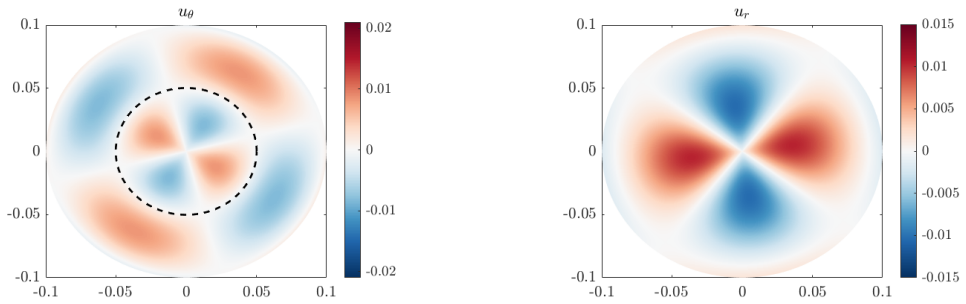

(a) u_θ **(b)** u_r

Figure 5.9: Fitted azimuthal and radial velocity profile at mid-height according to eq. (5.1) and eq. (5.2). Dashed circles indicate the zero-crossings of the profile in radial direction.

The same fitting analysis as described above is used to model the radial velocity profile at mid-height. Whereas the RMS of the azimuthal velocity profile (fig. 5.2) show a more or less constant value in the bulk (approx. $0 < r < 0.08$), the RMS of the radial velocity show a certain decrease when moving outward, which is caused by lower velocities. The radial velocity is, just as the azimuthal velocity, zero at the origin, so the same fit is used, but with an exponential decay term in the radial direction:

$$u_r(r,\theta) = A_r \cdot \sin(r \cdot B_r) \cdot \sin(2 \cdot \theta + C_r) \cdot \exp(-r \cdot D_r), \tag{5.2}$$

with the parameters that have the same function as described earlier and D_r the damping factor. This damping is added because the RMS values of the radial velocity (fig. 5.4) show a radial dependence.

To quantitatively compare the simulations with the different Rayleigh numbers, the radial and azimuthal data are made viscous dimensionless using eq. (2.16). The rotation averaged slabs at mid-height for the velocity in radial (fig. 5.8b) and azimuthal (fig. 5.7b) direction are fitted using eq. (5.1) and eq. (5.2). The fitting parameters of the amplitude (A), radial wavenumber (B), and damping (D) of the radial and azimuthal profile are tabulated in table 5.1. Note that although it looks like that there is a strong relationship between the radial wavenumber (B_r and $B_{1\theta}$) and the Rayleigh number, the zero-crossing of the profile moves just 0.003 units between the lowest and highest Rayleigh case, i.e. the radial wavelength is almost constant. The increase of radial wavenumber as a function of Ra means that the zero-crossings of the bulk structure move radially inward. This behavior matches with the increase of sidewall boundary layer thickness (section 4.1.2), i.e. increasing the sidewall thickness results in a smaller bulk region. This means that the pattern in the bulk is not

only dependent on the dimensions of the cylinder (Γ) but also depend on the thickness of the sidewall.

The radial velocity at mid-height (fig. 5.8b) is fitted using eq. (5.2), resulting in fig. 5.9b, which show a great degree of coherence with the simulated data (fig. 5.8).

Ra	A_r $(\times 10^3)$	B_r	D_r	$A_{1\theta}$ $(\times 10^3)$	$B_{1\theta}$
2.1×10^{11}	1.5	33.9	7.3	0.89	61.8
3.2×10^{11}	2.5	34.3	7.7	1.5	63.2
4.3×10^{11}	4.7	34.8	11.0	2.4	64.7
6.0×10^{11}	4.8	34.4	12.0	2.3	64.2
9.5×10^{11}	5.4	34.6	10.5	2.9	64.4
1.5×10^{12}	8.5	35.1	12.8	4.2	66.4

Table 5.1: Fit parameters of the radial and azimuthal velocity fields in viscous units at mid-height.

In fig. 5.10 the amplitude and radial wavenumbers of the radial and azimuthal velocity profiles of the simulations with different Rayleigh numbers are displayed as functions of each other. The data is fitted in both cases with a linear fit: $A_{1\theta} = a_A \cdot A_r$ and $B_{1\theta} = a_B \cdot B_r$ respectively. This results in the fitting parameters $a_A = 0.51$ and $a_B = 1.86$. The figures show that the amplitudes and radial wavenumbers of the radial and azimuthal velocity fields in the bulk are strongly related to each other.

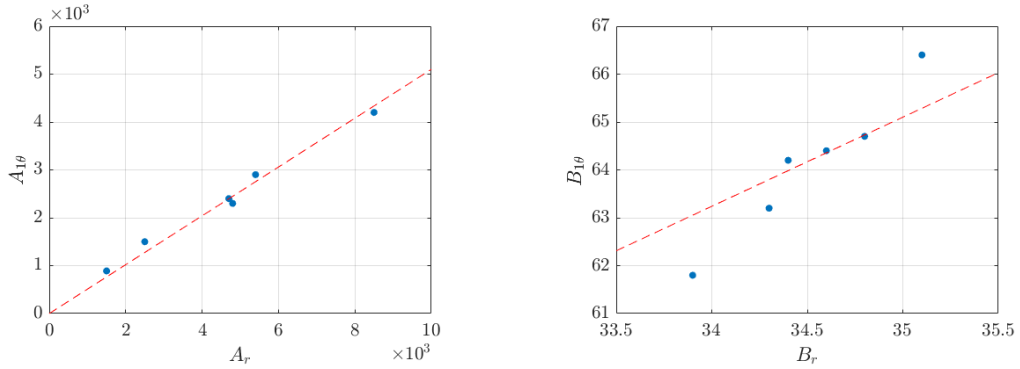

(a) Amplitude relation

(b) Radial wavenumber relation

Figure 5.10: Dependence of amplitude and radial wavenumber of radial and azimuthal velocity fields on each other.

To get an insight on the vertical distribution of the radial velocity scales, the radial velocity profiles at $z = 0.25$ and 0.75 are fitted too using eq. (5.2). Whereas the radial velocity profile is assumed to be mirror-symmetric in the height $z = 0.50$, the average of both profiles ($z = 0.25$ and 0.75) is taken to cancel out the asymmetry which is observed in fig. 5.8a and 5.8c relative to fig. 5.8b. The fitting parameters amplitude (A_r), radial wavenumber (B_r), and damping (D_r), together with the parameters of the fit at mid-height (also tabulated in table 5.1) are tabulated in appendix A and show a constant bulk mode amplitude over the height of the cylinder. The radial wavenumber at mid-height is slightly higher compared to the average wavenumbers of $z = 0.25$ and $z = 0.75$, resulting in a more compact structure at mid-height. This agrees with the observations of the boundary layer thickness, which is slightly thicker at mid-height (fig. App. A.1), resulting in a smaller bulk.

5.3 Isolating azimuthal wall mode

As mentioned before, the azimuthal flow profile at $z = 0.25$ and 0.75 is a superposition of a bulk and wall structure. Comparing the subfigures of fig. 5.7 with each other, an almost constant bulk mode is observed. The bulk profile (fig. 5.7b) is subtracted from the profiles observed at $z = 0.25$ and 0.75, resulting in an isolated wall structure. This is displayed in fig. 5.11, where the wall structure with azimuthal wavenumber $n = 1$ is visible. The wall mode is fitted with

$$u_\theta(r,\theta) = A_{2\theta} \cdot \cos((r - 0.1) \cdot B_{2\theta}) \cdot \sin(y + C_{2\theta}) \cdot \exp(-(0.1 - r) \cdot D_{2\theta}), \tag{5.3}$$

with $A_{2\theta}$ the amplitude, $B_{2\theta}$ the radial wavenumber, $C_{2\theta}$ the azimuthal shift and $D_{2\theta}$ the radial damping factor.

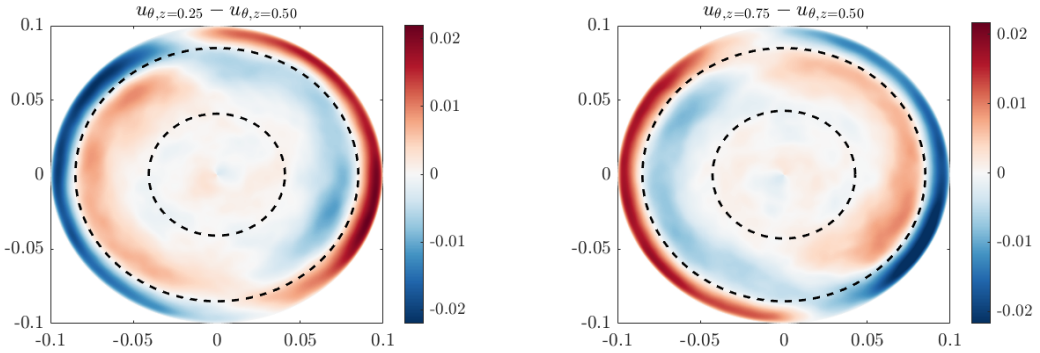

(a) Wall mode for $z = 0.25$.

(b) Wall mode for $z = 0.75$.

Figure 5.11: Isolated wall modes for $z = 0.25$ and 0.75 at $Ra = 4.3 \times 10^{11}$, which is isolated by substracting the bulk profile ($z = 0.50$) from the profiles at $z = 0.25$ and 0.75. Dashed circles indicate the zero-crossings of the profile in radial direction.

Superpositions of eq. (5.1) and eq. (5.3) are displayed for $z = 0.25$ and 0.75 in fig. 5.12a and fig. 5.12b and show large degrees of coherence with the profile as observed in fig. 5.7a and fig. 5.7c, suggesting that the observed profiles at $z = 0.25$ and 0.75 are just simple superpositions of a wall and bulk mode.

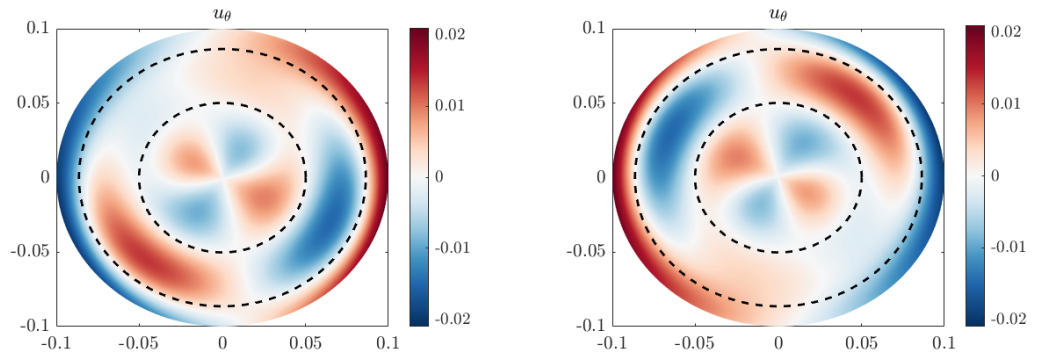

(a) $z = 0.25$

(b) $z = 0.75$

Figure 5.12: Azimuthal velocity profiles as superposition of eq. (5.1) and eq. (5.3), showing large degrees of coherence with the azimuthal flow profiles observed at $z = 0.25$ and 0.75. Dashed circles indicate the zero-crossings of the profile in radial direction.

The isolated wall structure is fitted (in viscous dimensionless units eq. (2.16)) for $Ra = 5.0 \times 10^{10} - 1.5 \times 10^{12}$ using eq. (5.3), after which the parameters $A_{2\theta}$, $B_{2\theta}$ and $D_{2\theta}$ from $z = 0.25$ and 0.75 are averaged, to get one value per parameter per Rayleigh number. These results are displayed as functions of Ra in fig. 5.13. The fits of the radial wavenumber ($B_{2\theta}$) show a constant decrease with increasing Ra, whereas the amplitude ($A_{2\theta}$) and damping ($D_{2\theta}$) show sections with Ra independent and Ra dependent behavior. This behavior is also observed for the fitting parameters of the vertical velocity field (fig. 4.14). The mathematical relation of the Rayleigh number dependence is tabulated in table 5.2. Comparing the equation of table 4.1 and 5.2, i.e. comparing the vertical and azimuthal velocity fields, one observes that the power of the amplitude parameter ($A_{2\theta}$) is almost twice as large for the vertical velocity field. The radial wavenumber ($B_{2\theta}$) scaling, i.e. a scaling for the first zero-crossing of the velocity field, of both fields is almost identical. The damping ($D_{2\theta}$) parameter power has equal size but opposite power, i.e. increasing the Rayleigh number results in faster radially decay for the vertical velocity, whereas the azimuthal velocity decays slower when moving radially inward.

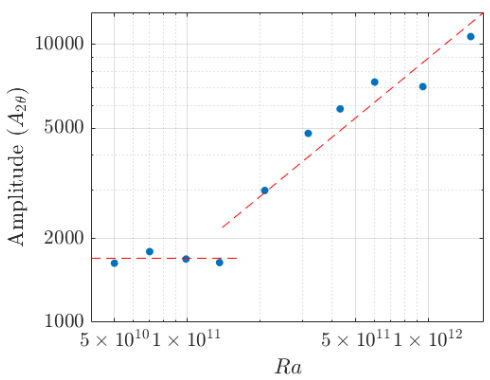

(a) Amplitude ($A_{2\theta}$) as a function of Ra.

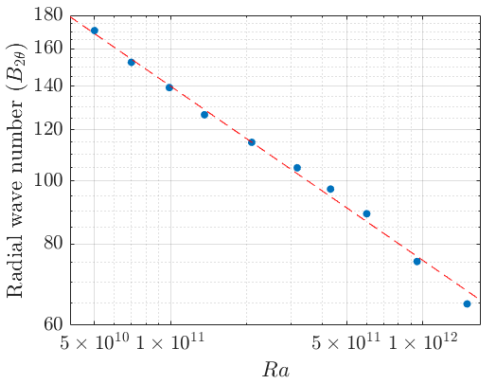

(b) Radial wave number ($B_{2\theta}$) as a function of Ra.

Figure 5.13: Fitting parameters of the azimuthal wall structure.

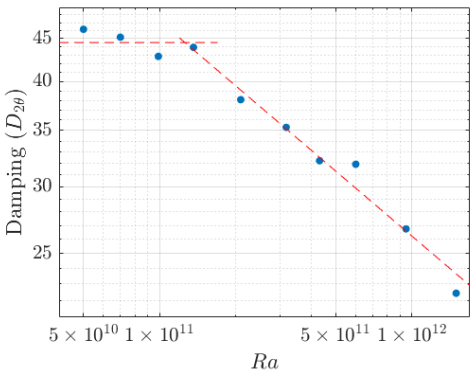

(c) Damping ($D_{2\theta}$) as a function of Ra.

Figure 5.13: Fitting parameters of the azimuthal wall structure.

	Low Ra	High Ra
Amplitude ($A_{2\theta}$)	1700	$(2.4 \times 10^{-5}) \cdot Ra^{0.71}$
Radial wavenumber ($B_{2\theta}$)	$(1.4 \times 10^{5}) \cdot Ra^{-0.27}$	$(1.4 \times 10^{5}) \cdot Ra^{-0.27}$
Damping ($D_{2\theta}$)	44.5	$(3.0 \times 10^{4}) \cdot Ra^{-0.26}$

Table 5.2: Equations belonging to the fitting parameters.

5.4 Inertial mode

The previous paragraphs concerning the bulk mode discussed the results of the simulations. In this paragraph, an attempt is made to connect the observed structures with theory.

An inertial wave mode, driven by convective instabilities, can exist in rotating Rayleigh Bénard Convection systems. The complete spectrum of inertial modes for a rotating cylinder is then determined by all axis-symmetric oscillation modes, a single geostrophic mode, and all non-axis-symmetric inertial modes (Zhang and Liao [2017]). The modes are superpositions of the Bessel function that decay radially outward. In the simulations for $Ra \geq 2.1 \times 10^{11}$ a bulk mode is observed which is z independent, with wavenumber $n = 2$ in azimuthal direction, and wavenumber $k = 1$ (u_r) or 2 (u_θ) in radial direction. The axis-symmetric oscillation modes and non-axis-symmetric inertial modes both show a sinusoidal behavior with zero velocity at mid-height, whereas the simulation results show a mode with almost constant amplitude between $z = 0.25 - 0.75$. However, the velocity components of the non-axis-symmetric geostrophic mode show no z-dependence and are given by (Zhang and Liao [2017])

$$\begin{aligned}
\vec{e}_r \cdot \mathbf{u}_{n,k} &= \frac{-\mathrm{i}n}{2r} J_n\left(\frac{\xi_{n,k} r}{\Gamma}\right) \mathrm{e}^{\mathrm{i}n\theta}, \\
\vec{e}_\theta \cdot \mathbf{u}_{n,k} &= \frac{1}{2}\left[\frac{\xi_{n,k}}{\Gamma} J_{n-1}\left(\frac{\xi_{n,k} r}{\Gamma}\right) - \frac{n}{r} J_n\left(\frac{\xi_{n,k} r}{\Gamma}\right)\right] \mathrm{e}^{\mathrm{i}n\theta}, \\
\vec{e}_z \cdot \mathbf{u}_{n,k} &= 0.
\end{aligned} \tag{5.4}$$

Here, $\xi_{n,k}$ is the k'th solution of the Bessel function $J_n(\xi_{n,k}) = 0$. Using these equations, the radial and azimuthal velocity profiles of the bulk can be calculated. As observed before, the bulk structure gets more compact with increasing Ra, which was explained by the fact that the sidewall thickness increasing with increasing Ra, through which the effective aspect ratio (Γ_{eff}) of the bulk decreases, where $\Gamma_{\text{eff}} = \frac{(D-2r^*)}{H}$, where r^* is the sidewall boundary layer thickness base on the position of $u_z RMS\text{-}dip$. Eq. (5.4) shows a Γ dependence, which could explain the observations.

The velocity profiles are calculated using eq. (5.4) for both Γ and Γ_{eff} and displayed in fig. 5.14. For comparison, the simulation results of $Ra = 4.3 \times 10^{11}$ at $z = 0.50$ are displayed too. In the figures, the boundary between the bulk and the wall region, based on the $u_z RMS\text{-}dip$ definition, is displayed with the black circle. The first zero-crossing of the simulation results of u_θ is displayed with the dashed circle and plotted in the other figures as reference. The flow profiles according to the equations show large degrees of similarity with the simulation results. The flow structure using the Γ_{eff} aspect ratio shows the largest similarity, This suggests that the bulk mode is not based on the dimensions (Γ) of the cylinder, but on the effective bulk cross-section of the cylinder, which is the cross-section of the cylinder minus the surface of the boundary layer flow.

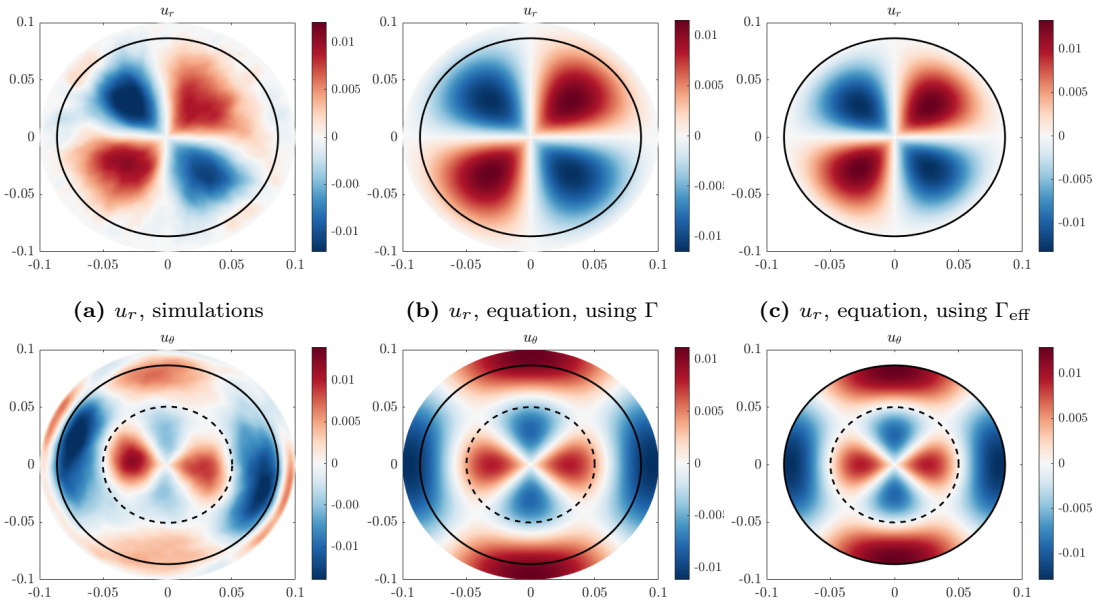

(a) u_r, simulations **(b)** u_r, equation, using Γ **(c)** u_r, equation, using Γ_{eff}

(d) u_θ, simulations. **(e)** u_θ, equation, using Γ **(f)** u_θ, equation, using Γ_{eff}

Figure 5.14: Radial and azimuthal velocity according to the simulations and geostrophic bulk mode (eq. (5.4)) for Γ and Γ_{eff}. The circle indicates the boundary between the bulk and wall region, based on $u_z RMS\text{-}dip$, the dashed circle indicates the first zero crossing of the simualtion results of u_θ and is displayed in the other figures as reference.

6 Conclusion and Outlook

6.1 Conclusion

In this work simulations are performed with $Ek = 10^{-7}$, $Pr = 5.2$ and varying Ra as an extension of the study of De Wit et al. [2020]. The newly obtained results are in line with the previous results found by De Wit et al. [2020].

The new simulations with larger Rayleigh number show the conservation of the wall mode far in the geostrophic turbulence regime. The amplitude of the wall mode is relatively large for low Ra and decreases to a constant relative amplitude for $Ra > 2.1 \times 10^{11}$. The wall mode precess in the retrograde direction, opposite to the background rotation, with a Ra dependent precession speed for $Ra \leq 6.0 \times 10^{11}$: $\omega_{\text{sc}} = (2.4 \times 10^{-9}) \cdot Ra^{0.64 \pm 0.12}$. For $Ra \geq 6.0 \times 10^{11}$ a constant precession speed is found of $\omega_{\text{sc}} = 0.079$. Note that a Ek dependence is not investigated.

The thickness of the wall mode is measured using the $u_z RMS\text{-}dip$ definition and show a wall thickness of $\delta = ((7 \pm 2) \times 10^{-5}) \cdot Ra^{0.21 \pm 0.02}$. The thicknesses based on the T_{RMS} and $\langle u_\theta \rangle = 0$ show a kink in thickness around $Ra = 1.4 \times 10^{11}$, which is a hint of a change in flow behavior around this Ra.

The coherence (R^2) of the wall mode is analyzed using a sinusoidal fit. The wall mode coherence decreases as a function of Ra for $Ra \leq 1.4 \times 10^{11}$, after which is increase to a constant value. The fluctuations in the degree of coherence of the wall mode in time are compared with the Nusselt number (heat transport) fluctuations in time in the wall mode region. These graphs show large degrees of similarity: large Nu when the wall mode is coherent and low Nu when the wall mode is not coherent. Cross-correlation calculations show that the Nu-signal has a 5 ± 3 time units delay compared to the coherence (R^2) signal, saying that a coherent wall mode is necessary to facilitate large heat transport.

The overall Nusselt number is calculated and is in line with the simulation results of De Wit et al. [2020] and the experimental results of Cheng et al. [2015]. The local Nusselt number of the wall and bulk region are calculated using the $u_z RMS\text{-}dip$ and $\langle u_\theta \rangle = 0$ definitions as boundaries between both regions. For $Ra \geq 1.4 \times 10^{11}$, the local Nu of the bulk coincides with the Nu of periodic simulations. The $\langle u_\theta \rangle = 0$ definition results in local Nu which are larger for both the bulk and wall region, indicating that this definition underestimates the thickness of the wall region. Underestimation of the sidewall boundary layer thickness results in the separation between bulk and wall inside the wall mode, resulting in an, on average, larger Nu for both the bulk and the wall region. The power-law fitting of the Nusselt number shows a Rayleigh number dependence that agrees with previous studies.

For low Ra, a constant Nu value is observed in the wall region, whereas a strong increase of heat transport in the bulk is observed. For $Ra \geq 1.4 \times 10^{11}$, both the Nu of the wall and the bulk increase. This change of behavior is related to the radial transport in the top and bottom Ekman boundary layer. For $Ra \leq 1.4 \times 10^{11}$ a negative radial velocity is observed, i.e. fluid is subtracted from the wall regions and through the top and bottom Ekman layer pumped into the bulk, resulting in the strong increase of Nu_{bulk}.

The velocity structures close to the sidewall boundary are fitted using a sinusoidal function, damped radially inward. The fitting parameters show a constant wall mode amplitude and damping factor for $Ra \leq 1.4 \times 10^{11}$. The amplitude and damping both increase for $Ra \geq 1.4 \times 10^{11}$. The same fitting is applied for the isolated wall mode in the azimuthal direction, showing the same behavior, with a change in parameter relation around $Ra = 1.4 \times 10^{11}$.

In this study also results of simulations with stress-free sidewall boundaries are discussed. For low Ra, the results show the same behavior, except for the narrower sidewall boundary layer, due to the stress-free sidewall condition. For large Ra the wall mode precesses in the opposite direction, with a double ringlike flow structure in azimuthal direction. Because just two simulations with stress-free sidewall conditions are performed, these results are only evaluated qualitatively.

The radial and azimuthal velocity fields in the bulk also show a change in flow behavior, around $Ra = 2.1 \times 10^{11}$. Below this Ra, the radial velocity field consists out of two local inward jets which are affected by rotation. For larger Ra, both the azimuthal and radial flow structures have a sinusoidal character. The flow profiles of the bulk are compared with theoretical geostrophic bulk modes and show the largest degree of similarity when the effective aspect ratio of the bulk is used. The fitting of the bulk mode using sinusoidal functions showed, except the amplitude, no large Ra dependence on the parameters, indicating that the bulk mode structure is Ra independent.

In this study several changes in the flow dynamics are observed around $Ra = 1.4 \times 10^{11}$: the radial velocity in the Ekman boundary layer changes sign (fig. 4.9), the power-law of the inner Nu dependence on Ra changes (fig. 4.11), the wall mode amplitude starts increasing (fig. 4.14a) and the bulk mode has a periodic character for $Ra > 1.4 \times 10^{11}$ (fig. 5.1). Besides that, the simulations with stress-free sidewall boundaries show different character for Ra being larger or smaller than $Ra = 1.4 \times 10^{11}$ (section 4.2). These transitions of behavior coincide with the change from columnar flow structures to plumes, which takes, in our parameter space, place around $Ra_{CP} \approx 1.1 \times 10^{11}$ (eq. (2.26)), suggesting the changes mark the changes from the columnar regime to plumes.

6.2 Outlook

Although giving a better insight into the process of Rotating Rayleigh-Bénard Convection in a slender cylinder, this research leaves issues unanswered and raises even more questions.

The research on the precession speed shows a precession frequency which is dependent on the Ra until a maximum velocity is reached (fig. 4.3), which can be explained by making use of a force balance, suggesting a dependence of the maximum velocity on the aspect ratio Γ. This dependence should further be researched. What should be taken into account is the fact that by increasing Ra the thermal forcing becomes more and more dominant over the rotation forces (Ek), ending finally in the regime of non-rotating convection (section 2.5). Further, there is the interplay of the wall with the bulk, which could influence the maximum precession velocity.

In this research two simulations with stress-free sidewall conditions are performed, which show different flow structures: different u_θ profile and wall modes precessing in the opposite direction (section 4.2). Further research could be focused on this change in u_θ and locate the Rayleigh number at which the transition from flow structure takes place, which could be the same Ra at which the transition in flow behavior takes place for no-slip sidewall conditions. In the continuation of the research on the effect of the wall conditions, a stress-free top and bottom boundary can be used, which probably will have a significant effect on the Ekman boundaries and so on the wall mode.

For all Ra a prominent wall mode is observed, whereas the bulk mode is only observed for large Ra. For large Ra the wall mode amplitude increases with increasing Ra. An unanswered question is if the wall mode causes the bulk mode or vice versa.

The two-lobe structure in the wall mode could be the source of the bulk mode: the locations

where the positive and negative parts of the wall come together are the locations of the radial inward velocity field, which could be a remnant of the jet, which was observed for low Ra. Another explanation for the bulk mode is that the four-lobe structure in the bulk flow is a stable quadropolar structure. To check which principle drives the bulk flow, new simulations can be performed with a larger aspect ratio Γ. This larger Γ results in a larger azimuthal wavenumber, e.g. a four-lobe structure in the wall mode. If the azimuthal wavenumber of the bulk does not increase with the azimuthal wavenumber of the bulk, the bulk mode is more likely to be a stable quadrapole instead of an effect of the wall mode. Γ could also be further increased, which should finally result in the same results as observed for periodic simulations.

References

Aguirre Guzmán, A. J. (2021). Numerical study of rapidly rotating turbulent convection. Technische Universiteit Eindhoven.

Chandrasekhar, S. (1961). *"Hydrodynamic and hydromagnetic stability"*. Oxford University Press.

Cheng, J. S., J. M. Aurnou, K. Julien, and R. P. J. Kunnen (2018). A heuristic framework for next-generation models of geostrophic convective turbulence. *Geophysical & Astrophysical Fluid Dynamics 112*, 277–300.

Cheng, J. S., M. Madonia, A. J. Aguirre Guzmán, and R. P. J. Kunnen (2020). Laboratory Exploration of Heat Transfer Regimes in Rapidly Rotating Turbulent Convection. *Physical Review Fluids 5*, 113501.

Cheng, J. S., S. Stellmach, A. Ribeiro, A. Grannan, E. M. King, and J. M. Aurnou (2015). Laboratory-numerical models of rapidly rotating convection in planetary cores. *Geophysical Journal International 201*, 1–17.

De Wit, X. M., A. J. Aguirre Guzmán, M. Madonia, J. S. Cheng, H. J. H. Clercx, and R. P. J. Kunnen (2020). Turbulent rotating convection confined in a slender cylinder: The sidewall circulation. *Physical Review Fluids 5*, 023502.

Ecke, R., F. Zhong, and E. Knobloch (1992). Hopf Bifurcation with Broken Reflection Symmetry in Rotating Rayleigh-Bénard Convection. *Europhysics Letters 19*, 177–182.

Ecke, R. E. and J. J. Niemela (2014). Heat transport in the geostrophic regime of rotating Rayleigh-Bénard convection. *Physical Review Letter 113*, 114301.

Favier, B. and E. Knobloch (2020). Robust wall modes in rapidly rotating Rayleigh-Bénard convection. *Journal of Fluid Mechnics 895*, R2245.

Gilman, P. A. (1977). Nonlinear dynamics of boussinesq convection in a deep rotating spherical shell-i. *Geophysical & Astrophysical Fluid Dynamics 8*, 93–135.

Goldstein, H., E. Knobloch, I. Mercader, and M. Net (1993). Convection in a rotating cylinder. Part 1 Linear theory for moderate Prandtl numbers. *Journal of Fluid Mechanics 248*, 583–604.

Hartmann, D. L., L. A. Moy, and Q. Fu (2001). Tropical Convection and the Energy Balance at the Top of the Atmosphere. *Journal of Climate 14*, 4495–4511.

Herrmann, J. and F. Busse (1993). Asymptotic theory of wall-attached convection in a rotating fluid layer. *Journal of Fluid Mechanics 255*, 183–194.

Horn, S. and P. J. Schmid (2017). Prograde, retrograde, and oscillatory modes in rotating Rayleigh-Bénard convection. *Journal of Fluid Mechanics 831*, 182–211.

Julien, K., A. M. Rubio, I. Grooms, and E. Knobloch (2012). Statistical and physical balances in low Rossby number Rayleigh-Bénard convection. *Geophysical & Astrophysical Fluid Dynamics 106*, 392–428.

Kunnen, R. P. J. (2021). The geostrophic regime of rapidly rotating turbulent convection. *Journal of Turbulence 22*, 232–241.

Lanczos, C. (2020). *"The Variational Principles of Mechanics"*. Dover Publications Inc.

Marshall, J. and F. Schott (1999). Open-ocean convection: Observations, theory, and models. *Reviews of Geophysics 37*, 1–64.

Monin, A. S., A. M. Yaglom, and J. L. Lumley (1975). *"Statistical Fluid Mechanics: Mechanics of Turbulence, Volume II"*. The MIT Press.

Nieuwstadt, F. T. M., J. Westerweel, and B. J. Boersma (2016). *"Turbulence: Introduction to Theory and Applications of Turbulent Flows"*. Springer.

Rajaei, H. (2017). Rotating Rayleigh-Bénard convection. Technische Universiteit Eindhoven.

Roberts, P. H. and E. M. King (2013). On the genesis of the Earth's magnetism. *Reports on Progress in Physics 76*, 096801.

Shishkina, O. and C. Wagner (2006). Analysis of thermal dissipation rates in turbulent Rayleigh-Bénard convection. *Journal of Fluid Mechanics 546*, 51–60.

Shraiman, B. I. and E. D. Siggia (1990). Heat transport in high-Rayleigh-number convection. *Physical Review A 42*, 36–40.

Stellmach, S., M. Lischper, K. Julien, G. Vasil, J. S. Cheng, A. Ribeiro, E. M. King, and J. M. Aurnou (2014). Approaching the Asymptotic Regime of Rapidly Rotating Convection: Boundary Layers versus Interior Dynamics. *Physical Review Letter 113*, 254501.

Stevens, R. J. A. M., R. Verzicco, and D. Lohse (2010). Radial boundary layer structure and Nusselt number in Rayleigh-Bénard convection. *Journal of Fluid Mechanics 643*, 495–507.

Stewartson, K. (1957). On almost rigid rotations. *Journal of Fluid Mechanics 3*, 17–26.

Taylor, J. R. (1997). *"An Introduction to Error Analysis, second edition"*. University Science Books, U.S.

Verzicco, R. and R. Camussi (2003). Numerical experiments on strongly turbulent thermal convection in a slender cylindrical cell. *Journal of Fluid Mechanics 477*, 19–49.

Verzicco, R. and P. Orlandi (1996). A Finite-Difference Scheme for Three-Dimensional Incompressible Flows in Cylindrical Coordinates. *Journal of Computational Physics 123*, 402–414.

Zhang, K. and X. Liao (2009). The onset of convection in rotating circular cylinders with experimental boundary conditions. *Journal of Fluid Mechanics 622*, 63–73.

Zhang, K. and X. Liao (2017). *"Theory and modeling of rotating fluids: convection, inertial waves and precession"*. Cambridge University Press.

Zhang, X., R. E. Ecke, and O. Shishkina (2021). Boundary zonal flows in rapidly rotating turbulent thermal convection. *Journal of Fluid Mechanics 915*, A62.

Zhang, X., D. P. M. van Gils, S. Horn, M. Wedi, L. Zwirner, G. Ahlers, R. E. Ecke, S. Weiss, E. Bodenschatz, and O. Shishkina (2020). Boundary Zonal Flow in Rotating Turbulent Rayleigh-Bénard Convection. *Physical Review Letter 124*, 084505.

Appendices

A Fitting parameters of velocity profiles

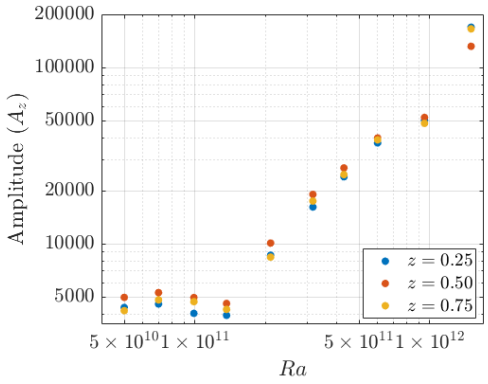

(a) Wall mode amplitude (A_z) as function of Ra.

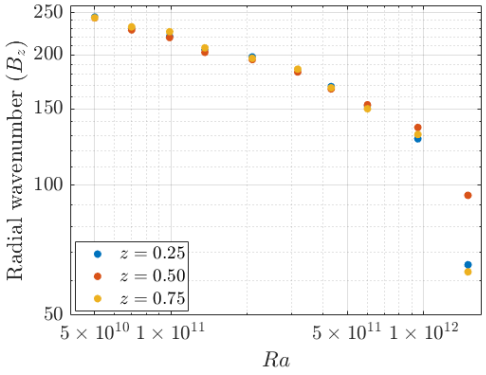

(b) Radial wavenumber (B_z) as function of Ra.

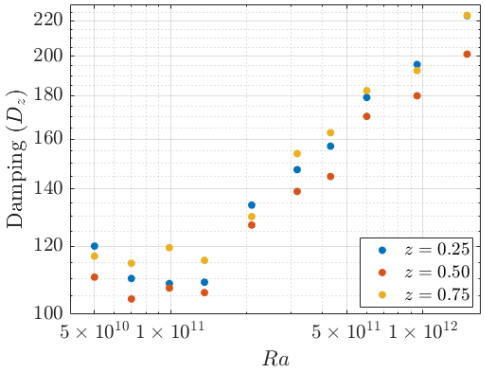

(c) Damping (D_z) as a function of Ra.

Figure A.1: Fitting parameters of the vertical velocity profile as function of Ra at $z = 0.25$, 0.50 and 0.75.

Ra	$A_{r,0.50}$ $(\times 10^3)$	$B_{r,0.50}$	$D_{r,0.50}$	$A_{r,av}$ $(\times 10^3)$	$B_{r,av}$	$D_{r,av}$
2.1×10^{11}	1.5	33.9	7.3	1.5	33.6	6.4
3.2×10^{11}	2.5	34.3	7.7	2.5	33.8	6.6
4.3×10^{11}	4.7	34.8	11.0	4.9	34.2	11.1
6.0×10^{11}	4.8	34.4	12.0	4.7	33.9	10.4
9.5×10^{11}	5.4	34.6	10.5	5.2	34.1	8.5
1.5×10^{12}	8.5	35.1	12.8	8.5	34.3	10.8

Table A.1: Amplitude (A), radial wavenumber (B) and damping (D) of the radial velocity profile at $z = 0.50$ and the average of $z = 0.25$ and $z = 0.75$ ($A_{r,av}$, $B_{r,av}$ and $D_{r,av}$).

B Root mean square of velocity profiles

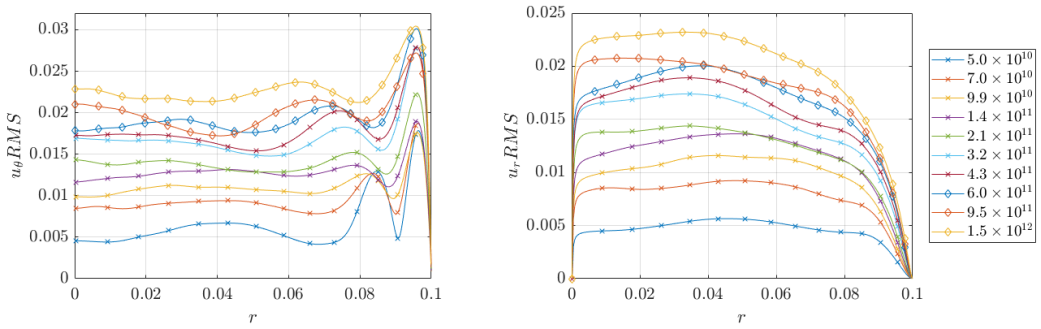

(a) $u_\theta RMS$ at $z = 0.25$ **(b)** $u_r RMS$ at $z = 0.25$

Figure B.1: Root mean squares of the azimuthal and radial velocity for different Rayleigh numbers at $z = 0.25$.

C Nusselt numbers

C.1 Nusselt number calculation

The Nusselt numbers are calculated using 5 different Nu definitions (section 2.4) and averaged. This is done by calculation the standard deviation σ_{Nu} of each Nu definition. The auto-correlation is calculated, to find the decorrelation time and the number of decorrelation times (N_{decor}). The number of decorrelation times is used as the amount of independent measurements, from which the uncertainty of the individual Nusselt numbers can be calculated using Taylor [1997]:

$$\Delta Nu \equiv \frac{\sigma_{Nu}}{\sqrt{N_{\text{decor}}}}. \tag{C.1}$$

Using ΔNu the weighted average $\overline{Nu}$ and its uncertainty $\Delta\overline{Nu}$ are calculated using

$$\overline{Nu} \equiv \frac{\sum_i w_i Nu_i}{\sum_i w_i}, \quad \Delta\overline{Nu} \equiv \frac{1}{\sqrt{\sum_i w_i}}, \tag{C.2}$$

with $w_i \equiv \frac{1}{\Delta Nu_i^2}$ being the weight corresponding to Nusselt number Nu_i. This method is not totally correct, because the Nusselt numbers are, strictly speaking, not mutually independent. Nonetheless, this method is used, as being the best approximation for the average Nusselt number and its uncertainty. The uncertainty of the Nusselt number of the bulk is determined in the same way, where only one Nusselt number is evaluated.

C.2 Nusselt numbers: no-slip sidewall boundaries

	Ra	Nu	σ_{Nu}	N_{decor}	ΔNu	$\overline{Nu}$	$\Delta\overline{Nu}$
Volume Average		104.9	17.7	17.0	4.3		
Wall $z = 0$		106.6	8.2	18.1	1.9		
Wall $z = 1$	9.9×10^{10}	106.9	9.5	15.9	2.4	106.0	1.2
Viscous dissipation		104.2	17.2	17.0	4.2		
Thermal dissipation		105.1	10.5	17.2	2.5		
Volume Average		195.4	49.0	26.1	9.6		
Wall $z = 0$		196.5	15.8	11.4	4.7		
Wall $z = 1$	2.1×10^{11}	198.3	17.9	10.8	5.4	195.3	2.6
Viscous dissipation		193.4	46.8	25.9	9.2		
Thermal dissipation		192.2	25.3	26.7	4.9		
Volume Average		387.1	110.0	23.0	22.9		
Wall $z = 0$		377.5	16.5	15.9	4.1		
Wall $z = 1$	6.0×10^{11}	379.1	18.3	7.9	6.5	377.4	3.2
Viscous dissipation		384.1	98.8	21.8	21.1		
Thermal dissipation		371.6	39.2	22.2	8.3		
Volume Average		426.3	113.9	11.8	33.2		
Wall $z = 0$		434.4	19.8	7.3	7.3		
Wall $z = 1$	9.5×10^{11}	434.8	15.5	4.6	7.2	431.0	4.5
Viscous dissipation		419.8	101.4	11.9	29.4		
Thermal dissipation		416.8	38.2	12.0	11.0		
Volume Average		559.0	133.8	11.3	39.8		
Wall $z = 0$		553.9	17.6	11.6	5.2		
Wall $z = 1$	1.5×10^{12}	555.8	18.0	7.3	6.6	552.3	3.8
Viscous dissipation		551.6	111.1	11.0	33.5		
Thermal dissipation		533.3	39.1	11.0	11.8		

Table C.1: Nusselt numbers and uncertainties of the different simulations with no-slip sidewall conditions.

Ra	Nu_{inner}	$\sigma_{Nu_{inner}}$	N_{decor}	ΔNu_{inner}
9.9×10^{10}	57.1	12.2	10.8	3.7
2.1×10^{11}	123.9	41.0	21.3	8.9
6.0×10^{11}	168.8	72.2	37.5	11.8
9.5×10^{11}	209.2	88.6	19.7	20.0
1.5×10^{12}	236.6	118.6	197.5	8.4

Table C.2: Inner Nusselt numbers and uncertainties for no-slip sidewall conditions.

C.3 Nusselt numbers: stress-free sidewall boundaries

	Ra	Nu	σ_{Nu}	N_{decor}	ΔNu	$\overline{Nu}$	$\Delta\overline{Nu}$
Volume Average		59.2	4.5	11.9	1.3		
Wall $z = 0$		60.1	3.0	11.2	0.9		
Wall $z = 1$	5.0×10^{10}	59.4	2.7	26.4	0.5	59.5	0.2
Viscous dissipation		59.5	4.5	11.9	1.3		
Thermal dissipation		59.0	3.4	21.1	0.7		
Volume Average		321.7	55.4	35.6	9.3		
Wall $z = 0$		315.7	13.2	8.8	4.4		
Wall $z = 1$	3.2×10^{11}	313.0	11.8	4.7	5.4	313.0	2.3
Viscous dissipation		314.7	49.3	33.3	8.5		
Thermal dissipation		307.1	17.7	24.6	3.6		

Table C.3: Nusselt numbers and uncertainties of the different simulations with stress-free sidewall conditions.

Ra	Nu_{inner}	$\sigma_{Nu_{inner}}$	N_{decor}	ΔNu_{inner}
5.0×10^{10}	15.0	2.4	7.5	0.9
3.2×10^{11}	72.3	30.3	11.4	10.1

Table C.4: Inner Nusselt numbers and uncertainties for stress-free sidewall conditions.

D Rotation averaged velocity profiles

D.1 Rotation averaged velocity profiles: no-slip

$$\mathrm{Ra}= 5.0 \times 10^{10}$$

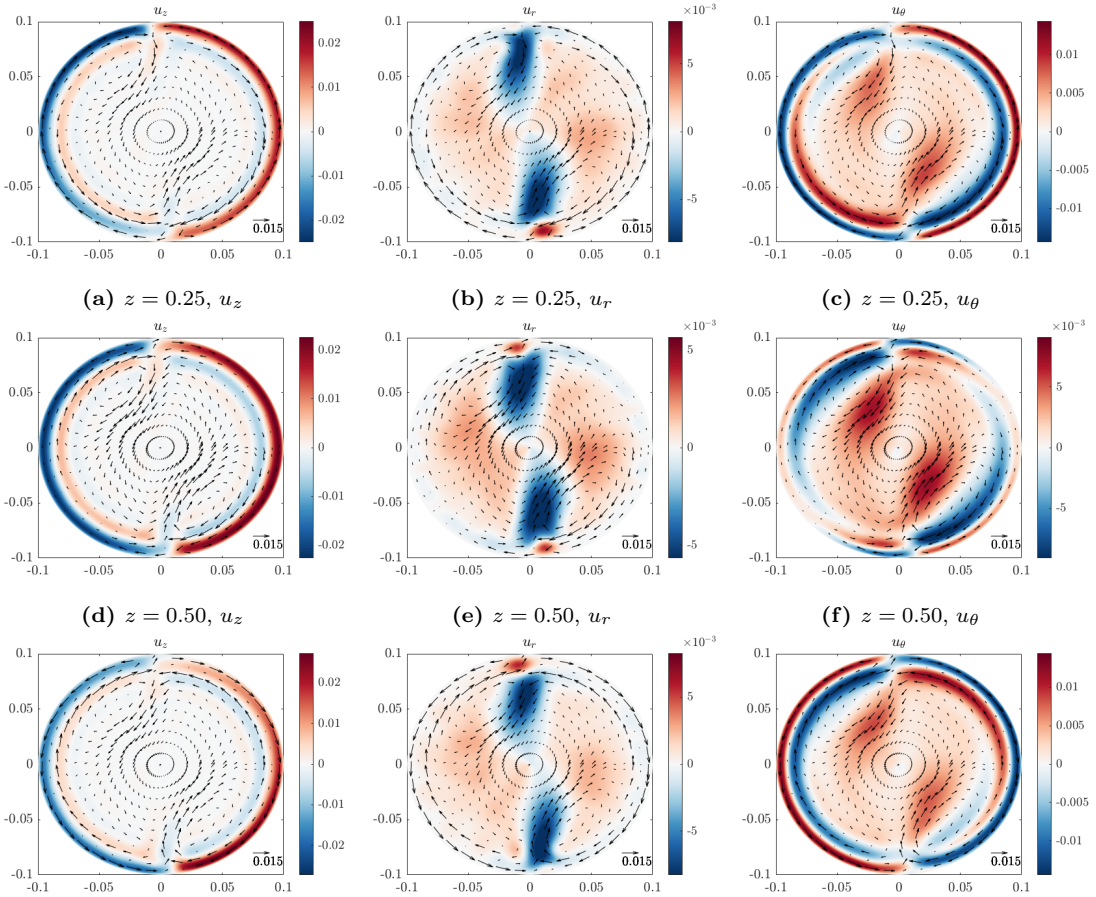

(a) $z = 0.25$, u_z **(b)** $z = 0.25$, u_r **(c)** $z = 0.25$, u_θ

(d) $z = 0.50$, u_z **(e)** $z = 0.50$, u_r **(f)** $z = 0.50$, u_θ

(g) $z = 0.75$, u_z **(h)** $z = 0.75$, u_r **(i)** $z = 0.75$, u_θ

Figure D.1: Rotation averages velocity profiles for the velocities in vertical (column 1), radial (column 2) and azimuthal (column 3) direction at $z = 0.25$ (row 1), $z = 0.50$ (row 2) and $z = 0.75$ (row 3) for $Ra = 5.0 \times 10^{10}$.

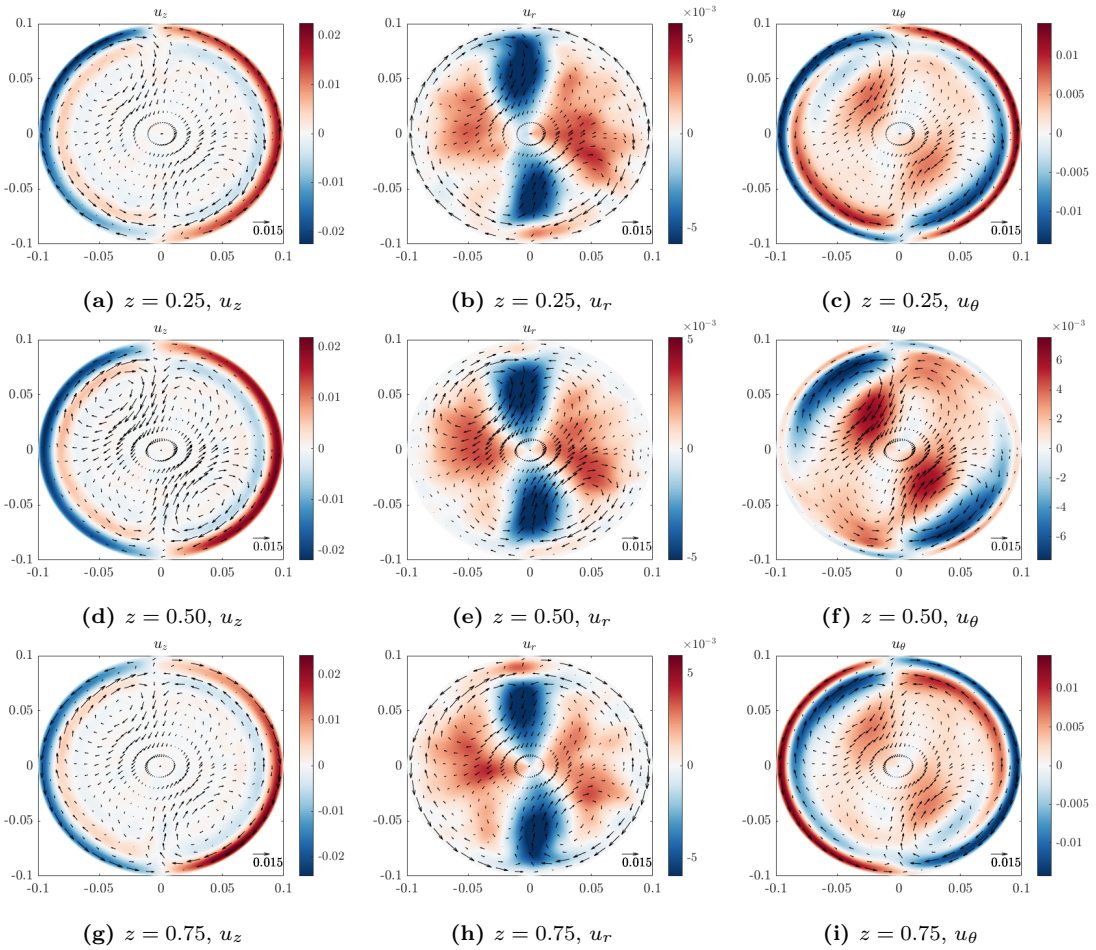

Figure D.2: Rotation averages velocity profiles for the velocities in vertical (column 1), radial (column 2) and azimuthal (column 3) direction at $z = 0.25$ (row 1), $z = 0.50$ (row 2) and $z = 0.75$ (row 3) for $Ra = 7.0 \times 10^{10}$.

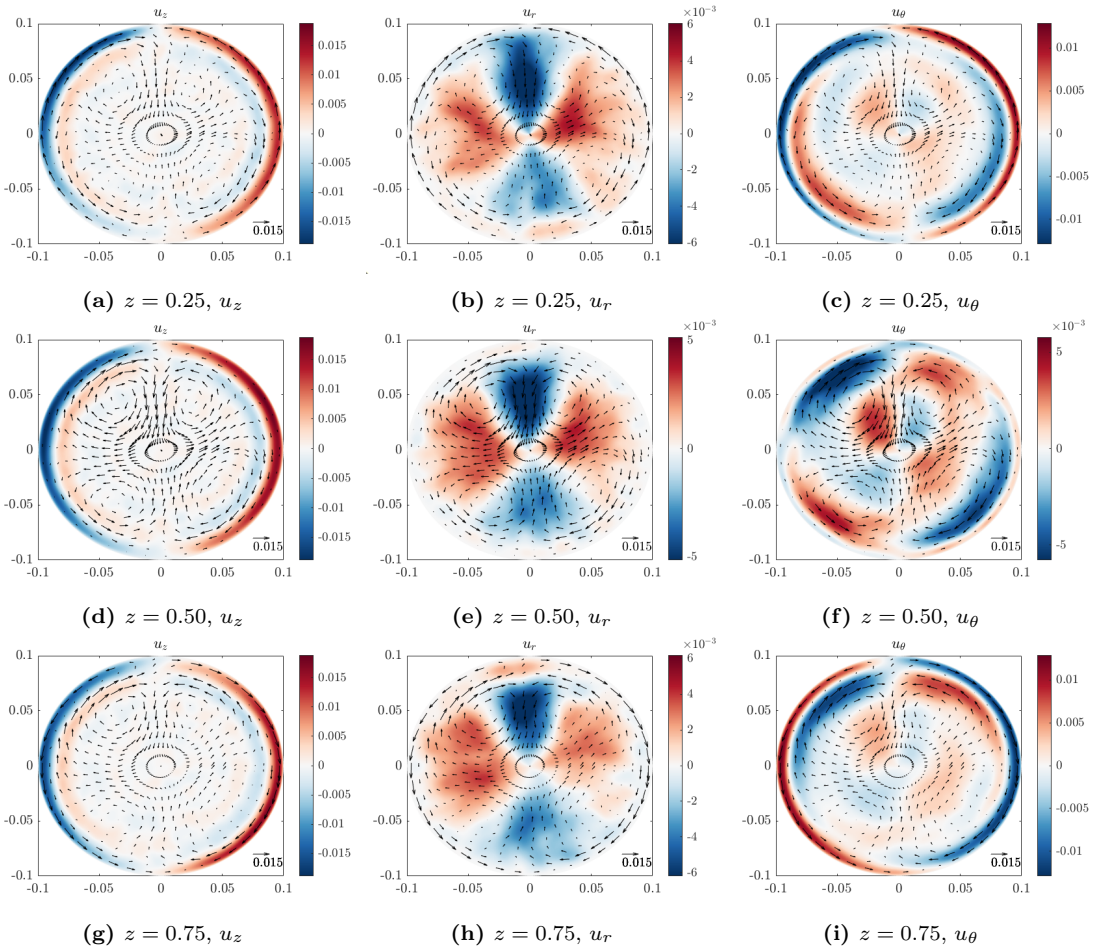

Figure D.3: Rotation averages velocity profiles for the velocities in vertical (column 1), radial (column 2) and azimuthal (column 3) direction at $z = 0.25$ (row 1), $z = 0.50$ (row 2) and $z = 0.75$ (row 3) for $Ra = 9.9 \times 10^{10}$.

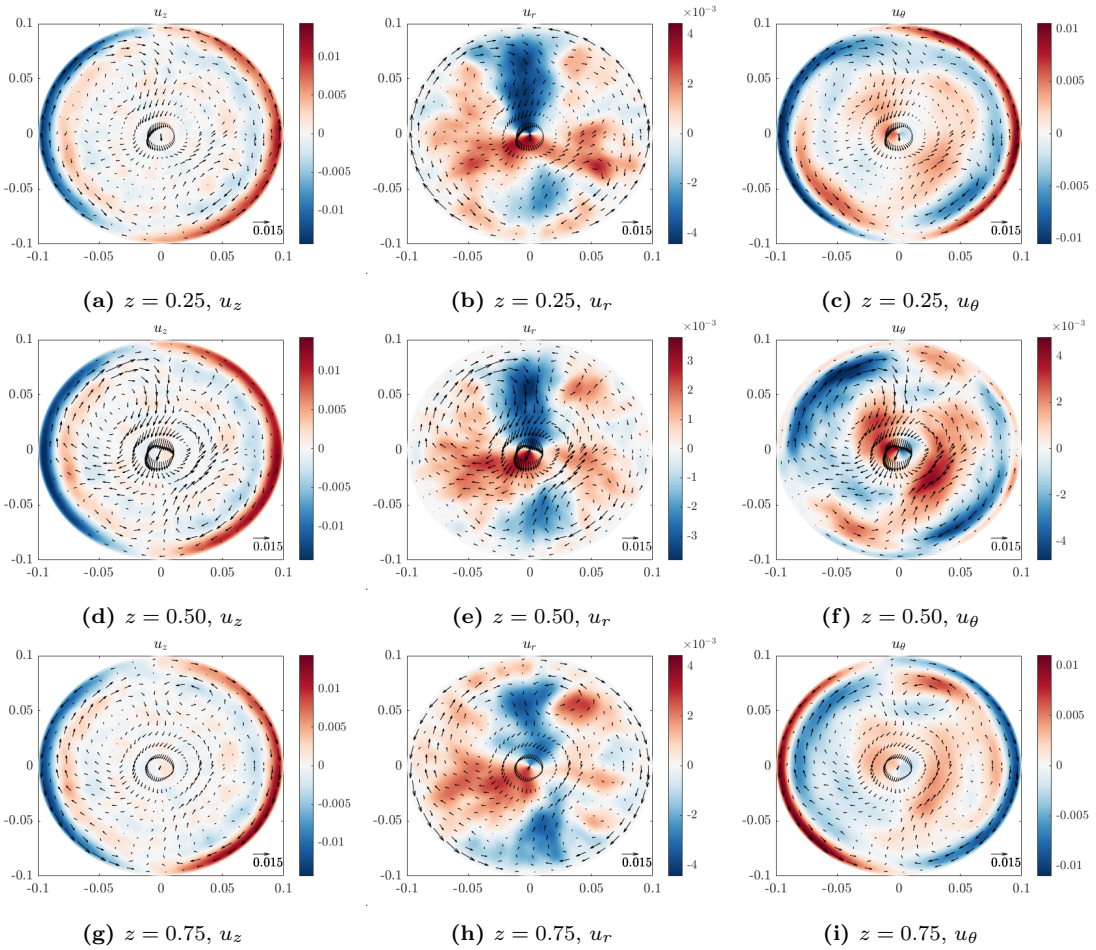

Figure D.4: Rotation averages velocity profiles for the velocities in vertical (column 1), radial (column 2) and azimuthal (column 3) direction at $z = 0.25$ (row 1), $z = 0.50$ (row 2) and $z = 0.75$ (row 3) for $Ra = 1.4 \times 10^{11}$.

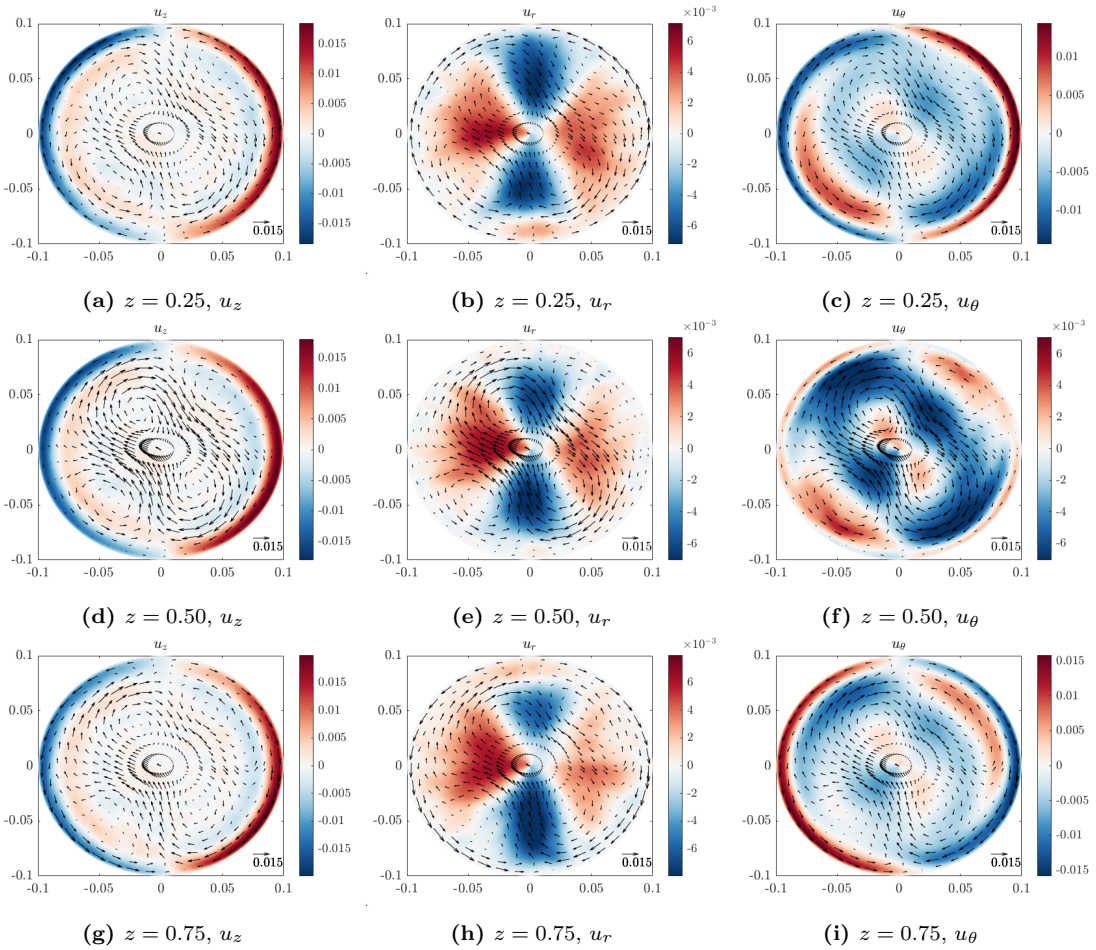

Figure D.5: Rotation averages velocity profiles for the velocities in vertical (column 1), radial (column 2) and azimuthal (column 3) direction at $z = 0.25$ (row 1), $z = 0.50$ (row 2) and $z = 0.75$ (row 3) for $Ra = 2.1 \times 10^{11}$.

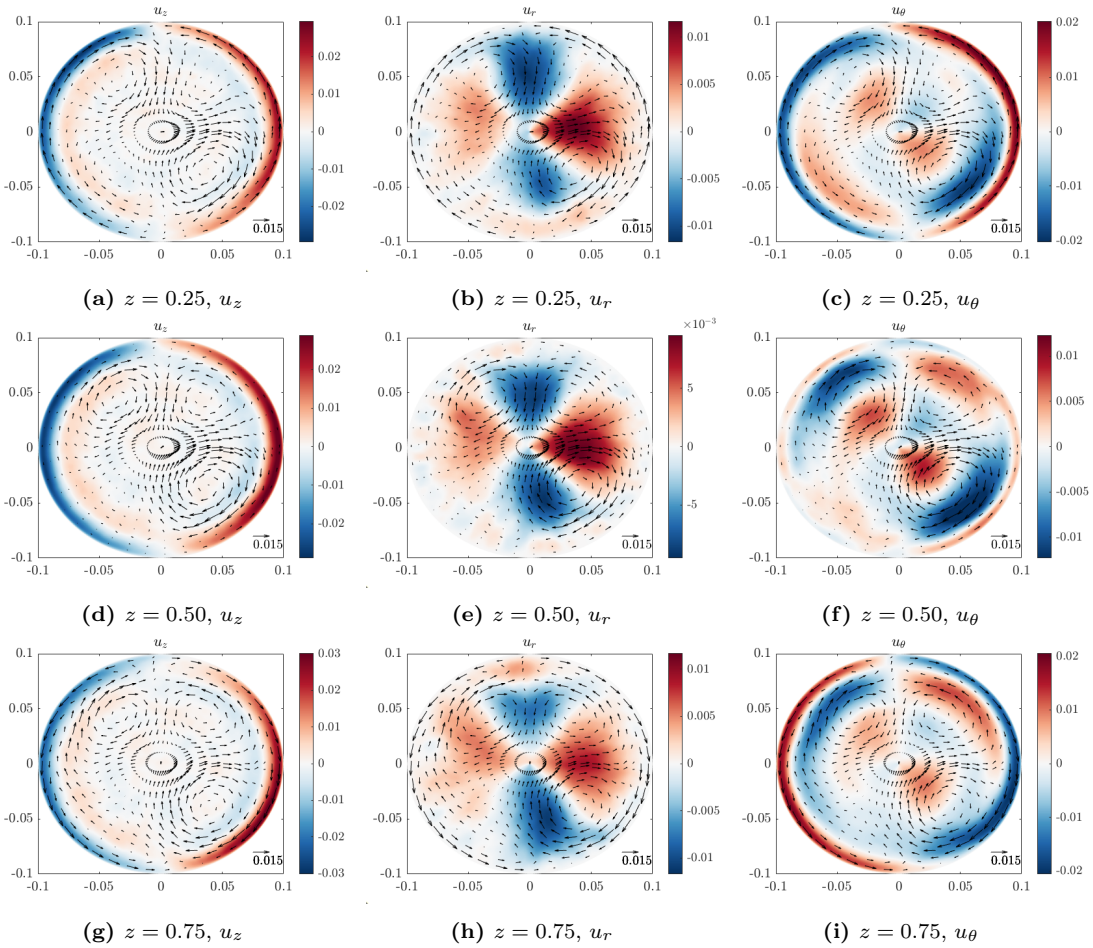

Figure D.6: Rotation averages velocity profiles for the velocities in vertical (column 1), radial (column 2) and azimuthal (column 3) direction at $z = 0.25$ (row 1), $z = 0.50$ (row 2) and $z = 0.75$ (row 3) for $Ra = 3.2 \times 10^{11}$.

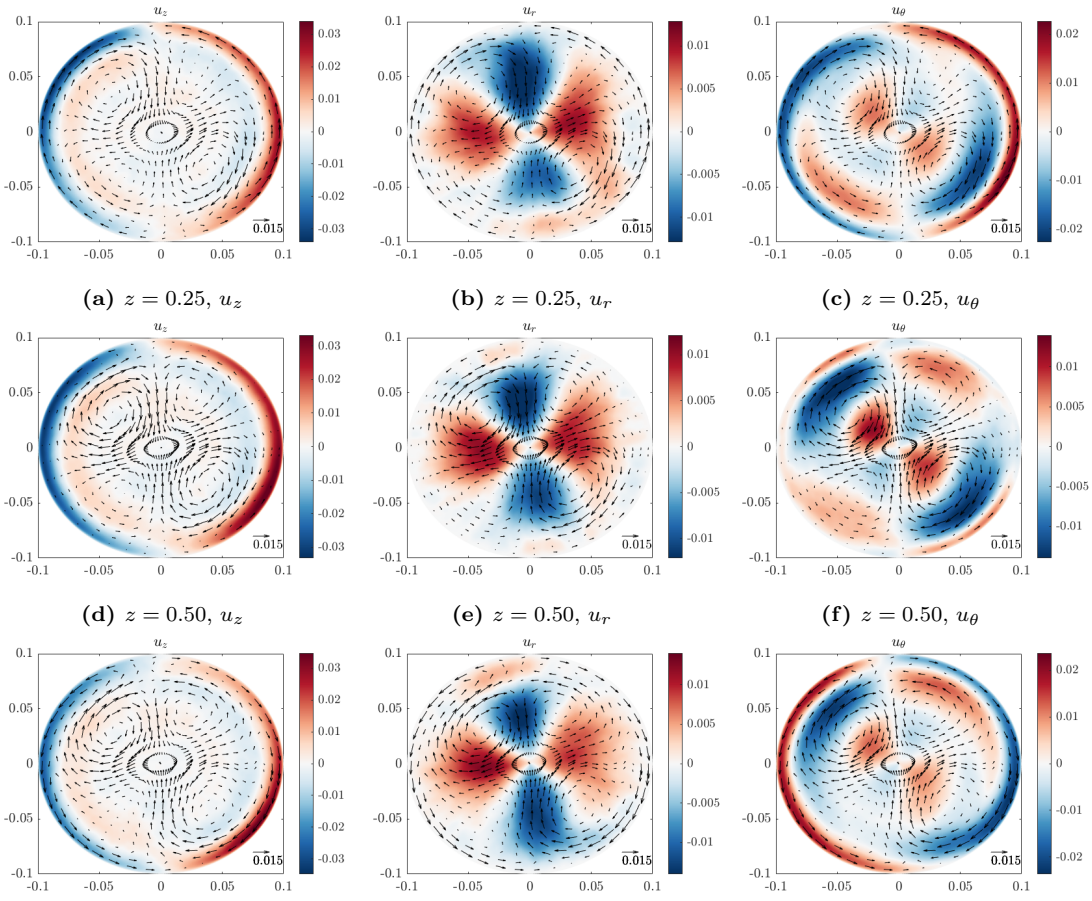

Figure D.7: Rotation averages velocity profiles for the velocities in vertical (column 1), radial (column 2) and azimuthal (column 3) direction at $z = 0.25$ (row 1), $z = 0.50$ (row 2) and $z = 0.75$ (row 3) for $Ra = 4.3 \times 10^{11}$.

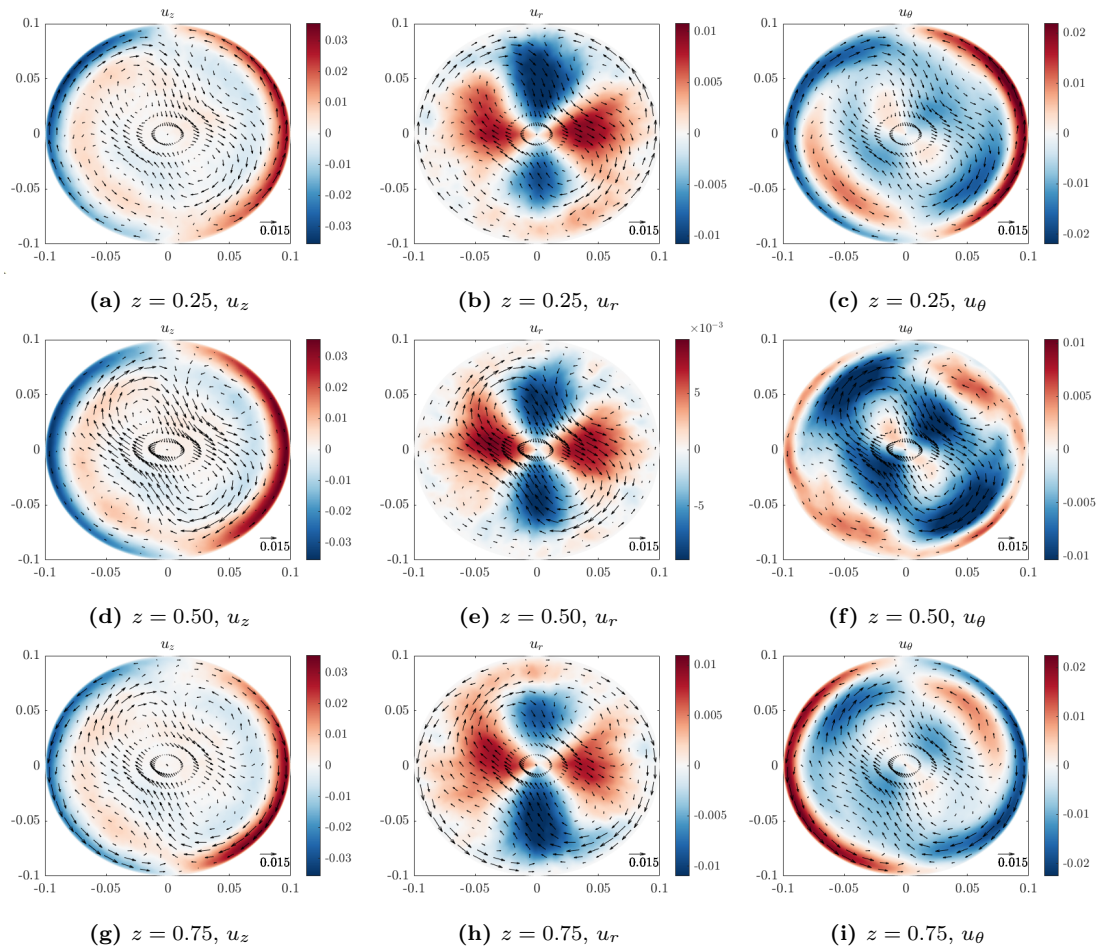

Figure D.8: Rotation averages velocity profiles for the velocities in vertical (column 1), radial (column 2) and azimuthal (column 3) direction at $z = 0.25$ (row 1), $z = 0.50$ (row 2) and $z = 0.75$ (row 3) for $Ra = 6.0 \times 10^{11}$.

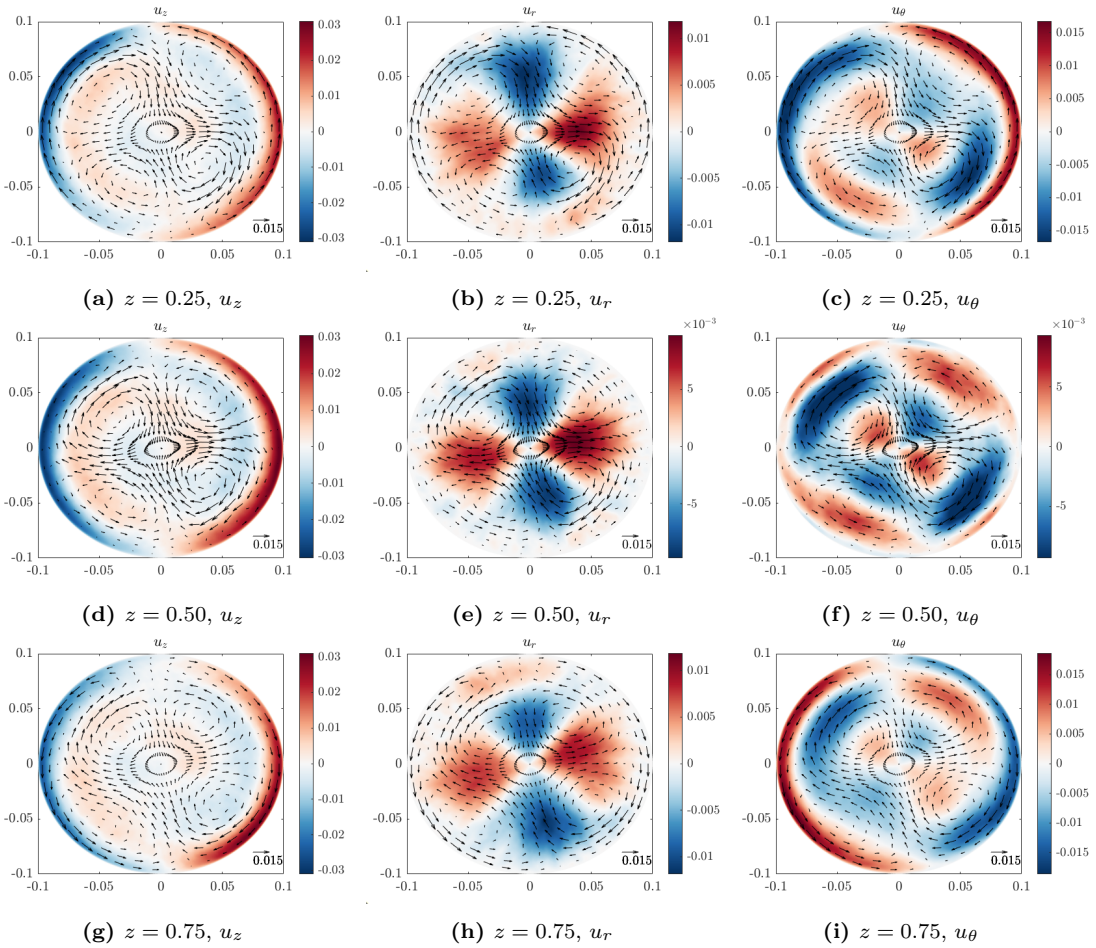

Figure D.9: Rotation averages velocity profiles for the velocities in vertical (column 1), radial (column 2) and azimuthal (column 3) direction at $z = 0.25$ (row 1), $z = 0.50$ (row 2) and $z = 0.75$ (row 3) for $Ra = 9.5 \times 10^{11}$.

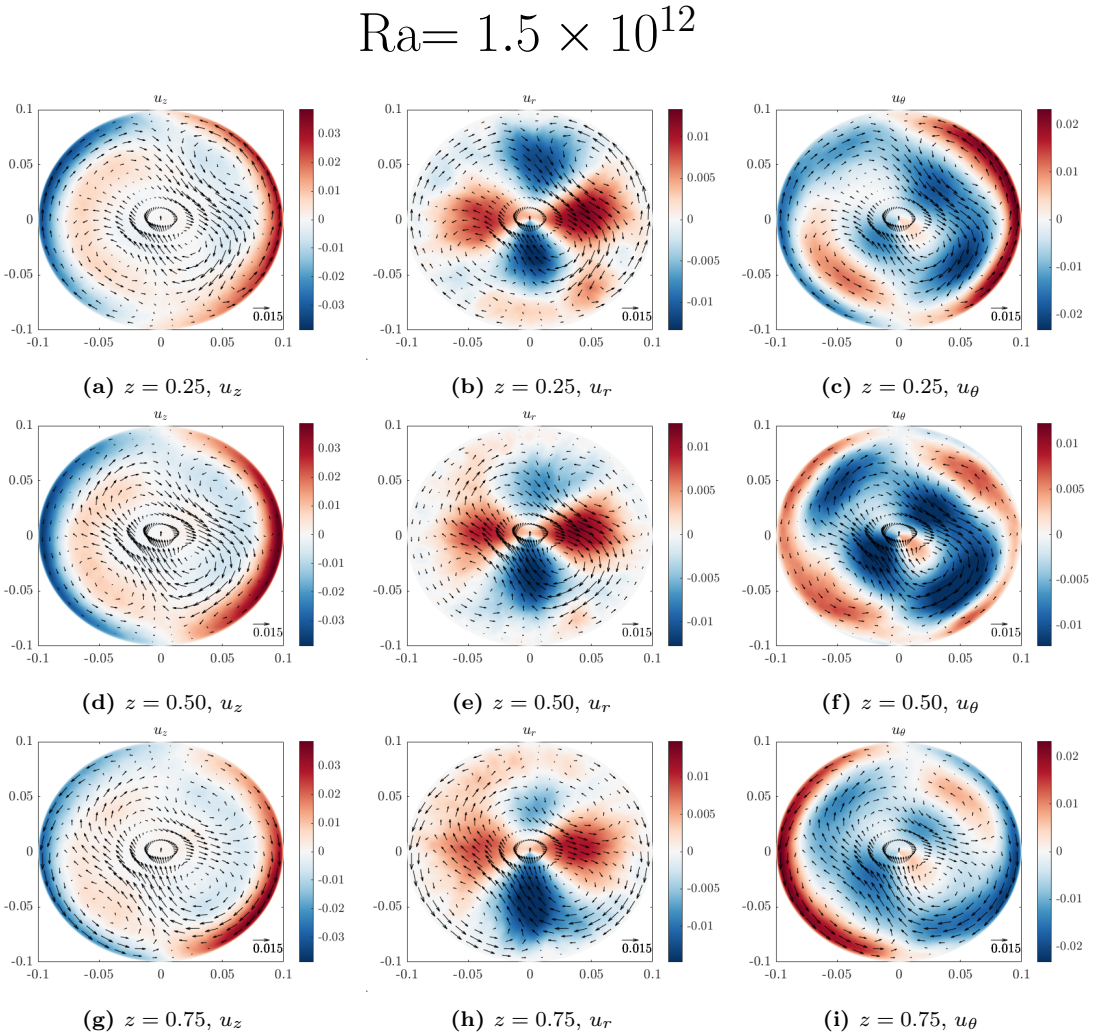

Figure D.10: Rotation averages velocity profiles for the velocities in vertical (column 1), radial (column 2) and azimuthal (column 3) direction at $z = 0.25$ (row 1), $z = 0.50$ (row 2) and $z = 0.75$ (row 3) for $Ra = 1.5 \times 10^{12}$.

D.2 Rotation averaged velocity profiles: stress-free

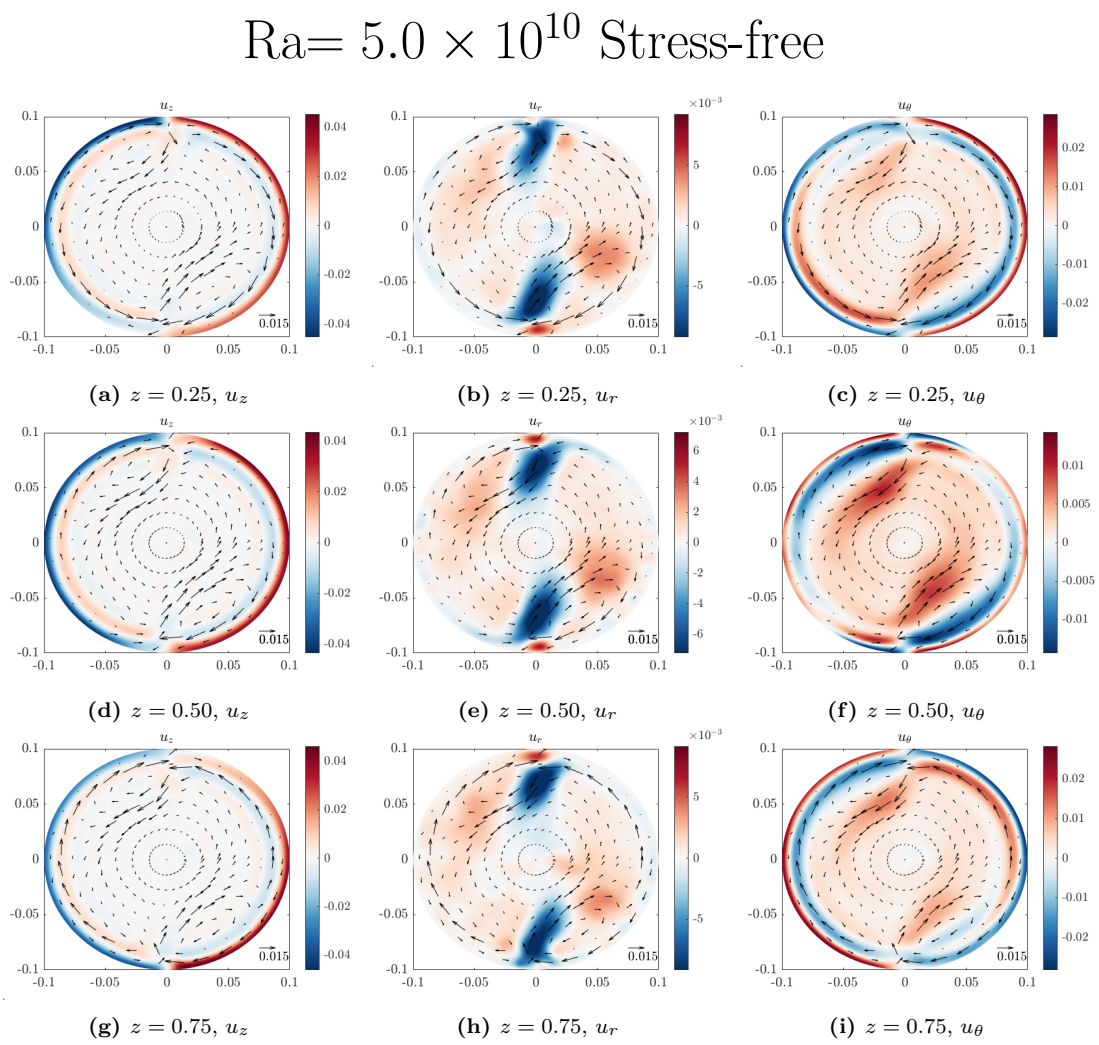

(a) $z = 0.25$, u_z **(b)** $z = 0.25$, u_r **(c)** $z = 0.25$, u_θ

(d) $z = 0.50$, u_z **(e)** $z = 0.50$, u_r **(f)** $z = 0.50$, u_θ

(g) $z = 0.75$, u_z **(h)** $z = 0.75$, u_r **(i)** $z = 0.75$, u_θ

Figure D.11: Rotation averages velocity profiles for the velocities in vertical (column 1), radial (column 2) and azimuthal (column 3) direction at $z = 0.25$ (row 1), $z = 0.50$ (row 2) and $z = 0.75$ (row 3) for $Ra = 5.0 \times 10^{10}$ with stress-free sidewall conditions.

Ra= 3.2×10^{11} Stress-free

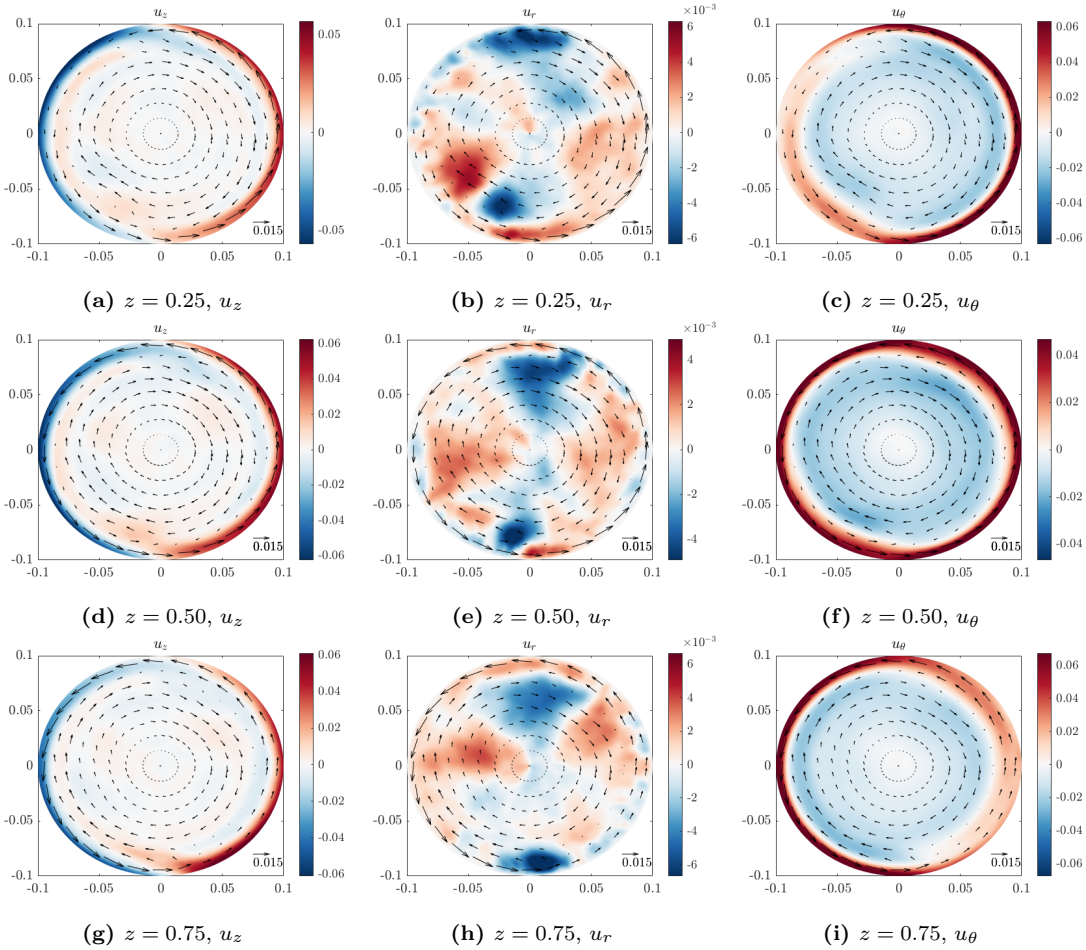

(a) $z = 0.25$, u_z **(b)** $z = 0.25$, u_r **(c)** $z = 0.25$, u_θ

(d) $z = 0.50$, u_z **(e)** $z = 0.50$, u_r **(f)** $z = 0.50$, u_θ

(g) $z = 0.75$, u_z **(h)** $z = 0.75$, u_r **(i)** $z = 0.75$, u_θ

Figure D.12: Rotation averages velocity profiles for the velocities in vertical (column 1), radial (column 2) and azimuthal (column 3) direction at $z = 0.25$ (row 1), $z = 0.50$ (row 2) and $z = 0.75$ (row 3) for $Ra = 3.2 \times 10^{10}$ with stress-free sidewall conditions.